

CREATION OF ALGORITHMS AND TOOLS FOR THE STUDY OF BRAIN  
DEVELOPMENT WITH THE IDENTIFICATION OF CONFOUNDS

AN ABSTRACT

SUBMITTED ON THE EIGHTEENTH DAY OF NOVEMBER, 2024  
TO THE DEPARTMENT OF BIOMEDICAL ENGINEERING  
OF THE SCHOOL OF SCIENCE AND ENGINEERING OF  
TULANE UNIVERSITY  
IN PARTIAL FULFILLMENT OF THE REQUIREMENTS  
FOR THE DEGREE OF  
DOCTOR OF PHILOSOPHY  
BY

*Anton Orlichenko*

---

ANTON ORLICHENKO

APPROVED:   
\_\_\_\_\_

---

YU-PING WANG  
CHAIR

*Donald P. Gaver*

---

DONALD P. GAVER



---

HONG-WEN DENG



---

ZHENGMING DING

# Abstract

This dissertation provides a description of novel algorithms and software using neuroimaging to predict subject phenotypes, with a focus on the effect of demographic confounders. Specifically, we use fMRI-derived functional connectivity (FC) to create connectomes which can then be acted upon by machine learning models to predict subject phenotypes.

We first use a large publicly available dataset, the UK Biobank (UKB), to explore natural age-related changes in the connectome in a healthy population. We find that, contrary to many existing studies, strength of connection between brain areas as measured by FC increases with increasing age. We find that the somatomotor-visual connection gives the best prediction of subject age in the longitudinal cohort of the UKB, while connectivity increases almost uniformly throughout the connectome in the cross-sectional cohort.

Next, we present a novel machine learning algorithm for the analysis of neuroimaging data when subject number is far smaller than the input features associated with each subject, as typical with neuroimaging studies. Besides using this algorithm for the prediction of phenotypes, we apply it to the integration of genomics and neuroimaging for predicting wide range achievement test (WRAT) score.

Finally, we discuss the creation of a software tool for quickly and accurately analyzing functional connectivity and genomic data and correlating these data with phenotypic variables. Using this tool, we find that the prediction of WRAT score is

heavily influenced by demographic confounds. We then describe the creation of a generative machine learning model that is able to decorrelate connectome features from demographics, finding that the majority of FC-phenotype correlations are dependent on demographic confounds.

In conclusion, this dissertation uncovers novel trends in connectome development with age, and provides new algorithms for prediction of subject phenotypes in the low-sample size, high feature dimension regime of neuroimaging studies. It also describes the under-reported effect of demographics in these studies, finding that age, sex, race, and the non-demographic of scanner task explain the vast majority of information found in both the connectome and single nucleotide polymorphism data. This lays a robust groundwork for future studies that wish to find true cognitive signal unconfounded by demographics.

**Keywords:** Functional magnetic resonance imaging, functional connectivity, multimodal neuroimaging, demographics and confounders, neuroimaging software

CREATION OF ALGORITHMS AND TOOLS FOR THE STUDY OF BRAIN  
DEVELOPMENT WITH THE IDENTIFICATION OF CONFOUNDS

A DISSERTATION  
SUBMITTED ON THE EIGHTEENTH DAY OF NOVEMBER, 2024  
TO THE DEPARTMENT OF BIOMEDICAL ENGINEERING  
OF THE SCHOOL OF SCIENCE AND ENGINEERING OF  
TULANE UNIVERSITY  
IN PARTIAL FULFILLMENT OF THE REQUIREMENTS  
FOR THE DEGREE OF  
DOCTOR OF PHILOSOPHY  
BY

*Anton Orlichenko*

---

ANTON ORLICHENKO

APPROVED: \_\_\_\_\_ 

YU-PING WANG  
CHAIR

*Donald P. Gaver*

---

DONALD P. GAVER



---

HONG-WEN DENG

*Zhengming Ding*

---

ZHENGMING DING

© Copyright Anton Orlichenko, 2024

All Rights Reserved

# Acknowledgments

I would like to give my profound appreciation to Professor Yu-Ping Wang, my mentor, for his constant support and guidance throughout my Ph.D. journey and early research career. His expertise and advice have been invaluable during every phase of my academic endeavors.

I would also like to thank Professor Donald P. Gaver, Professor Hong-Wen Deng, and Professor Zhengming Ding for serving on my dissertation committee. Their insightful comments and suggestions have significantly contributed to my dissertation's success.

My gratitude also extends to all the members of our research group. The knowledge I have gained from them over the past few years has been immense. It has been an honor and privilege to work and research alongside such a supportive and talented team.

Lastly, my heartfelt thanks go to my mother, Lidiya. Her emotional support, endless love, and encouragement have served as the bedrock of my entire graduate studies journey. Without her sacrifice and backing, reaching this remarkable milestone would never have been possible.

# Contents

<b>1</b>	<b>Introduction</b>	<b>1</b>
1.1	Introduction to Neuroimaging . . . . .	1
1.1.1	Research Domain Criteria (RDoC) . . . . .	3
1.1.2	Neuroimaging Modalities . . . . .	5
1.1.3	Integration of Multiomics and Neuroimaging . . . . .	9
1.2	The Connectome and Functional Connectivity . . . . .	11
1.3	Publicly Available Neuroimaging Datasets . . . . .	14
1.4	Challenges in Neuroimaging and Neuroscience . . . . .	19
1.5	Overview of Thesis . . . . .	21
<b>2</b>	<b>Age-Related Changes in Functional Connectivity in the UKB</b>	<b>22</b>
2.1	Introduction . . . . .	22
2.2	Methods . . . . .	24
2.2.1	UK Biobank Longitudinal Cohort . . . . .	24
2.2.2	fMRI Preprocessing . . . . .	24
2.2.3	Prediction of Scan Age and Analysis of FC . . . . .	26
2.3	Results: Somatomotor-Visual Connectivity Increases with Age . . . . .	27
2.3.1	Inter-network FC Changes . . . . .	27
2.3.2	Identification of Older Scan of Pair . . . . .	29
2.3.3	Prediction of Scan Age Using Specific Inter-network Connections	29

2.3.4	FC Changes with Age in the UKB Cross-sectional Cohort . . . . .	32
2.3.5	Comparison with Different Scanner Tasks in the PNC Dataset . . . . .	37
2.3.6	Validation on UKB Working Task . . . . .	38
2.3.7	Correlation of Longitudinal FC Changes with Health Outcomes . . . . .	38
2.4	Discussion . . . . .	41
2.5	Conclusion . . . . .	44
<b>3</b>	<b>Latent Similarity Model Identifies Important Functional Connections for Phenotype Prediction</b>	<b>46</b>
3.1	Introduction . . . . .	46
3.2	Methods . . . . .	49
3.2.1	Kernel CCA . . . . .	49
3.2.2	Latent Similarity . . . . .	51
3.2.3	Greedy Selection Algorithm and Model Interpretability . . . . .	53
3.2.4	Spurious Correlation . . . . .	56
3.3	Results . . . . .	56
3.3.1	Simulation Experiment . . . . .	57
3.3.2	Brain Development Study . . . . .	61
3.3.3	Integration of Genomics and Functional Connectivity . . . . .	73
3.4	Discussion . . . . .	78
3.4.1	Significant Functional Networks . . . . .	78
3.4.2	Significant FCs . . . . .	79
3.4.3	Robustness to Spurious Correlations . . . . .	81
3.5	Conclusion . . . . .	83
<b>4</b>	<b>Description of a Functional Connectivity Analysis Tool and Identification of Demographic Confounds</b>	<b>84</b>
4.1	Introduction to ImageNomer . . . . .	84

4.2	Methods	87
4.2.1	Architecture	87
4.2.2	Software Features	88
4.2.3	Live Web Demo, Docker Images, and Tutorial	89
4.2.4	Case Study on Ethnicity Confound in FC and Its Impact on Achievement Score Prediction	91
4.2.5	PNC Dataset	91
4.2.6	BSNIP Dataset	92
4.3	Results and Discussion	93
4.3.1	Data Exploration of Confound with ImageNomer	93
4.3.2	Validation with Regression Models	96
4.3.3	Transfer of Race Prediction Models Between PNC and BSNIP	96
4.3.4	Effect of Socioeconomic Status Explored	98
4.4	ImageNomer Conclusion	100
4.5	Demographic Variational Autoencoder for Removal of Confounds	102
4.5.1	Formulation	102
4.5.2	Validation of fMRI Samples Generated by DemoVAE	108
4.5.3	Additional Insight on Demographic Confounds in FC	114
5	Conclusion	120
5.1	Future Work	121
<b>References</b>		<b>123</b>

# Chapter 1

## Introduction

### 1.1 Introduction to Neuroimaging

Neuroscience was fundamentally changed with the development of functional magnetic resonance imaging (fMRI) technology, which allowed for unmatched querying of in vivo cognitive processes in human subjects [1]. For the first time, researchers could measure which regions in the brain were activated in response to in-scanner cognitive tasks [2]. This began with a paper by *Belliveau et al.* (1991) using a contrast agent to label blood, which would see increased flow in areas of high neural activity. At the same time, it was discovered that the blood itself could be used as a means of querying neural activity, via the blood oxygen level dependent signal, discovered by *Ogawa et al.* (1990) [3]. In subsequent years, fMRI has been used to map the brain into more than 10 functional networks [4, 5], including the default mode network (DMN), which is active in the resting state, that is, when subjects are not performing a task [6]. Other technologies, such as electroencephalography (EEG) [7], near-infrared spectroscopy (NIRS) [8], and magnetoencephalography (MEG) [9] have also been used to identify patterns of brain function in vivo.

In spite of the unmatched ability to probe brain networks in living patients, imag-

ing methods such as fMRI were limited in their ability to process data. A single fMRI scan from a patient may contain more than a million voxels (volume elements), sampled about every second, for a scan lasting tens of minutes. This curse of dimensionality makes processing imaging data challenging [10]. However, recent years have seen impressive progress in machine learning techniques, especially with regards to neuroscience [11]. New machine learning tools, such as convolutional neural networks [12], graph neural networks [13], and the transformer model [14] have changed the way one is able to work with imaging data. Specifically, they allow for integration and correlation of data at multiple scales, from imaging data at the level of the organism to genomics and multiomics data at the level of the genome or cells [15]. At the same time, large publicly-accessible datasets such as the UK Biobank (UKB) [16], Human Connectome Project (HCP) [17], Alzheimer’s Disease Neuroimaging Initiative (ADNI) [18], and Europe’s Human Brain Project (HBP) [19] are providing enough patient data for these new machine learning models to transform into robust conclusions and discoveries.

The question may be asked about the reason for studying brain networks at all. Mental health challenges are reported to cost the U.S. up to \$282 billion annually [20]. Similarly, neurological illnesses, such as Alzheimer’s disease (AD), are the second leading cause of death globally after heart disease [21]. The burden of neurological disease can be measured in disability adjusted life years (DALYs), or the loss of the equivalent of one year of full health. In this form, neurological diseases are thought to result in the loss of 276 million DALYs every year. The total cost of neurological disease in Europe is estimated to be €798 billion [22]. Interestingly, machine learning models applied to neuroimaging data have shown distinct alterations in the DMN in Alzheimer’s disease [6]. They have also proven to be able to predict conversion from healthy elderly subjects to Alzheimer’s disease patients through the identification of a brain age gap, or a difference between the chronological age of a person and that

person's "brain age" [23, 24]. In this way, it can be seen that neuroimaging combined with machine learning has the potential to reduce the burden of neurological disease on healthcare systems by identifying patients for early intervention.

### 1.1.1 Research Domain Criteria (RDoC)

In the United States, the National Institutes of Mental Health (NIMH) have seen the potential for neuroscience and machine learning to revolutionize diagnosis and treatment. In 2010 they created the Research Domain Criteria (RDoC) program as a paradigm of how research in the mental health fields should proceed. In contrast to the Diagnostic and Statistical Manual 5 (DSM-5) of the American Psychiatric Association, which bases diagnoses upon patient symptoms, the RDoC program uses a nosology based on biological factors [25]. The former director of the NIMH Thomas Insel has stated that "Unlike our definitions of ischemic heart disease, lymphoma, or AIDS, the DSM diagnoses are based on a consensus about clusters of clinical symptoms, not any objective laboratory measure." [26]

The RDoC framework is based around four key tenets:

- A diagnostic approach based on the biology as well as the symptoms must not be constrained by the current DSM categories,
- Mental disorders are biological disorders involving brain circuits that implicate specific domains of cognition, emotion, or behavior,
- Each level of analysis needs to be understood across a dimension of function,
- Mapping the cognitive, circuit, and genetic aspects of mental disorders will yield new and better targets for treatment.

Additionally, the RDoC framework consists of eight units of analysis applied to five groups of domain constructs. These units of analysis, starting from the microscopic

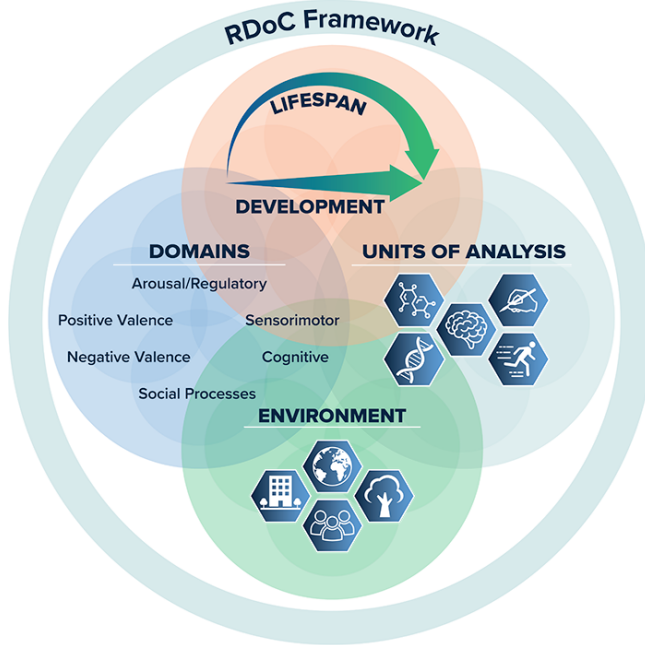


Figure 1.1: Overview of the RDoC framework, which seeks to understand mental processes throughout development and the lifespan in terms of units of analysis at various scales as well as their interaction with the environment and cognitive domains. Reproduced from <https://www.nimh.nih.gov/news/science-news/2024/revolutionizing-the-study-of-mental-disorders>.

or cell level and going to the macroscopic or organismal level are:

Genes → Molecules → Cells → Circuits → Physiology → Behavior → Self-Reports  
→ Paradigms

Current neuroscience research and machine learning frameworks work to integrate the multiple scales represented by the units of analysis [27]. Additionally, recent research treats synchrony of oscillations as the syntax by which the brain communications [28].

An overview of the RDoC framework is shown in Figure 1.1. It encompasses four distinct areas, which are lifespan/development, multiscale units of analysis, interaction with environment, and mental domains. The five groups of domain constructs are negative valence, positive valence cognitive control, social, and arousal and regulation, as seen in Figure 1.2 [29].

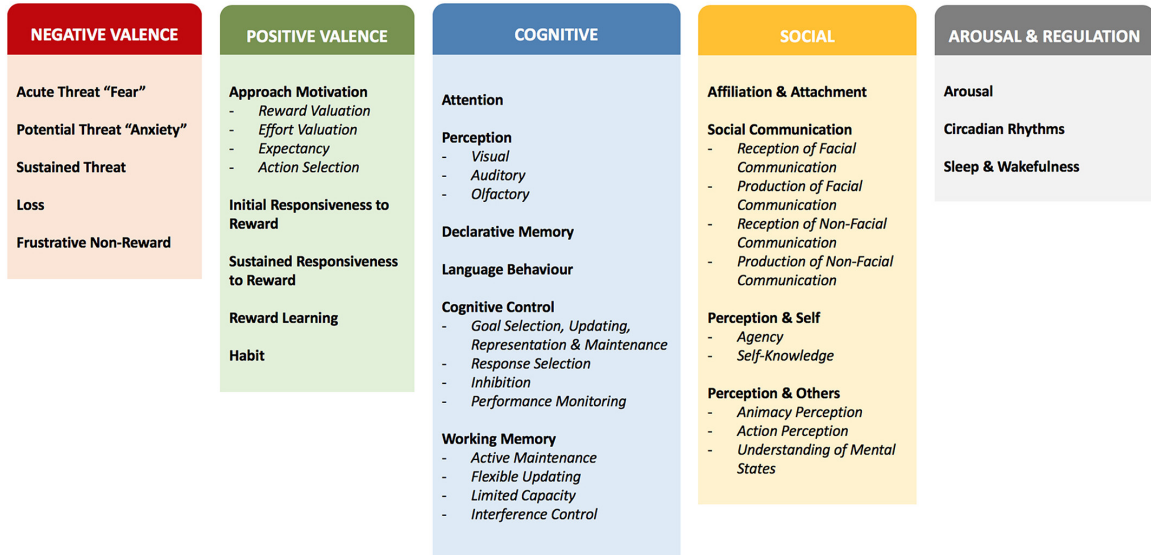


Figure 1.2: Overview of the Research Domain Criteria (RDoC) schema highlighting the five major domains, comprising 23 main constructs (bold text), wherein seven of these main constructs are further broken down into 23 subconstructs (italicized text), leading to a total of 39 primary and subconstructs. Note that in June 2018, the Positive Valence domain of the RDoC matrix underwent a reorganization. Reproduced from [29].

This dissertation will follow the RDoC framework in exploring how brain networks change throughout both early and late development. It will present novel algorithms for predicting subject level phenotypes from the information present in the genomic and circuit levels of analysis. At the same time, it will investigate what phenotypes can possibly be predicted, given the fact that confounders may be present. Finally, we will describe the creation of software tools for analysis of brain network data for detection of confounders and analysis of patient phenotypes. However, we will first present an introduction to brain imaging modalities, techniques for analysis of imaging data, and existing software tools.

### 1.1.2 Neuroimaging Modalities

Various imaging modalities are used to image both functional and structural brain data. By integrating magnetic resonance imaging (MRI), positron emission tomography (PET), computed tomography (CT), electroencephalography (EEG), magne-

toencephalography (MEG), and near infrared spectroscopy (fNIRS) in order to gain insight into normal brain processes as well as pathological disturbances.

- **MRI.** Magnetic resonance imaging (MRI) uses the resonance of hydrogen or other nuclei along with magnetic field gradients and radio waves to image those nuclei in living tissue [30]. Importantly, it does not use ionizing radiation so it is safe as long as precautions regarding heating or ferromagnetic materials in the scanner are taken [31]. Many types of MRI exist including T1-weighted, T2-weighted, proton density, diffusion weighted, contrast agent-enhanced, and others. Functional MRI (fMRI) uses oxyhemoglobin itself as a contrast agent via the blood-oxygen level dependent (BOLD) signal [3]. The premise of BOLD fMRI is that oxygenated blood flow increases in response to neural processing in activated brain regions, leading to change in signal intensity. MRI spatial resolution depends on the strength of the main B0 field in the scanner and is often 3T for human scanners and 7T or above for preclinical scanners, although higher field strength human scanners have been constructed [32]. fMRI temporal resolution is limited by the hemodynamic response function, which typically peaks after around 3 seconds [33], but high field scanners with state of the art pulse sequences have been able to take whole volume images in as little as 100ms [34]. fMRI spatial resolution is around 3-4 mm for 3T scanners but can be increased to 500 microns for 7T machines [33].
- **PET.** Positron emission tomography (PET) is another functional in vivo imaging technique that, unlike fMRI, does use ionizing radiation. Radiotracers labeled with radioactive nuclei are administered to the patient and accumulate in areas of increased metabolism, such as active tissues in the brain or in tumors [35]. Radioactive tracers commonly include molecules such as
  - Fluorodeoxyglucose ( $[^{18}\text{F}]$ FDG or FDG), commonly used to detect cancer;

- [<sup>18</sup>F]Sodium fluoride ( $\text{Na}^{18}\text{F}$ ), widely used for detecting bone formation;
- Oxygen-15 (<sup>15</sup>O), sometimes used to measure blood flow.

For example, Alzheimer’s disease typically results in decreased metabolism of both glucose and oxygen [36]. Pairs of photons emitted by the decay of radioactive tracers and annihilation of a positron are detected by scintillator crystals coupled to photomultiplier tubes or silicon avalanche photodiodes. Both the spatial and temporal resolution of PET tend to be worse than for fMRI. Current clinical scanners have temporal resolution in the range of 5-10 seconds [37] and spatial resolution of 4-5 mm [38].

- **CT.** Computed tomography (CT) uses ionizing radiation (X-rays) to image structures inside the body by taking many 2D projections and reconstructing the 3D volume from them. CT is used to visualize broken bones, identify tumors, and, with the help of a contrast agent, to visualize blood flow or perfusion [39]. The visualization of blood flow in particular may help with identification of areas affected by stroke in the brain, although CT is not typically considered a functional imaging modality. Current CT scanners have spatial resolution of 0.5mm and temporal resolution of 100ms [40]. The high spatial and temporal resolution of CT are sometimes combined with the functional imaging modality of PET to provide additional insights into cancer progression or brain function [41]. Photon-counting CT is an under-development technique to provide even better signal to noise ratio and spatial resolution to CT systems [42].
- **EEG.** Electroencephalography (EEG) is a mature technique that uses electrodes situated on the skull to record *in vivo* electrical signals resulting from brain activity. Although the first EEG was developed more than 100 years ago [43], it is still the essential clinical tool for evaluating seizure activity [44]. One downside of EEG is the poor spatial resolution: a cortical surface of  $10\text{cm}^2$

discharging synchronously is required to generate a deflection on the EEG [45]. Deeper structures in the brain also tend to result in smaller deflections on the EEG. On the other hand, the temporal resolution of EEG is extremely good, and is measured in milliseconds. EEG waveforms are categorized according to their frequency and are labeled as gamma, alpha, beta, theta, and delta [46]. It is possible to combine the high spatial resolution of fMRI and high temporal resolution of EEG in simultaneous EEG-fMRI techniques [47]. For example, fMRI may be used to create fMRI-informed EEG source reconstruction, although artifacts such as those caused by the gradient coils of the MRI scanner must be compensated for.

- **MEG.** Magnetoencephalography (MEG) uses superconducting quantum interference devices (SQUIDs) to measure tiny magnetic field variations resulting from brain activity [48]. MEG is a functional technique, and, similar to EEG, has poor spatial resolution combined with very good temporal resolution. Unlike EEG, it is not possible to combine MEG with simultaneous fMRI. MEG is used for basic research into perception and cognitive processes, localization of regions affected by pathology before surgical removal, determination of function of brain regions, and neurofeedback [49]. The SQUIDs used in MEG instruments tend to be bulky and require cooling to cryogenic temperatures to operate. Recent work on spin exchange relaxation-free (SERF) sensors have resulted in MEG equipment that is much less bulky and that can be integrated into a 3D printed helmet [50, 51].
- **NIRS.** Near infrared spectroscopy (NIRS) is a method that makes use of the near infrared (700nm to 900nm) part of the electromagnetic spectrum to image functional brain activity [52]. It does so by exploiting the different absorption spectra of oxygenated and deoxygenated hemoglobin, and can thus

be used to infer the hemodynamic response of neuronal activity. fNIRS signal is often compared to the BOLD signal measured in fMRI [53]. Typically, an NIR emitter and detector are placed ipsilaterally on the skull and the signal recorder is due to the backscatter of emitted light [54]. The benefits of fNIRS is that it is one of the least complicated and least expensive functional brain imaging techniques to set up and use while having excellent temporal resolution. The drawbacks of fNIRS are the extremely limited spatial resolution, susceptibility to noise, and lack of penetrating power into deeper regions of the brain [55].

### 1.1.3 Integration of Multiomics and Neuroimaging

A recent goal in neuroscience research, as evidenced by the multi-scale paradigms of the RDoC program, is the integration of subject and circuit-level neuroimaging information with genomics, transcriptomics, metagenomics, and others. In terms of genomic information, single nucleotide polymorphisms (SNPs) are the most common method used due to low cost and simplicity [56]. SNPs are point mutation at a particular locus, with a common and rare allele. Since they are conserved during evolution, they can be used at quantitative trait loci (QTL) to correlate to particular phenotypes [57]. The set of SNPs for a particular subject can also act as a molecular fingerprint. Rather than performing a whole genome sequencing for each subject, which can cost more than \$1,000 per genome [58] or more for cancer or rare disease sequencing, microarray based methods for SNP haplotyping have significantly reduced cost, enhancing their applicability for large public datasets. The Philadelphia Neurodevelopmental Cohort (PNC) dataset, for example, contains SNP data for more than 9,000 subjects compared to neuroimaging data for slightly more than 1,500 [59, 60].

One of the great promises of SNPs and other genotyping methods is that they can shed light on the process of disease formation. For example, it has been shown

that the a particular allele of the *APOE4* gene greatly increases the risk for developing Alzheimer's disease later in life [61]. At the same time, many psychiatric and neurodegenerative diseases, including Alzheimer's, are multifactorial and involve the interplay of many different genes and the environment [62]. Schizophrenia, for instance, is highly heritable (heritability  $\sim 0.8$ ), as shown by twin and relative studies, but much of the genetic basis remains unknown [63]. Furthermore, only about 23% of the variability associated with whether one does or does not develop schizophrenia is associated with SNPs, that is, has a genetic component not captured by other types of mutations [64].

Whereas genotype is determined at birth, phenotype and behavior describes the organism as it currently functions during the experiment, which is where neuroimaging takes place. As shown in Table 1.1, neuroimaging can often predict whether a patient has a particular psychiatric or neurodegenerative disease with good accuracy, in many cases better than the patient's genotype. Additionally, comparative neuroimaging is starting to be used as an adjunct to comparative genotyping, where genomic changes between organisms are correlated with neural structure and function [65]. Of more relevance to psychiatry, prediction of illness can be improved when combining both neuroimaging and genomic data [66]. For example, prediction of Alzheimer's disease and mild cognitive impairment was improved by about 4% when combining MRI and SNP features [67]. Alternatively, the benefit of fusing genomic and neuroimaging information may be in identifying novel biologically relevant features and pathways [68].

Fusing multiomic and neuroimaging data presents unique challenges because of the scale at which the two modalities operate. The simplest method, ensembling, using the two modalities independently to make a prediction and then combines the result [66]. A more complicated methodology uses canonical correlation analysis (CCA) to correlate multiomic and neuroimaging features prior to making a prediction

[69]. Alternatively, independent component analysis (ICA) may be used to fuse the modalities into jointly maximally independent components [70, 71]. More recently, graph neural networks have been used to model the relationship between and fuse disparate modalities in multiomics and neuroimaging [72–74].

## 1.2 The Connectome and Functional Connectivity

Research in recent years has yielded immense progress in understanding of brain function at scales ranging from genes, proteins, cells, neurons, neuronal circuits, up to including the organism and behavior [11]. Much of that knowledge has come from the relationships between different neuronal structures and how they link together. That linkage is referred to as the connectome. A connectome can be thought of as a wiring diagram that shows how different neurons or different brain regions communicate [75]. In neuroimaging studies, many types of connectomes may exist.

Diffusion tensor imaging (DTI), for instance, may yield the physical connections between different regions formed by axon tracts inferred from the anisotropy of diffusion of water. This use of diffusion information to perform tractography may be referred to as **structural connectivity** [76]. In addition to the brain, structural connectivity from tractography has been found useful in the study of tissues such as the heart or prostate [77]. The high information content of DTI voxels also make them very sensitive to pathology such as tumors. Besides its use in identifying regions of brain ischemia and oncology, physical connectivity has been used to infer regional activity in the performance of cognitive tasks, based solely on task-independent connections [78].

In contrast to structural connectivity, which measures physical connections such as axon tracts, **functional connectivity** refers to actual information flow between regions in the brain. Such information flow is often represented by the temporal

Study	Dataset	# of Subjects	Predictive Task	Accuracy
Hu et al. 2019 [81]	PNC	857	Age (child vs. young adult)	99%
Zhang et al. 2018 [82]	HCP	820	Sex	87%
Orlichenko et al. 2023 [83]	PNC, BSNIP	830	Race	85%
Du et al. 2023 [84]	COBRE + study-specific	688	Schizophrenia	73-76%
Zou et al. 2022 [85]	study-specific	80	Bipolar disorder	68-72%
Suo et al. 2020 [86]	study-specific	122	PTSD	$\rho = 0.298$
Ingahalikar et al. 2022 [87]	ABIDE	988	Autism	60-90%
Hua et al. 2023 [88]	ADNI	235	Preclinical Alzheimer's disease	75-90%
Shi et al. 2022 [89]	FCP/INDI	100	Parkinson's disease	67%
Park et al. 2020 [90]	UKB	1,497	Obesity	$\rho = (0.308, 0.556)$

Table 1.1: List of representative studies using fMRI-based functional connectivity to predict patient demographics or illness status. In some cases, a correlation-based methodology was employed instead of a training and test set.

correlation of the bandpass-filtered BOLD signal between two regions [79]. It is hoped that functional connectivity, derived from either resting state or task-based fMRI, may help with prediction and diagnosis of, e.g., bipolar disorder, PTSD, and other illnesses, as well as to help measure the effect of treatment [80]. Indeed, functional connectivity has been successfully used to predict subject age, sex, race, schizophrenia or bipolar disease status, preclinical Alzheimer's disease, and autism. A list of studies using functional connectivity as a predictive tool is given in Table 1.1. Most of the large studies in that table make use of public datasets, some of which will be described in Section 1.3.

Calculation of functional connectivity requires that the regions between which communication occurs are clearly defined. Most often, this can be done either using some form of independent component analysis (ICA) or by using a predefined Atlas.

Atlas	# of Subjects	Derivation Method	# of Regions	Modality
Power et al. 2011 [5]	446	Graph theory Pearson correlation	264	Functional
Automated Anatomical Labeling 3		Anatomical considerations	166	Anatomy
Rolls et al. 2020 [94]				
Glasser et al. 2016 [95]	210	Group average parcellation	180	Structural, functional
Shen et al. 2013 [96]	79	Graph theory	268	Functional
Brainnetome	80	DTI tractography	246	Functional
Fan et al. 2016 [97]		Optimal clustering solution		

Table 1.2: List of atlases commonly used for the calculation of functional or structural connectivity of the brain.

Both approaches have their advantages and disadvantages. For one, group ICA is a data driven approach, with divisions of the brain into regions based completely on the signals found in the group of subjects under study [70]. Therefore it is not subject to a prior bias. On the other hand, ICA regions are not reproducible from study to study and often have no fixed relationship to anatomical structures in the brain. An atlas, by contrast, gives a consensus set of regions derived from the group of subjects used to build the atlas, and is replicable across studies that use the same atlas. Table 1.2 lists some atlases commonly used in neuroimaging studies, particularly in fMRI.

It should be noted that prior to creation of these atlases, most MRI studies warp brain data to the space of the average brain of the Montreal Neurological Institute (MNI), constructed in 2001 [91], so that regions from different subjects are located in approximately the same coordinates and are transformed to be approximately the same sizes [92]. Registration is commonly performed using either the Statistical and Parametric Mapping (SPM12) Matlab-based software (<https://www.fil.ion.ucl.ac.uk/spm/software/spm12/>) or the FMRIB Software Library (FSL) freestanding software [93].

Besides connectivity, fMRI has traditionally used Z-score of changes in average

BOLD signal between task and no task to localize cognitive tasks to specific brain regions. For example, task vs rest comparison of average BOLD signal has been utilized to localize regions associated with vision [98], speech [99], emotion [100], and others. Nevertheless, derived metrics such as functional connectivity hold more promise clinically for the prediction of illness or neurodegenerative diseases. Finally, while functional connectivity measures the undirected correlation between signals in different brain regions, **effective connectivity** goes one step further and seeks to uncover the directional, causal links between brain regions [101]. This is typically done by first identifying potential undirected links between brain regions then using a causality algorithm to assign directionality, such as dynamic causal models (DCM) [102].

### 1.3 Publicly Available Neuroimaging Datasets

One of the challenges of neuroimaging, especially using fMRI, is the high cost of data acquisition, at more than \$1000 per subject. In recent years, the median cohort size for published experimental and clinical fMRI studies was 24 subjects, and fewer than 1% of datasets contained more than 100 subjects [103]. At the same time, the large amount of information contained in neuroimaging data means that models trained with small numbers of subjects often overfit the data and become unreproducible [104]. This highlights the need for pooling resources in order to create datasets having large numbers of subjects in order to robustly identify small but significant signals. Some examples of publicly available datasets are given below.

- **PNC.** The Philadelphia Neurodevelopmental Cohort (PNC) is a widely-used dataset of children and young adults with multi-task fMRI scans for 1,529 subjects [60] and genomic data for more than 9,000 subjects [59], many of whom have both modalities. In addition, the PNC includes data for 169 question-

naire, computerized battery, and in-scanner task parameter fields, not all of which are available for every subject. Scholastic achievement was measured using the Wide Range Achievement Test (WRAT) [105], with both a raw score and score with the effects of age regressed out. The dataset is intentionally enriched for subjects of European (EA) and African (AA) ancestry. This dataset has been used in many studies of normal development during adolescence and is particularly valuable because it contains both neuroimaging and genomic data.

- **HCP.** The human connectome project (HCP) is a joint project between Washington University, the University of Minnesota, Harvard, UCLA, and Oxford that aims to provide several large datasets containing neuroimaging and phenotype data (<https://www.humanconnectome.org/>) [106]. For example, the HCP Aging dataset contains 1200 normal subjects aged 36-100+ years old, while the HCP Development dataset, similar to PNC, contains neuroimaging data for 1350 subjects aged 5-21 years old. The HCP also contains a unique large dataset of baby and young children neuroimaging data, having 500 subjects aged 0-5 years old. In addition, the HCP contains data releases for specific morbidities, including the 300 subject Alzheimer's disease connectome project and the 340 subject epilepsy connectome project. Neuroimaging data includes both functional, structural, and diffusion data for all subjects. All data is de-identified and MRI data has been defaced to preclude identification through facial reconstruction [107].
- **BSNIP.** The bipolar and schizophrenia network for intermediate phenotypes (BSNIP) contains structural MRI, functional MRI, EEG, and symptom/questionnaire data for 933 probands, divided among 397 schizophrenia patients, 224 schizoaffective disorder patients, and 312 bipolar disorder patients [108]. Along with these patients, at least one relative was also recruited, resulting in a group of

1,059 relatives (41.8% parents, 39.7% siblings, 18.5% children). An additional 459 healthy controls were enrolled from the same catchment areas. Along with imaging and demographics, data was included for medication info as well as positive and negative syndrome scale (PANSS) for schizophrenia scores. Among relatives, only approximately 1/3 lacked any Axis I or Axis II psychiatric disorder or drug abuse history. As typical of overall patient statistics, BSNIP schizophrenia patients were skewed to being predominantly male (69.3% male).

- **COBRE.** The center for biomedical research excellence is contributing structural MRI and fMRI data for 100 patients with schizophrenia and 100 healthy controls ([https://fcon\\_1000.projects.nitrc.org/indi/retro/cobre.html](https://fcon_1000.projects.nitrc.org/indi/retro/cobre.html)) [109,110]. The age range for subjects is from 18 to 65 years old in each group. In addition to anatomical and functional scans, phenotype information on age, sex, handedness, and other diagnostics were included in the data release. Subjects were excluded if they had a history of substance abuse or head injury.
- **Dev-CoG/Dev-MIND.** The developmental chronnecto-genomics (Dev-CoG) study is a multimodal study of the development of the human brain in otherwise healthy children and adolescents [111]. The Dev-MIND study is a follow-up study increasing the number of subjects (<https://diconlab.org/devmind>). This in-house project, of which the MBB lab at Tulane is a member, seeks to evaluate attention, cognitive control, and working memory using a battery of cognitive tasks, neuroimaging (including dynamic functional networks), and (epi)genetic data. Here (epi)genetic refers to the inclusion of DNA methylation data along with SNPs and whole genome sequencing [112]. The project is ongoing and currently data for more than 200 participants aged 9-14 years old has been collected. The dataset is unique because it is one of the few large datasets containing both fMRI, MEG, and genomic data alongside cognitive battery and

questionnaire data.

- **ABIDE.** The Autism Brain Imaging Data Exchange (ABIDE) dataset ([http://fcon\\_1000.projects.nitrc.org/indi/abide/](http://fcon_1000.projects.nitrc.org/indi/abide/)) contains neuroimaging data for both healthy controls and autism spectrum disorder (ASD) patients. ABIDE I, released in 2012, contains functional and structural MRI data for 1,112 subjects, with 539 individuals with ASD and 573 healthy age-matched controls [113]. ABIDE II, released in 2017, adds an additional 487 individuals with ASD 557 controls, for a total of 2156 unique cross-sectional datasets [114]. The two datasets are focused on providing functional information as well as allowing for the elucidations of voxel-wise differences between ASD patients and healthy controls. The dataset is large enough to enable, for example, the identification of differences between subgroups as well as sex-based differences. The dataset is slightly skewed towards having a majority of males, with 360 ASD males in the ABIDE I dataset compared with 213 ASD females. Ages of subjects range from 7 to 64 years old.
- **ADNI.** Neuroimaging studies may help shed light on both normal development during advanced age as well as in developing clinical pathologies. For this reason, the large longitudinal Alzheimer’s disease neuroimaging initiative (ADNI) cohort (<https://adni.loni.usc.edu>) was created in 2003 with 819 subjects, 229 of whom were cognitively normal, 398 who had mild cognitive impairment (MCI), and 192 who had a diagnosis for Alzheimer’s disease [115]. The ADNI cohort continues to recruit subjects up to the present day. There have been several releases of ADNI data. The ADNI-2 dataset contains 757 subjects, of which there are 283 normal controls, 380 MCI patients, and 144 with Alzheimer’s disease [116]. Subjects have been recruited from 50 sites within the U.S., with implications for analysis due to the confounding factors of site-specific effects.

ADNI and datasets like it are often used for the validation of new machine learning models seeking to enhance predictive accuracy [117].

- **ABCD.** The Adolescent Brain Cognitive Development (ABCD, <https://abcdstudy.org/>) study is a very large longitudinal study enrolling approximately 11,800 children aged 9-10 at baseline, and following many of them for an extended number of years [118]. The study aims to be the largest study of brain development and behavior to date, consisting of 21 different universities and study sites. It is also specifically constructed to create a socio-economically diverse sample representative of the U.S. population as a whole [119]. Originally created to identify brain endophenotype factors that may lead to substance use disorders (e.g., cannabis), the aims of the study have expanded to include all psychosocial correlates of behavior and mental health [118]. The ABCD dataset contains a large number of questionnaire and cognitive battery fields as well as genetics and many types of MRI data: structural, diffusion, resting state fMRI, and task-based fMRI.
- **UKB.** The UK Biobank (<https://www.ukbiobank.ac.uk/>) is a nationwide initiative in the United Kingdom to collect de-identified health metrics from a large number of late middle aged and elderly participants. The UKB contains various data from more than 500,000 subjects, including genetic data, health record information, and questionnaire data [120]. In addition, it contains fMRI imaging data for a subset of more than 40,000 participants, including around 2,800 that have longitudinal neuroimaging scans, that is, scans taken at different points in the subjects' lives several years apart [121]. Not all data is available for all subjects, and only a small number of subjects have diagnoses for any particular disease, for example, 2,090 subjects in the UKB have a diagnosis for Alzheimer's disease [122], although most UKB AD subjects do not have

neuroimaging data.

## 1.4 Challenges in Neuroimaging and Neuroscience

Although advancements in imaging and AI have led to numerous successes in understanding of brain function and diagnosis of psychiatric and neurodegenerative diseases, many challenges remain to be answered in this field. A list of the major challenges is given below.

- **Data collection quality.** In studies of the human connectome, ensuring that data is acquired in a robust and repeatable manner is an important step. For example, involuntary or unconscious participant head movement can lead to significant artifacts and can distort the data or create significant biases [123, 124]. Researchers use a variety of techniques to counter these phenomena, including preventative measures such as instructions to participants, physical restraints, and post-processing techniques to regress out the effect of motion [125–127]. Effectively removing the effects of confounders is important for the validity of neuroimaging studies and the conclusions gleaned from them.
- **Longitudinal vs. cross-sectional studies.** In clinical studies it is relatively easy to recruit even large numbers of subjects, but it is harder to follow subjects over a multi-year period. For example, the UK Biobank has over 40,000 subjects with neuroimaging data but only slightly more than 2,722 that have longitudinal neuroimaging data [121]. This may be because of the additional time and cost burden they place on both the subject and investigator [128]. In spite of this, longitudinal studies are preferred in neuroimaging because they eliminate many sources of demographic bias and are able to show changes in the same subjects due to changes in age, lifestyle, disease progression, medication, etc. [129]

- **Security and privacy.** Ensuring the security and privacy of participants in neuroimaging studies while facilitating interoperability with regards to patient data poses unique challenges [130]. Having robust data protection measures, including encryption and data audits, is essential for protecting patient data [131, 132]. Robust data security practices are required not only from a technical standpoint but also from the standpoint of ethical obligations. One commonly used tool is the de-identification of MRI scans by hiding facial features [107]. At the same time, standardized data formats are required for interoperability between different research groups [133].
- **Sample size and curse of dimensionality.** Neuroimaging data often contains millions of features per subject [10], combined with small numbers of enrolled subjects, and this is called the curse of dimensionality. MRI studies tend to recruit fewer than 30 subjects, and it has been shown that 36 subjects is the minimum number required for good reproducibility of study conclusions [103, 134]. This requires the development of specific algorithms for low sample size studies combined with robust false discovery rate correction [135].
- **Multi-site harmonization and elimination of site-specific effects.** Multi-site studies that pool their data require specialized protocols to compensate for the different scanner parameters present at each of the sites [136]. Variation in scanner construction, imaging protocol, and imaging parameters can lead to significant differences in the characteristics of resulting images. Reaching full data standardization requires aligning protocols, scanner parameters, and subject instructions. When full standardization becomes impossible, advanced statistical techniques must be used to eliminate sources of site-specific bias [137].
- **Demographic confounds.** Similar to the problem of site-specific effects described above, correlations among features of interest and demographics can

result in unintentional inclusion of bias and masking of signal of interest [138]. Many of the same techniques used for statistical elimination of site-specific effects may also be used to attempt to eliminate sources of demographic bias [139].

## 1.5 Overview of Thesis

This thesis is structured in five chapters. This, the first chapter, gives a comprehensive introduction to neuroimaging and connectomics and conveys the uses for and limitations of current neuroimaging studies.

The second chapter will investigate how brain connectomics change with age in the large UKB dataset. In particular, it will show an increase in functional connectivity both in the cross-sectional and longitudinal cohorts with increased age, especially in the somatomotor-visual system connection.

The third chapter will present a machine learning algorithm that is effective at the low subject numbers and high feature dimensionality found in most fMRI studies. It will also present a tree-based feature selection algorithm that is superior to post-hoc saliency-based feature selection. Finally, it will investigate the fusion of neuroimaging and genomic data via contrastive learning.

The fourth chapter will give a description of a software package developed to quickly analyze functional connectivity and omics datasets in a graphical, browser-based environment. It will describe the identification of a significant race confound in functional connectivity data. It will also describe the effects of demographics on functional connectivity and genomic-based predictions.

Finally, the fifth chapter will recapitulate all the work described in this thesis and present ideas for potential future directions.

# Chapter 2

## Age-Related Changes in Functional Connectivity in the UKB

### 2.1 Introduction

Functional magnetic resonance imaging (fMRI) is a non-invasive technique that has proven indispensable for investigating human neural processes *in vivo* [2]. For example, it has been used to localize the areas associated with vision [140], attention [141, 142], emotion [143–145], and language [146] to specific regions in the cortex, or at least find the regions that are most significantly involved in a specific task. Functional connectivity (FC) is a quantity derived from fMRI that measures the time correlation of blood oxygen level-dependent (BOLD) signal between different regions in the brain [147]. FC has recently been used to predict age [148, 149], sex [150, 151], race [83], psychiatric disease status [152, 153], and pre-clinical Alzheimer’s disease [23]. Efforts to predict general fluid intelligence, although common [151], are thought by some to be confounded by differential achievement score distribution among ethnicities and the strong presence of race signal in FC [83]. FC has proven effective in predictive studies because of its simplicity and its robust representation of complex BOLD sig-

nal activity, as evidenced by high subject identifiability across different scanner tasks and across time [154, 155].

Besides being used as a predictive tool, FC has been observed to undergo changes throughout the lifespan. For example, connectivity in young children is generally very high between all brain regions and decreases while also becoming more modularized during and after puberty [156]. The FC of males and females is also quantitatively different, with females having higher intra-DMN connectivity and males having relatively greater connectivity between the DMN and other networks, although there is a wide degree of individual variation [157, 158]. Meanwhile, studies have shown that changes occur in the DMN during late middle and old age [159], although the exact direction of change in FC does not always appear constant [160]. In addition, various studies have examined age-related changes in the cingulum and medial temporal lobe [161, 162]. Given the recent interest in using fMRI to predict pre-clinical Alzheimer's disease,[23, 160] we believe a knowledge of ordinary changes in FC during old age is essential. This is especially true because it has been shown that a confounder can easily be mistaken for a true signal indicative of, e.g., general fluid intelligence or achievement score [83].

This study uses the longitudinal cohort of the UKB[120] to examine changes in the FC of individuals after an average of two years, the time between longitudinal scans. The UKB population of subjects with fMRI scans is predominantly (98%) Caucasian, ruling out race as a possible confounding effect. Additionally, we investigate changes in FC in longitudinal sub-populations based on subject age and sex. We find that average FC between the Somatomotor and Visual (SMT-VIS) networks increases on average from the first scan to the second, and that SMT and VIS-related connectivities are more predictive of scan age than those of other networks. The complete FC, or a large subset, is still required to attain the best accuracy.

## 2.2 Methods

We first describe the UKB dataset and the longitudinal subset used for our analysis. We then describe pre-processing of the fMRI data and conversion into FC. Finally, we discuss prediction of older vs younger scan in the longitudinal cohort and detail our methods for analysis of FC changes.

### 2.2.1 UK Biobank Longitudinal Cohort

The UKB contains various data of more than 500,000 subjects in the UK, of whom more than 40,000 have fMRI scans [120]. We processed two longitudinal resting state scans for 2,722 subjects, taken approximately two years apart. These subjects are approximately equally split between male and female, and have significant numbers of younger and older adults. The longitudinal cohort is composed of 1,289 genetic males and 1,369 genetic females, with the rest not having genetic sex information. The ethnicity of the subset of the UKB with fMRI scans is 98% Caucasian. Besides the 2,722 subjects we processed, an additional 154 subjects have the second longitudinal scan but not the first, resulting either from missing original source data or a failure in our SPM12-based preprocessing pipeline. Additionally, we perform analysis on the UKB working scanner task [163, 164], which includes a total of 2,360 longitudinal subjects, compared with the 2,722 subjects having resting state longitudinal scans.

### 2.2.2 fMRI Preprocessing

The original scan acquisition parameters are described elsewhere [163, 165], but consist of both resting state and task fMRI scans with a repetition time of TR = 0.735 sec. All resting state 4D fMRI volumes were processed with SPM12, including co-registration and warping to MNI space (<http://www.fil.ion.ucl.ac.uk/spm/software/spm12/>). BOLD signal was extracted using the Power264 atlas [5], which

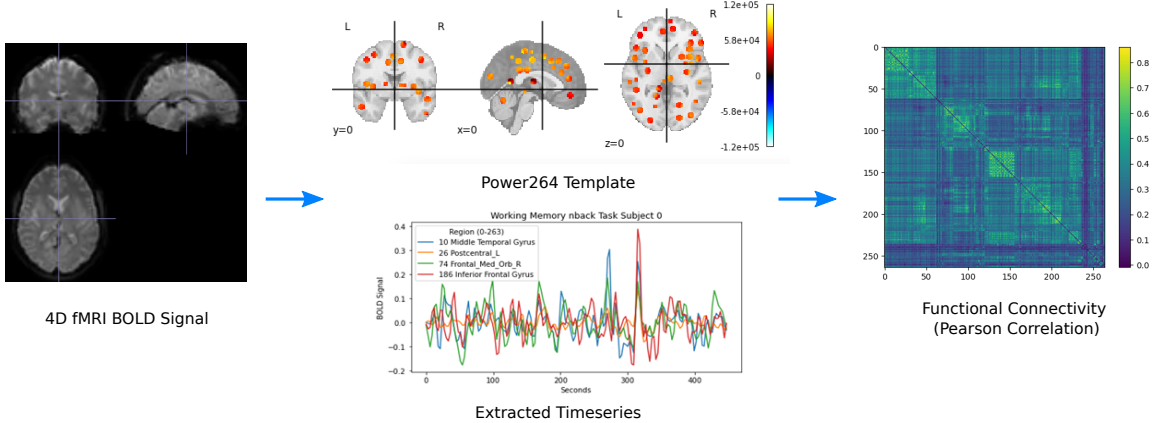


Figure 2.1: Preprocessing pipeline for converting 4D fMRI volumes into FC using the Power264 atlas [5].

consists of 264 ROIs grouped into 14 functional networks, with the ROIs represented by 5mm radius spheres. The resulting timeseries were bandpass filtered between 0.01 and 0.15 Hz to remove scanner drift, noise, heartbeat, and some breathing signal. Pearson correlation of the filtered timeseries was used to create subject-specific FC matrices, which were reduced to the 34,716 unique entries in the upper right triangle and vectorized. The entire procedure is summarized in Figure 2.1.

In contrast to the Power264 atlas-derived FC constructed by us, the original UKB data provided the unique part of 21-region and 55-region FC and partial correlation-based connectivity (PC) matrices based on ICA in vectorized format [163]. These matrices were calculated through the use of PCA on whole cohort fMRI data followed by ICA [163], meaning that regions overlap in an unpredictable way and are not associated with specific functional networks. Although prediction using 55-component ICA-based FC and PC is often as good as and sometimes better than prediction using Power264 atlas-derived FC, the resulting connectivities are uninterpretable with regards to BOLD signal within specific regions. Additionally, in predicting which scan is older, Power264 asymptotes to a higher predictive accuracy than either of the ICA-derived measures (see Figure 2.4).

### 2.2.3 Prediction of Scan Age and Analysis of FC

Prediction of scan age in the UKB longitudinal cohort was carried out by logistic regression (<https://scikit-learn.org/stable/>) models with 20 bootstrapping repetitions, using the scikit-learn implementation [166]. The regularization parameter was fixed to  $C = 1$ , which was found to be near the optimal value for all training set sizes using grid search. Prediction was carried out using the difference of vectorized FC matrices as input features, and scan order (younger scan minus older [0] or older scan minus younger [1]) as the prediction target. It was found that a simple difference of the two longitudinal scan FCs gave the best prediction results compared with concatenation or difference and concatenation, using either logistic regression or MLP. The training set was created with randomization of whether older scan was subtracted from younger scan or younger scan was subtracted from older scan. Predictive ability was tested at various training set sizes, from 50 to 2,000 subjects, with the remaining subjects forming the test set. In addition to the resting state scanner task, we have repeated this analysis for the UKB working scanner task, a faces/shapes emotion identification task [163, 164]. We also include a comparison with average FC differences due to different scanner tasks as found in the widely-used Philadelphia Neurodevelopmental Cohort (PNC) dataset [60], computing the mean FC differences for combinations of scanner tasks (resting state, working memory, or emotion identification). Our code for computing prediction accuracy can be found online (<https://github.com/aorliche/ukb-longitudinal-smt-vis>). However, UKB data sharing policy precludes us from posting the longitudinal data itself; interested researchers may contact us with any questions.

Analysis of FC was performed by finding the mean (Figure 2.2) and standard deviation (Figure 2.12) of older scan FC minus younger scan FC for the longitudinal cohort. Additionally, prediction of scan order was carried out using the average connectivity between each of the Power264 networks, each network consisting of many

individual ROIs. As before, logistic regression with 20 bootstrap repetitions and  $C = 1$ , with 2,000 subjects in the training set and the rest in the test set, was used for this purpose. A Bonferroni-corrected two-sided t-test was applied to the 105 average inter-network connectivity differences (from the complete graph of 14 functional networks) of the 2,722 longitudinal subjects to determine if they were significantly different from zero (Figure 2.5 Bottom). Finally, we examine changes in FC in the UKB cross-sectional cohort, which contains 23,672 younger (< 55 years old) and older (> 65 years old) male and female subjects, also using a two-sided t-test with p-values adjusted by Bonferroni correction.

## 2.3 Results: Somatomotor-Visual Connectivity Increases with Age

We first describe trends in FC changes during the two years or more between longitudinal scans, summarize the ability of simple machine learning models to identify older vs younger scan, and investigate the ability of specific inter-network connectivities to predict scan order. We then summarize the statistical significance of inter-network FC changes with aging, in both the longitudinal and cross-sectional cohorts of the UKB. Next, we consider the possibility that the observed longitudinal changes are due to a change in scanner task by presenting inter-task FC differences in the PNC dataset [60]. Finally, we confirm the presence of increased longitudinal SMT-VIS connectivity in the UKB working task scan in addition to the UKB resting state scan.

### 2.3.1 Inter-network FC Changes

In Figure 2.2, we show that, on average, SMT-VIS connectivity increases from younger scan to older scan. The right hand side of Figure 2.2 displays divisions of the 14 functional networks included in the Power264 atlas. Network labels and abbreviations

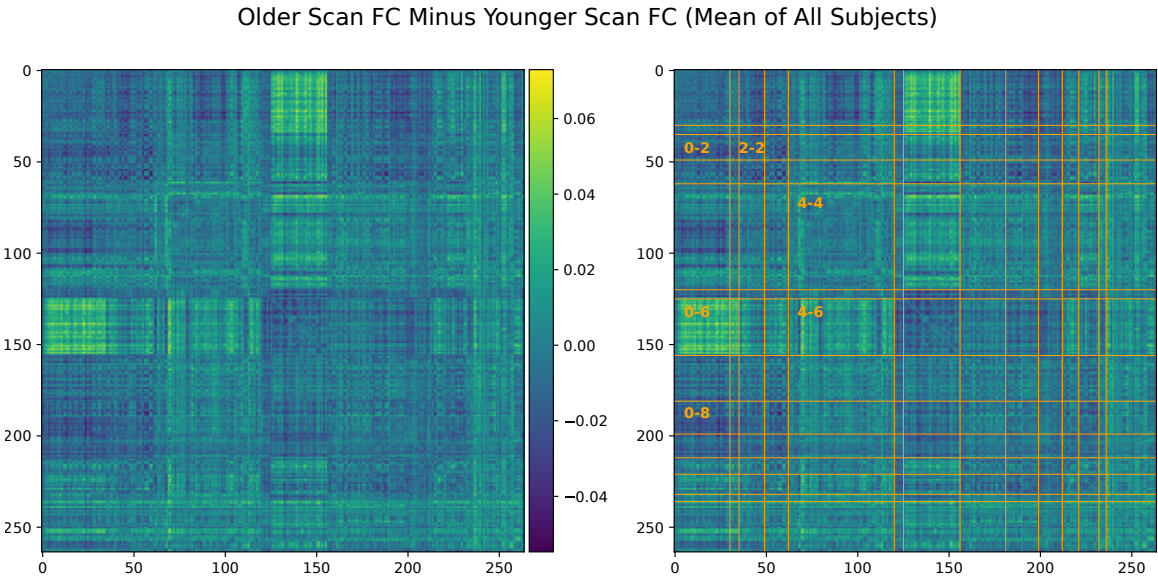


Figure 2.2: Difference in FC calculated by older scan minus younger scan, averaged over all 2,722 longitudinal cohort subjects. There are significant average differences in SMT-VIS connectivity (labeled 0-6). The same plot is displayed on the left and right, with Power264 network divisions on the right hand side. Network labels can be found in Table 2.1.

**Functional Networks**

Label	ROIs	Network	Label	ROIs	Network
0	0-29	Somatomotor Hand (SMT)	7	156-180	Frontoparietal (FRNT)
1	30-34	Somatomotor Mouth (SMT)	8	181-198	Salience (SAL)
2	35-48	Cinguloopercular (CNG)	9	199-211	Subcortical (SUB)
3	49-61	Auditory (AUD)	10	212-220	Ventral Attention (VTRL)
4	62-119	Default Mode (DMN)	11	221-231	Dorsal Attention (DRSL)
5	120-124	Memory (MEM)	12	232-235	Cerebellar (CB)
6	125-155	Visual (VIS)	13	236-263	Uncertain (UNK)

Table 2.1: Regions, abbreviations, and labels in the Power264 atlas.

are listed in Table 2.1. The increase in connectivity is large and distinct over the majority of SMT-VIS FCs compared with other non-SMT and non-VIS FCs. Many FCs involving the VIS network appear to increase in connectivity from the first scan to the second. The average change in FC in the SMT-VIS connection is 6.8%, corresponding to a mean change  $\mu_{\Delta\rho} = +0.03$ , compared with a standard deviation of  $\sigma_{\Delta\rho} = 0.26$ . Figure 2.5 shows that, due to the large number of subjects, this difference is very statistically significant.

Figure 2.3 displays the same analysis, i.e., the average FC change from first scan

to second, for four subsets of the cohort. These subsets are male subjects, female subjects, young ( $< 55$  years old) subjects, and old ( $> 65$  years old) subjects. All four subsets showed the same patterns of changes in FC as the whole cohort, thus we rule out very old age or gender as confounding factors.

### 2.3.2 Identification of Older Scan of Pair

In Figure 2.4, one can see that it is possible to predict which scan of a longitudinal pair is older with the Power264 atlas at an accuracy of 82.5%, having 2,000 subjects in the training set and the rest in the test set. This measurement was repeated with 20 bootstrap iterations and averaged. The entire 34,716-feature upper right triangle of the FC matrix was used to make the prediction. One can also see that the ICA FC/PC matrices provided pre-processed by the UKB curators along with the UKB data are also able to predict scan order, although at a slightly reduced accuracy. Prediction is possible at an accuracy of 60-70% using only 100-200 training set subjects. This shows an expected dependence of accuracy of test set prediction of scan order on training set size. Note that most machine learning models will perform better on the training set than the test set. Overfitting, where the prediction accuracy is high on the training set but close to or worse than the null model (50%) on the test set, is not observed.

### 2.3.3 Prediction of Scan Age Using Specific Inter-network Connections

In Figure 2.5, we rank average inter-network FCs in their ability to predict scan order. As expected from the mean change in FC (Figure 2.2), the SMT-VIS connection is the most predictive of longitudinal scan age. Furthermore, SMT and VIS networks are included among the next several most predictive inter-network connections. In



Figure 2.3: Significant increase in SMT-VIS connectivity after an average of two years in the UKB longitudinal cohort appears in male, female, younger, and older groups, and seems to be an invariant feature of FC change in the longitudinal UKB cohort. SMT and VIS regions in the Power264 atlas are visualized in Figure 2.6.

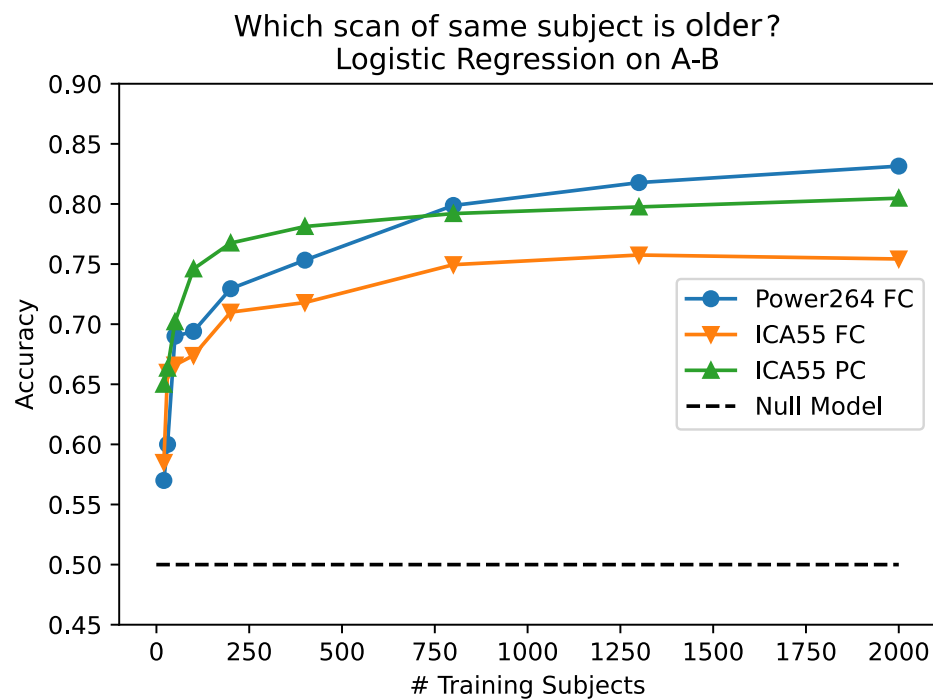


Figure 2.4: Capability of predicting older scan of a pair based on the difference of FC between the two scans, as a function of the number of training subjects. Three inputs are used: 55 component ICA FC, 55 component ICA PC, and the Power264 atlas FC. Prediction accuracy as displayed is on the test set, not the training set, and asymptotes at 82.5%.

Group	+SMT-VIS FC	-SMT-VIS FC	+Total FC	-Total FC	Total Subjects
Male	778 (60.4%)	511	690 (53.5%)	599	1289
Female	741 (54.1%)	628	671 (49.0%)	698	1369
< 55 years old	269 (59.0%)	187	249 (54.6%)	207	456
> 65 years old	577 (56.5%)	445	520 (50.1%)	502	1022

Table 2.2: Number of subjects in the longitudinal cohort increasing and decreasing in average FC within the SMT-VIS connection and within the whole brain.

Figure 2.5 bottom, we plot the predictive ability of all 105 inter-network connections, along with a p-value for the inter-network FC change being significantly different from zero. The raw p-value has been multiplied by 105 to account for multiple comparisons. It is highly significant for the first 10 or so most predictive inter-network connections, and we find a p-value of  $p < 10^{-15}$  for the increase in SMT-VIS connectivity from the first longitudinal scan to the second.

Table 2.2 lists the number of subjects whose FC increased or decreased for the SMT-VIS connection and over the entire brain. The table is divided among the four subsets of the longitudinal cohort mentioned previously. Additionally, we correlated several dozen subject phenotypes and longitudinally-tracked variables with changes in FC and report the most significant in Section 2.3.7. In that section, we find an interesting but small correlation with hand grip strength, body mass index (BMI), and basal metabolic rate. In Section 2.3.4, we find that average resting state FC increases with age across most inter-network connections in the much larger UKB cross-sectional cohort.

### 2.3.4 FC Changes with Age in the UKB Cross-sectional Cohort

We find that average resting state FC has a significant increase in almost all inter-network connections in the UKB cross-sectional cohort. Average maps of FC change are shown in Figure 2.7. We fail to find a higher SMT-VIS change as compared with

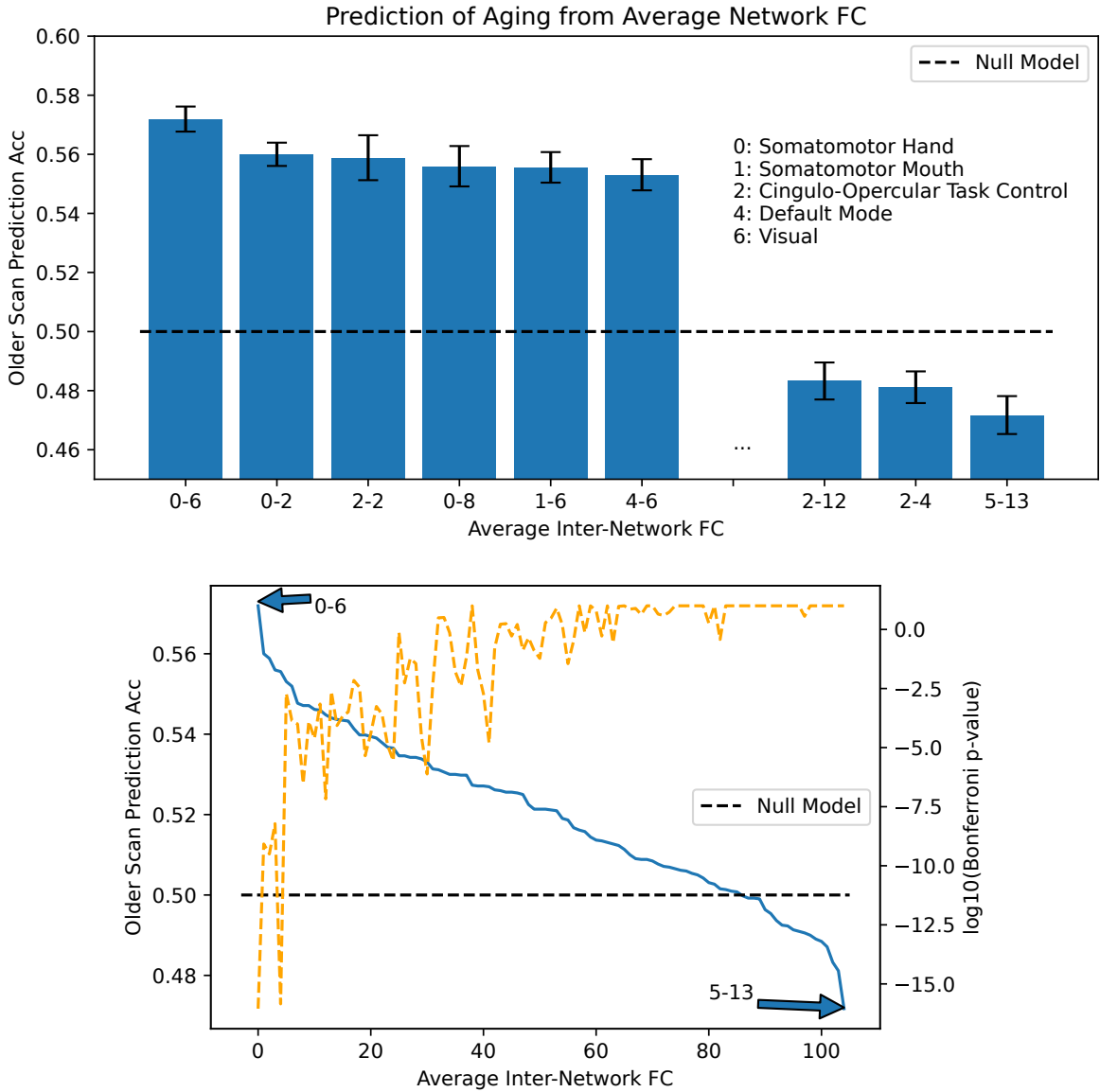


Figure 2.5: Ability to predict which scan of a subject is older based on average connectivity between regions. Top: best and worst inter-network connectivities for prediction. Bottom: Prediction accuracy for all 105 inter-network connectivities. We find that SMT-VIS connectivity has the maximum predictive ability of all regions at 57%. In general, network-level connectivities involving SMT and VIS networks have higher predictive ability as compared with other regions. The dashed orange line displays log base 10 of the Bonferroni-corrected p-value for significance of FC change between scans. Note the Bonferroni-corrected p-value for the observed SMT-VIS connectivity increase is  $p < 10^{-15}$ .

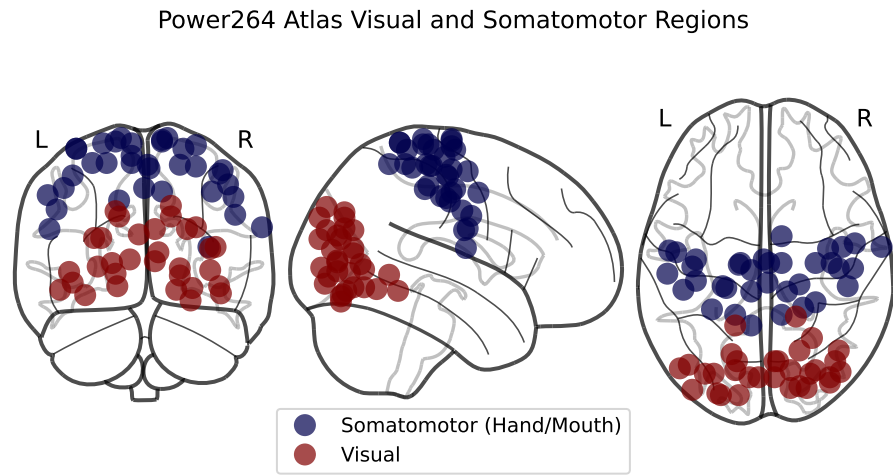


Figure 2.6: SMT and VIS regions in the Power264 atlas.

other connections; however, almost all inter-network regions have a large positive change in FC with aging. We give precise numbers for four inter-network connections as well as total FC in Table 2.3. In total, there are 9,387 older males ( $> 65$  years old), 2,425 younger males ( $< 55$  years old), 8,728 older females ( $> 65$  years old), and 3,132 younger females ( $< 55$  years old) in the UKB cross-sectional cohort.

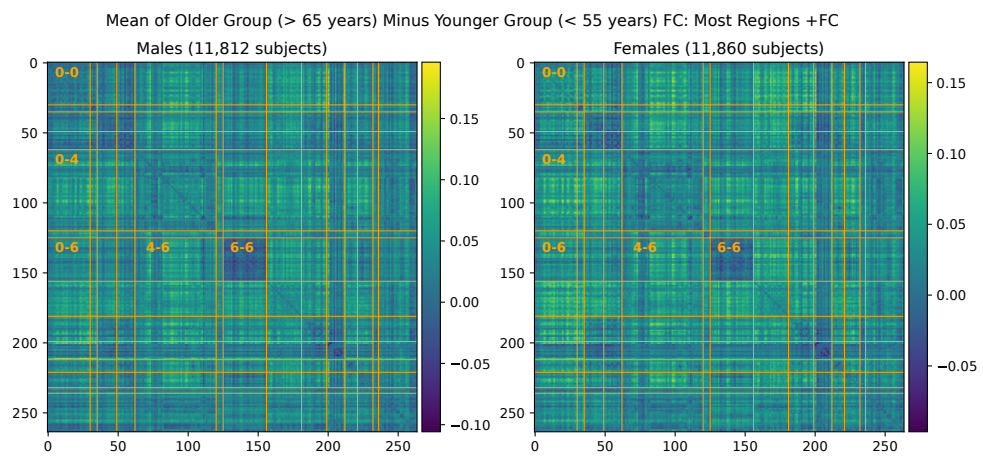


Figure 2.7: Mean FC change from younger group to older group in the large UKB cross-sectional cohort.

Regions	Male (Young to Old)			Female (Young to Old)		
	FC Increase	Std Dev of Avg FC	p-value	FC Increase	Std Dev of Avg FC	p-value
SMT-VIS (0-6)	0.031	0.13	< 10 <sup>-23</sup>	0.029	0.13	< 10 <sup>-25</sup>
SMT-DMN (0-4)	0.045	0.11	< 10 <sup>-78</sup>	0.043	0.11	< 10 <sup>-82</sup>
DMN-VIS (4-6)	0.042	0.11	< 10 <sup>-60</sup>	0.035	0.11	< 10 <sup>-52</sup>
VIS-VIS (6-6)	-0.014	0.10	< 10 <sup>-7</sup>	-0.009	0.11	< 0.002
Total FC	0.035	0.09	< 10 <sup>-64</sup>	0.031	0.087	< 10 <sup>-62</sup>

Table 2.3: Average FC changes with aging in the UKB cross-sectional cohort from young subjects (< 55 years old) to old subjects (> 65 years old). SMT=Somatotmotor Network, VIS=Visual Network, DMN=Default Mode Network, FC=Functional Connectivity

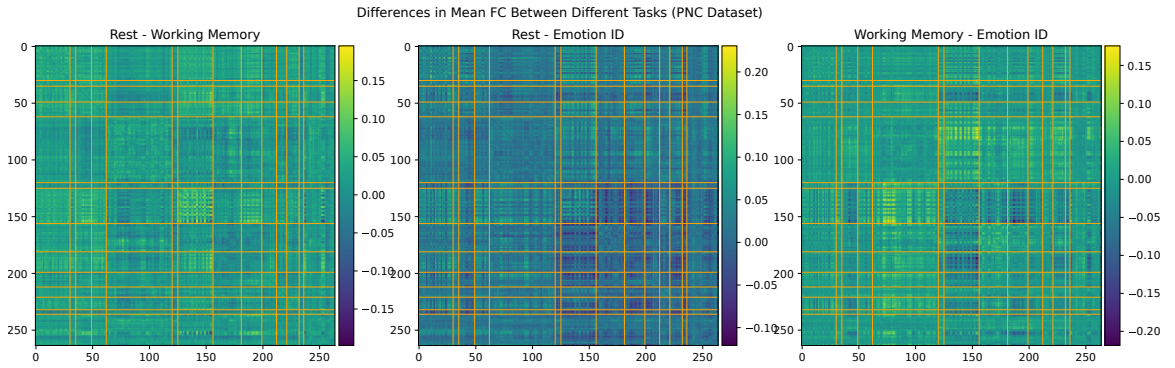


Figure 2.8: Average differences in FC between three scanner tasks of 1,345 subjects in the PNC dataset. This is a cross-sectional, not longitudinal, dataset.

### 2.3.5 Comparison with Different Scanner Tasks in the PNC Dataset

We consider the possibility that the difference in SMT-VIS connectivity between the two scans of the longitudinal cohort is due to a change in scanner task. In Figure 2.8, we show the average FC differences between 3 different tasks in the PNC dataset.[60] This dataset contains 1,345 children and young adults having all of three different scanner tasks: resting state, working memory, and emotion identification. The pre-processing and FC creation steps for this dataset have been described elsewhere.[148] We note that VIS-VIS connectivity has the greatest average difference between different tasks, and that the change in SMT-VIS connectivity is not qualitatively more different than for other inter-network connections. Also, the magnitude of change in FC in the PNC dataset between tasks is much larger than in the UKB longitudinal cohort. We observe a  $\Delta\rho = 0.03$  average change in SMT-VIS connectivity in the UKB longitudinal cohort compared with a  $\Delta\rho > 0.05$  average FC change in some inter-network connections between different scanner tasks in the PNC dataset.

### 2.3.6 Validation on UKB Working Task

In addition to the resting state scanner task, the UKB had fMRI scan participants undergo a faces/shapes emotion identification task.[163][164] As validation for the findings of increased SMT-VIS connectivity in resting state scan data, we performed the same analysis described previously for the resting state scanner task on the longitudinal cohort working task scan. The number of subjects with working scanner task was smaller than for the resting state, with 2,360 working task subjects compared with 2,722 resting state task subjects. As shown in Figure 2.9 top, one can see the same qualitative pattern of FC changes in the working task as in the resting state task. Additionally, Figure 2.9 bottom shows that the working state FC has can predict which scan is older at least as well as the resting state FC.

### 2.3.7 Correlation of Longitudinal FC Changes with Health Outcomes

We identified several correlations between longitudinal change in FC and changes in clinical outcomes associated with the two scan timepoints in the UKB dataset. These are presented below, along with the UKB field identifiers of the outcomes. All p-values are Bonferroni-corrected with  $n = 105$  multiple comparisons (one for each average inter-network connectivity).

#### SMT Hand, VIS, and CB Connectivity and Grip Strength (f.46.2.0, f.46.3.0, f.47.2.0, f.47.3.0)

We find a marginally significant association between change in hand grip strength and VIS-CB and SMT-CB connectivity change (Figure 2.10).

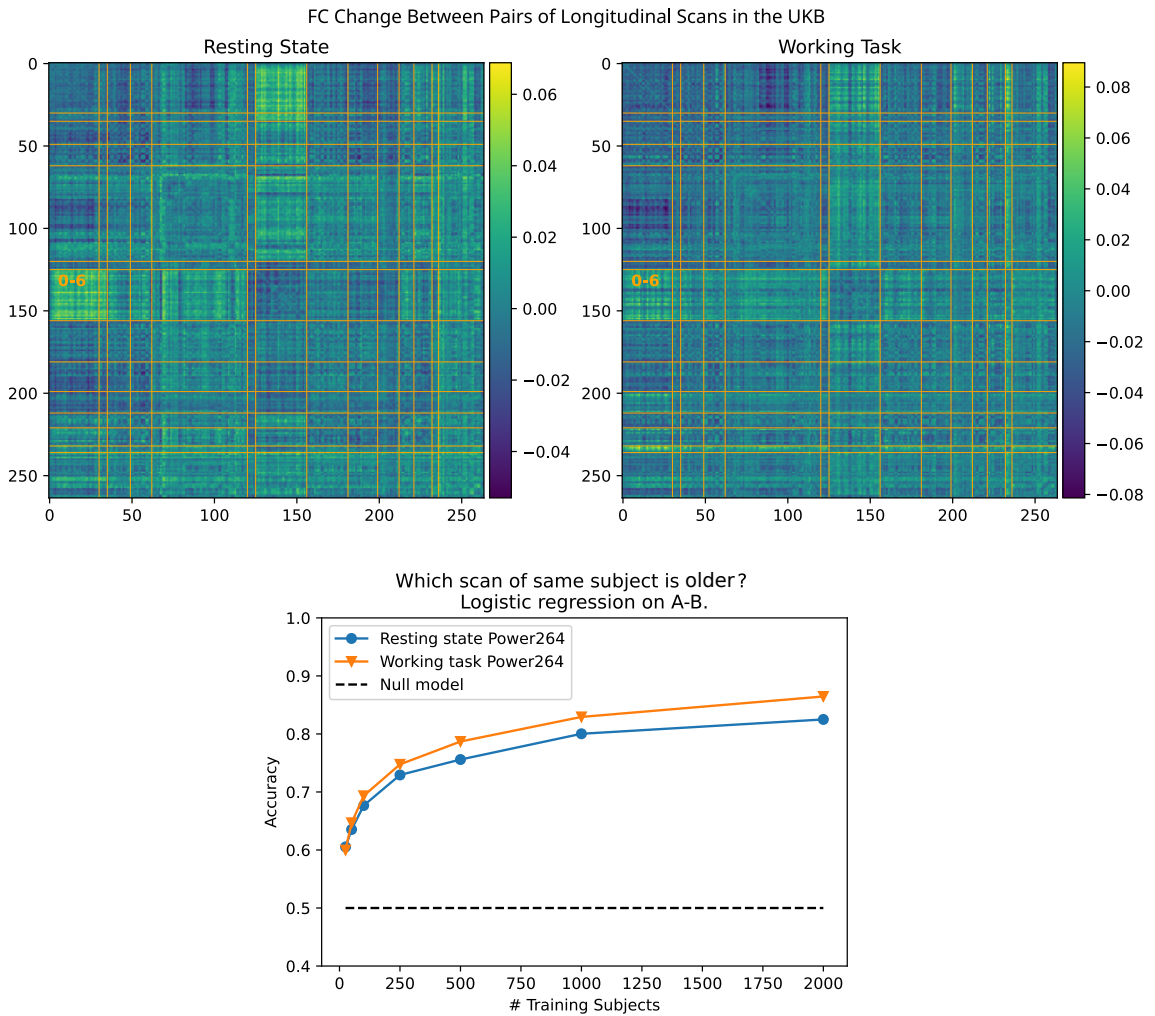
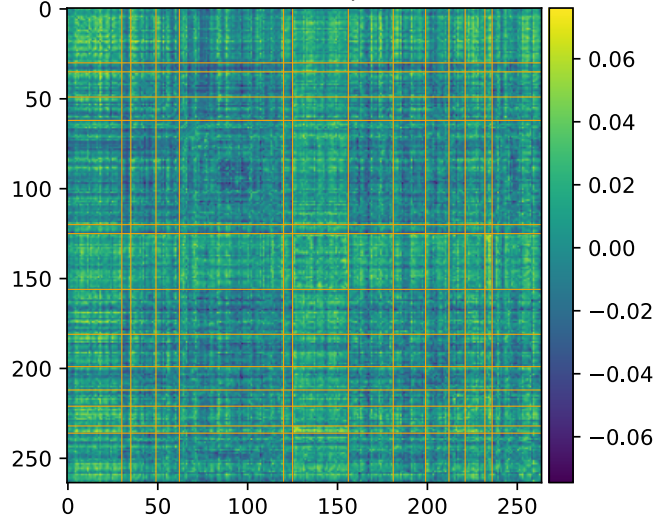


Figure 2.9: Top: Comparison of resting state with working task average FC change in the longitudinal cohort. We see qualitatively the same pattern, with high SMT-VIS connectivity change along with high change for other VIS-connected FCs. Bottom: Ability to predict which of a scan pair from a single subject was older, using resting state and working task FC data. We find that it is slightly easier to predict scan age in the longitudinal cohort using the working scanner task than resting state scanner task.

FC Change Correlation with Hand Grip Strength Change (Left)  
Vis-CB (6-12):  $p < 0.27$



FC Change Correlation with Hand Grip Strength Change (Right)  
SMT-CB (0-12):  $p < 0.09$ , VIS-CB (6-12):  $p < 0.56$

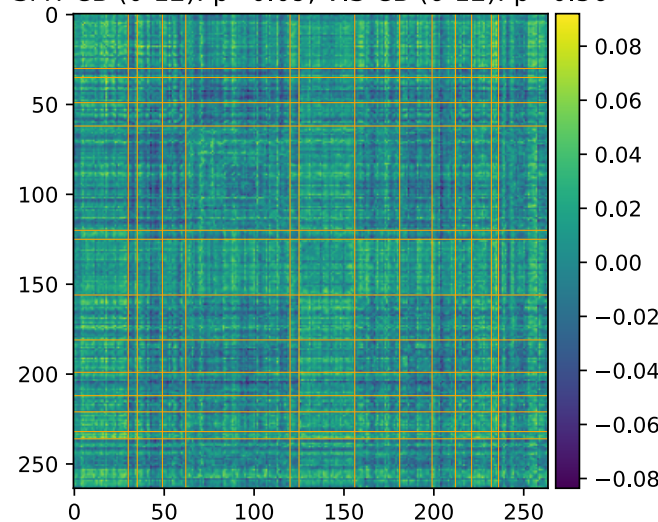


Figure 2.10: Hand grip strength change association with functional connectivity change in the longitudinal cohort. Bonferroni-corrected p-values.

## Body Mass Index and Basal Metabolic Rate (f.23104.2.0, f.23104.3.0, f.23105.2.0, f.23105.3.0)

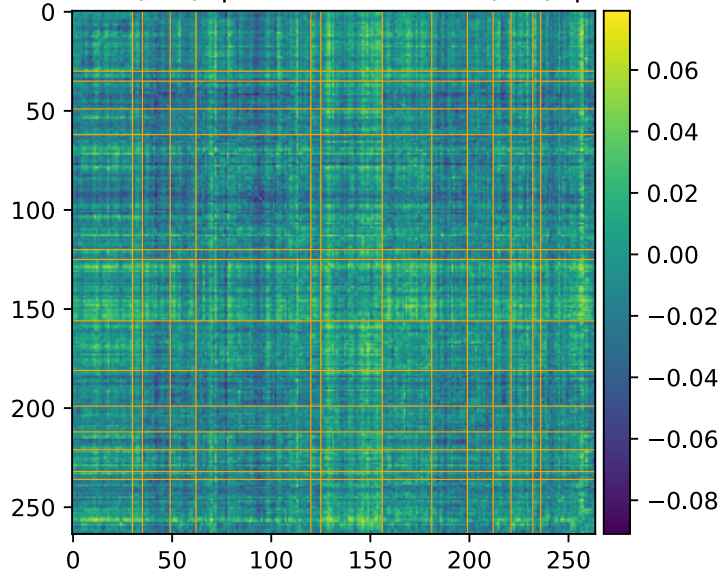
We find a not statistically significant but suggestive association between BMI and basal metabolic rate change and SMT-VIS connectivity change (Figure 2.11).

## 2.4 Discussion

*Farràs-Permanyer et al.* (2019) [167] found that mean resting state FC may increase throughout the entire brain for the oldest subject ( $> 80$  years old) group. In another study, *Hafkemeijer et al.* (2013) [168] found that resting state FC increases in older adults with memory complaints. In Section 2.3.4, we show that there is a large, statistically significant increase in average resting state FC across almost all inter-network connections in the UKB cross-sectional cohort with increased age. This cross-sectional cohort is much larger than the longitudinal cohort we describe in the main part of this paper. The fact that SMT-VIS FC also increases in the cross-sectional cohort, but not disproportionately compared with the rest of FC, raises the possibility of a change in resting state scanner task during the second longitudinal scan. The credence given to this possibility should be reduced because we find a similar increase in the UKB longitudinal cohort working task, as described in Section 2.3.6. We believe this longitudinal change is not an artifact of our pre-processing methods. Confidence should increase in our pre-processing methods since the UKB-provided ICA-based FC and PC is also able to predict longitudinal scan ordering at almost the same level as our Power264-based approach, although the ICA FC and PC matrices are not interpretable.

Many studies have focused on examining connectivity in the DMN associated with aging [169, 170]. These studies find areas of increased connectivity as well as areas of decreased connectivity. There are two problems with such studies. First, they are

FC Change Correlation with Body Mass Index Change  
CNG-CNG (2-2):  $p<0.12$ , CNG-AUD (2-3):  $p<0.76$



FC Change Correlation with Basal Metabolic Rate Change  
SMT-VIS:  $p<0.05$  (Uncorrected)

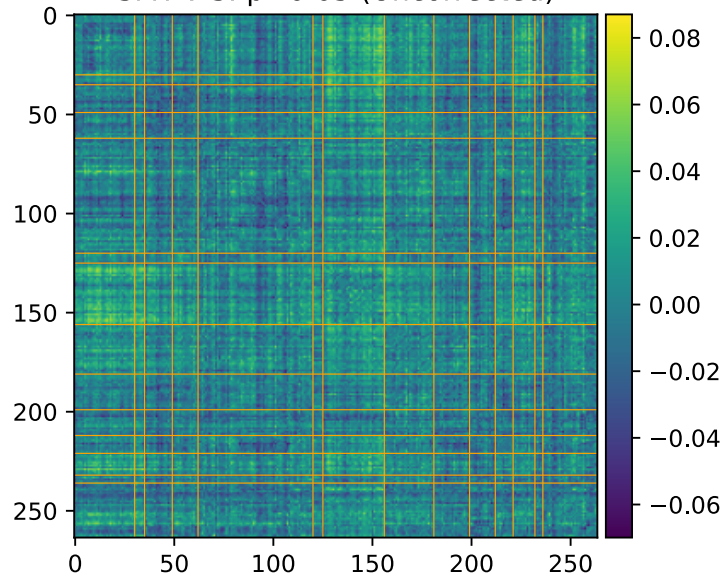


Figure 2.11: BMI and basal metabolic range change association with functional connectivity change in the longitudinal cohort. Bonferroni-corrected p-values.

for the most part cross-sectional and do not follow a single subject across a multi-year period. Second, they mostly use small numbers of subjects, the majority of studies enrolling fewer than 50, making it impossible to identify small effects. On the other hand, one study performed on a cohort of more than 2,000 older subjects in Rotterdam found age-related changes in connectivity to be complicated, drawing no firm conclusions [171]. We note that the Rotterdam study was not longitudinal but cross-sectional.

We conjecture the fact that most studies only focus on DMN and report decreased connectivity[169] in aging populations may be related to the large number of ROIs in the DMN and an implicit bias inherent in the word “connectivity.” Naturally, as we reach very old age we expect physical connections to degenerate, not become stronger. In fact, FC is really the synchronization of BOLD signal between regions, and does not imply a direct physical link between regions. Young children are known to have higher average FC than young adults;[156, 172] thus older subjects may be seen as reverting to a less optimal state as they age.

On the other hand, as we describe in Section 2.3.7, physical observables such as hand grip strength in the UKB longitudinal cohort are weakly correlated with an increase in FC in SMT-CB and VIS-CB connectivity. Additionally, we find BMI and basal metabolic rate are weakly correlated with the longitudinal increase in SMT-VIS connectivity (see Section 2.3.7). This may suggest a small health related effect that is found throughout the study cohort and includes male, female, younger, and older subjects.

We show in this work that the average connectivity increase in the SMT-VIS connection is small but highly statistically significant. The average change in FC in this connection is only 6.8%, corresponding to a mean change  $\mu_{\Delta\rho} = +0.03$ , compared with a standard deviation of change from subject to subject of  $\sigma_{\Delta\rho} = 0.26$  (see Figure 2.12). However, using our longitudinal sample of 2,722 subjects, we find

Standard Deviation of FC Difference Between Longitudinal Scans

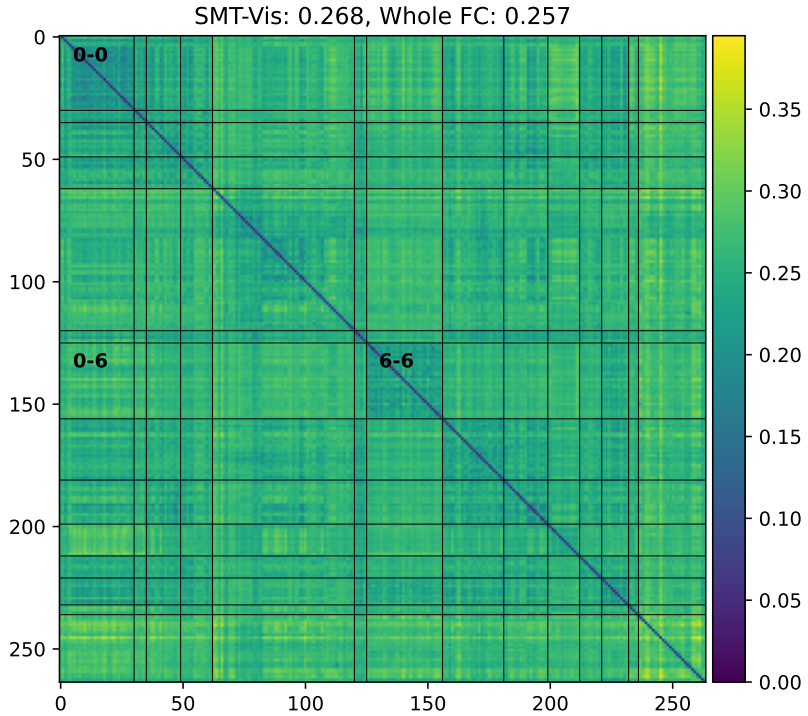


Figure 2.12: Standard deviation of difference between older scan FC and younger scan FC in the UKB longitudinal cohort. Note that the magnitude of average standard deviation (0.26) of SMT-VIS connectivity change is large compared with mean SMT-VIS connectivity change (0.03). However, we show in Figure 2.5 that this connectivity change is highly statistically significant. The smallest average standard deviations are found in SMT-SMT (0.2) and VIS-VIS (0.22) connectivities.

the average SMT-VIS connectivity change from younger scan to older scan is very significant after Bonferroni correction for multiple comparisons (Figure 2.5). Finding such small effects is helped by the use of large number of subjects and longitudinal data.

## 2.5 Conclusion

In this work, we pre-process a 2,722 subject longitudinal subset of the UK Biobank dataset and examine FC using the Power264 atlas. We find that in scans taken an average of two years apart, the average functional connectivity between SMT and VIS

network regions tends to increase at a Bonferroni-corrected p-value of  $p < 10^{-15}$ . This occurs in male, female, younger ( $< 55$  years old), and older ( $> 65$  years old) subject groups. We verify the ability of this average FC increase to predict scan ordering using simple machine learning models. The identification of an increase in connectivity with non-pathological aging, in longitudinal as well as cross-sectional cohorts, and specifically in the SMT-VIS synchronization of BOLD signal, may lead to novel insights about brain function in old age. The identified increase in SMT-VIS connectivity with aging could also appear as a confounder in future studies of dementia or neurodegenerative diseases, and should be guarded against. Finally, we rule out the possibility of a change in scanner task leading to the identified increase in resting state SMT-VIS connectivity by finding a similar increase in SMT-VIS connectivity in the UKB longitudinal working scanner task.

## Chapter 3

# Latent Similarity Model Identifies Important Functional Connections for Phenotype Prediction

### 3.1 Introduction

Functional magnetic resonance imaging (fMRI) provides a non-invasive estimate of brain activity by exploiting the blood oxygen level-dependent (BOLD) signal [2]. This high-acuity imaging data can be used to predict variables like age, sex, intelligence, and disease status [150, 173–175]. Interestingly, the gap between fMRI-predicted brain age and biological age can identify Alzheimer’s disease patients prior to the onset of symptoms [23]. Prediction is hindered, however, by the combination of small sample size and very high feature number. This results in models that have poor reproducibility and generalizability [104].

Studies with small sample size only have the power to detect very large effects. Many effects that are found in small studies may be due to noise. When identifying regions that are associated with in-scanner tasks, it was found that the average min-

imum cohort size needed to reproducibly identify the same region 50% of the time in independent samples was N=36 [134]. In contrast, models deployed clinically use thousands of subjects for training and validation [176]. In 2017 and 2018, the median cohort sizes for published experimental and clinical MRI studies were 23 and 24 subjects, respectively, and less than 1% of the 272 papers surveyed reported cohort sizes greater than 100 [103]. This may be attributed to both cost, at \$500-\$1000 per subject, and the difficulty of collecting the data, stemming from long scan times, subject discomfort in the scanner, and experimental design [103].

Additionally, for fMRI-based predictions to be useful clinically, they must be interpretable. There is a large literature on the interpretability of machine learning in medical imaging [177, 178]; however, there is often a tradeoff between model accuracy and interpretability. This raises questions about robustness in the clinical setting [179]. For example, *Zhang et al.* (2020) show that different processing methods can yield similar accuracy in a sex prediction task, but with different discriminative features identified by each method [180]. Identifying a minimal set of valid functional connections may increase model robustness, and make inroads into causal analysis of brain networks [181].

Finally, many recent studies in the deep learning field shift their focus to integrate data from multiple omics [182], or multiple omics and imaging [183]. This is done for two purposes: to improve prediction accuracy and to learn novel interactions between different modalities. CCA-based models have been proposed that use response variable-guided feature alignment [184, 185]. However, these models do not consider inter-subject relationships and cannot control disentanglement between different predictive tasks.

In this chapter, we introduce LatSim (Figure 3.1), a model in the spirit of metric learning [186], that is both robust and interpretable. Traditional machine learning (ML) models in fMRI, which work directly on functional connectivity (FC) [147],

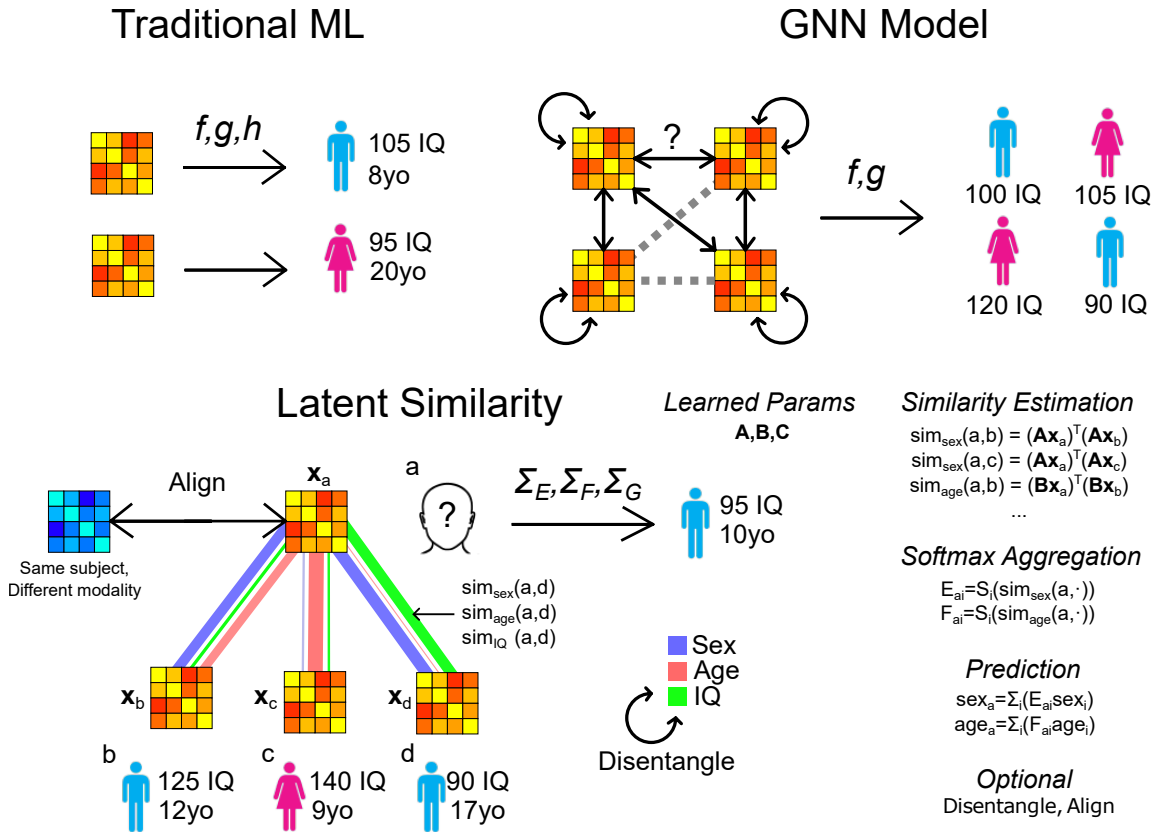


Figure 3.1: An overview of the Latent Similarity model. In traditional ML, estimation of response variables is decoupled from inter-subject similarity, whereas GNN models require additional degrees of freedom to estimate edges between subjects. Our model calculates similarity between subjects based on a set of response variables and incorporates multi-modal feature alignment (in addition to ensembling) as well as sparsity and feature disentanglement.

are vulnerable to noise or random confounders like scanner drift or head motion [187]. Graph neural networks (GNN) use inter-subject information as an adjunct to calculations performed directly on FC [188]. However, graph edges may be ambiguous or non-binary, requiring additional degrees of freedom for their estimation [189, 190]. In contrast, LatSim learns an inter-subject similarity metric,  $d(\mathbf{x}_a, \mathbf{x}_b)$ , and uses the inter-subject similarity, without a self-loop, to make predictions.

The contribution of this chapter is three-fold. First, we propose a novel metric learning-based model, LatSim, which is robust, interpretable, computationally efficient, multi-view, and multi-task. Second, we use LatSim and a greedy selection algorithm to identify the most discriminative connections for age, sex, and intelligence prediction among adolescents in the Philadelphia Neurodevelopmental Cohort (PNC) dataset [60]. We show that the such connections are superior to those identified by saliency maps. Third, we give a justification why LatSim performs better than traditional ML models with low sample sizes and high feature dimensionality. We make the code publicly available on GitHub (<https://github.com/aorliche/LatentSimilarity/>).

## 3.2 Methods

### 3.2.1 Kernel CCA

To compute similarity between subjects, we utilize ideas from canonical correlation analysis (CCA) [191, 192]. Conventional CCA seeks to find relationships between the features of two different views of a dataset. It aligns the two views,  $\mathbf{X}_1 \in \mathbb{R}^{N \times d_1}$  and  $\mathbf{X}_2 \in \mathbb{R}^{N \times d_2}$ , by finding canonical variables  $\mathbf{w}_1$  and  $\mathbf{w}_2$  that maximize the correlation between  $\mathbf{X}_1\mathbf{w}_1$  and  $\mathbf{X}_2\mathbf{w}_2$ :

Table 3.1: Commonly used notation.

Notation	Description
$\mathbf{X} \in \mathbb{R}^{N \times d}$	A matrix of dimension $N$ by $d$
$X_{ij}$	The $(i,j)$ -th entry of matrix $\mathbf{X}$
$\mathbf{X}_{i,:}$	The $i$ -th row of matrix $\mathbf{X}$
$\mathbf{X}_i, \mathbf{X}^{(i)}$	The $i$ -th matrix in a set of matrices
$\mathbf{X}^T$	The transpose of matrix $\mathbf{X}$
$A, B$	Random variables
$F_i$	The $i$ -th element of a set
$y_i$	The $i$ -th entry of vector $y$
$\odot$	The Hadamard product
$\mathbf{1}$	A matrix of ones
diag( $\mathbf{a}$ )	A square matrix with the elements of $\mathbf{a}$ on the main diagonal, 0s elsewhere
$\Sigma_{abc}$	Summation over indices $a, b, c$
$\mathbb{E}[\cdot]$	Expectation
Var[ $\cdot$ ], Cov[ $\cdot$ ]	Variance, covariance
$\mu, \sigma^2, \rho$	Mean, variance, correlation
$ C $	Cardinality of set $C$
$\ \cdot\ _1$	The $l_1$ norm
$\ \cdot\ _2$	The $l_2$ norm

$$\begin{aligned}
& \underset{\mathbf{w}}{\text{maximize}} && \mathbf{w}_1^T \mathbf{X}_1^T \mathbf{X}_2 \mathbf{w}_2 \\
& \text{s.t.} && \mathbf{w}_1^T \mathbf{X}_1^T \mathbf{X}_1 \mathbf{w}_1 = 1, \\
& && \mathbf{w}_2^T \mathbf{X}_2^T \mathbf{X}_2 \mathbf{w}_2 = 1
\end{aligned} \tag{3.1}$$

where  $N$  is the number of subjects and  $d_1 = d_2 = d$  is the feature dimension. Kernel CCA (kCCA) [193, 194] transforms features into a reproducing kernel Hilbert space (RKHS), and finds the alignment between the transformed features  $\mathbf{K}_1$  and  $\mathbf{K}_2$ . The similarity in the RKHS is  $k(\mathbf{X}_{i,:}, \mathbf{X}_{j,:}) = \phi(\mathbf{X}_{i,:})^T \phi(\mathbf{X}_{j,:})$ , where  $\phi : \mathbb{R}^d \mapsto \mathbb{R}^{d'}$  is the feature transformation. LatSim learns a linear kernel  $\mathbf{A} \in \mathbb{R}^{d \times d'}$ ; however, this still allows detection of nonlinear relationships.

The main idea behind CCA and kCCA is to maximize the similarity between two or more signals after some constrained transformation. This constrained transfor-

mation moves the data to a latent space, which may be of lower dimension. The limitation of CCA and kCCA is that they are unsupervised learning techniques that must account for every similarity between the signals, not just those relevant for a particular application, although recent work is tackling this problem [185].

### 3.2.2 Latent Similarity

In contrast to unsupervised learning, LatSim maximizes similarity of subjects relative to a response variable of interest, such as age, sex or intelligence. First, similarities are computed as the inner product of the low-dimensional projections of subject features, based on a learned kernel:

$$\begin{aligned} \text{sim}(a, b) &= \langle \phi(\mathbf{x}_a), \phi(\mathbf{x}_b) \rangle \\ &= \mathbf{x}_a \mathbf{A} \mathbf{A}^T \mathbf{x}_b^T, \end{aligned} \tag{3.2}$$

where  $\mathbf{A} \in \mathbb{R}^{d \times d'}$  is the kernel matrix and  $\mathbf{x}_a, \mathbf{x}_b \in \mathbb{R}^d$  are feature vectors for subjects  $a$  and  $b$ , respectively. These similarities are then adjusted by passing them through a softmax activation function while masking each subject's self-similarity. The entire model for a single predictive task and a single fMRI paradigm is as follows:

$$\begin{aligned} \mathbf{M} &= \text{diag}(\infty), \\ \mathbf{E} &= S_{Row}((\mathbf{1} - \mathbf{M}) \odot \mathbf{X} \mathbf{A} \mathbf{A}^T \mathbf{X}^T), \\ S(\mathbf{z})_i &= \frac{e^{z_i/\tau}}{\sum_{j=0}^N e^{z_j/\tau}}, \end{aligned} \tag{3.3}$$

where  $\mathbf{E} \in \mathbb{R}^{N \times N}$  is the final similarity matrix,  $\mathbf{M} \in \mathbb{R}^{N \times N}$  is a mask to remove self-loops in predictions,  $\infty \in \mathbb{R}^N$  is a vector of infinite-valued elements,  $\mathbf{1} \in \mathbb{R}^{N \times N}$  is a matrix of ones,  $\mathbf{X} \in \mathbb{R}^{N \times d}$  is the feature matrix,  $\mathbf{A} \in \mathbb{R}^{d \times d'}$  is the kernel taking

connectivity features to a lower latent dimension,  $N$  is the number of subjects,  $d$  is the number of features (FCs),  $S(\mathbf{z})_i$  is the softmax function with temperature  $\tau$ , and  $S_{Row}(\mathbf{Z})$  is a function applying softmax to each row of the input matrix. High or low temperature  $\tau$  determines whether the subject-subject similarity matrix  $\mathbf{E}$  is more dense or sparse, respectively. The final similarity matrix of training and test set subjects is multiplied by the training set response variable to yield the prediction:

$$\hat{\mathbf{y}} = \mathbf{E}\mathbf{y}_{train} \quad (3.4)$$

The model is trained, using gradient descent, by minimizing the following objective function. Here we assume for brevity the existence of two fMRI feature matrices  $\mathbf{X}_a$  and  $\mathbf{X}_b$ , and two predictive tasks, one regression (1) and one classification (2), for which we identify four kernel matrices  $\mathbf{A}_{1a}$ ,  $\mathbf{A}_{1b}$ ,  $\mathbf{A}_{2a}$  and  $\mathbf{A}_{2b}$ :

$$\begin{aligned} & \underset{\mathbf{A}_{1a}, \mathbf{A}_{1b}, \mathbf{A}_{2a}, \mathbf{A}_{2b}}{\text{minimize}} \\ & \frac{1}{N}(\mathbf{y}^{(1)} - \mathbf{E}^{(1a)}\mathbf{y}^{(1)})^2 + \\ & \frac{1}{N}(\mathbf{y}^{(1)} - \mathbf{E}^{(1b)}\mathbf{y}^{(1)})^2 + \\ & \gamma_1 \frac{1}{N} \sum_{n=1}^N \sum_{c=1}^C \mathbf{Y}_{:,c}^{(2)} \cdot \log(\mathbf{E}^{(2a)}\mathbf{Y}^{(2)})_{:,c} + \\ & \gamma_2 \frac{1}{N} \sum_{n=1}^N \sum_{c=1}^C \mathbf{Y}_{:,c}^{(2)} \cdot \log(\mathbf{E}^{(2b)}\mathbf{Y}^{(2)})_{:,c} + \\ & \lambda_1 \|\mathbf{A}_{1a}\|_1 + \lambda_2 \|\mathbf{A}_{1b}\|_1 + \\ & \lambda_3 \|\mathbf{A}_{2a}\|_1 + \lambda_4 \|\mathbf{A}_{2b}\|_1 + \\ & \alpha_1 \|\mathbf{A}_{1a} \odot \mathbf{A}_{2a}\|_1 + \\ & \alpha_2 \|\mathbf{A}_{1b} \odot \mathbf{A}_{2b}\|_1 + \\ & \beta_1 \|\mathbf{X}_a \mathbf{A}_{1a} - \mathbf{X}_b \mathbf{A}_{1b}\|_2 + \\ & \beta_2 \|\mathbf{X}_a \mathbf{A}_{2a} - \mathbf{X}_b \mathbf{A}_{2b}\|_2, \end{aligned} \quad (3.5)$$

where  $\mathbf{E}^{(1a)} \in \mathbb{R}^{N \times N}$ , for example, is the similarity matrix for task 1 and fMRI paradigm  $a$ ,  $\mathbf{y}^{(1)} \in \mathbb{R}^N$  (numeric) and  $\mathbf{Y}^{(2)} \in \mathbb{R}^{N \times C}$  (one-hot categorical) are the stacked response variables for tasks 1 and 2, respectively,  $N$  is the number of subjects,  $C$  is the number of classes in task 2,  $\gamma_i$  is a task importance weight,  $\lambda_i$  is a sparsity-inducing hyperparameter,  $\alpha_i$  is a hyperparameter promoting feature disentanglement, and  $\beta_i$  is a hyperparameter promoting alignment between fMRI paradigms. Note that our experiments on the PNC dataset in Section 3.3.2 used precomputed vectorized functional connectivity matrices as the input, e.g.,  $\mathbf{X}$  is a matrix where each row is the vectorized FC of one subject.

In the conventional image domain, *Zheng et al.* (2022) have proposed a similar metric learning approach using softmax aggregation for image classification [195]. However, their work makes use of a pre-trained backbone, is semi-supervised, and does not provide all of the possibilities for feature selection, disentanglement, and alignment as does LatSim (see Equation 3.5).

### 3.2.3 Greedy Selection Algorithm and Model Interpretability

A greedy selection algorithm was developed to compare with other interpretability methods [196]. The algorithm selects connections one at a time by ranking their ability to separate dissimilar subjects, i.e., their ability to minimize similarity between subjects that are “far apart” with regards to the current residual:

$$\begin{aligned}
\mathbf{r}^{(i)} &= \text{LatSim}(\mathbf{X}_{F_{i-1}}, \mathbf{y}) - \mathbf{y}, \\
D_{ab} &= (r_a^{(i)} - r_b^{(i)})^2, \\
\mathbf{D} &= \mathbf{D} - \frac{1}{N^2} \Sigma_{ab} D_{ab}, \\
F_i &= F_{i-1} \cup \left\{ \underset{j}{\operatorname{argmin}} \Sigma_{ab} (D_{ab} X_{aj} X_{bj}) \right\},
\end{aligned} \tag{3.6}$$

where  $\text{LatSim} : \mathbb{R}^{N \times |F_{i-1}|} \rightarrow \mathbb{R}^N$  is the predictive model,  $r_a^{(i)}$  is the residual at iteration  $i$  for subject  $a$ ,  $\mathbf{D} \in \mathbb{R}^{N \times N}$  is a centered matrix of differences between residuals,  $F_i = \{0, \dots, i\}$  is the set of selected connections at iteration  $i$ ,  $\mathbf{X} \in \mathbb{R}^{N \times d}$  is the vectorized FC matrix for all subjects, and  $\mathbf{y} \in \mathbb{R}^N$  is the response variable. A summary of the algorithm is presented in Figure 3.2. We describe feature selection results in Section 3.3.2.

The greedy algorithm can select the several dozen most relevant features given a single predictive task. To select discriminative features using the fully trained model, we find the correlation between subject similarities and residual distances, as in Equation 3.6 above, except the FCs are multiplied by the learned model weights:

$$F = \underset{j}{\operatorname{argsort}} \Sigma_{abd} (D_{ab} A_{dj}^2 X_{aj} X_{bj}), \tag{3.7}$$

where the residual is set to the response variable,  $\mathbf{D}$  is calculated as before,  $\mathbf{A} \in \mathbb{R}^{d \times d'}$  is the set of model weights, and  $F$  is the resulting set of ranked features.

Except for greedy feature selection, we optimized prediction of all three response variables (age, sex, and intelligence) at the same time in the same LatSim model. Greedy selection required optimizing a single task at once, as the best feature for age prediction may not be the best feature for sex or intelligence prediction. LatSim was trained using PyTorch on an NVIDIA Titan Xp with CUDA support.

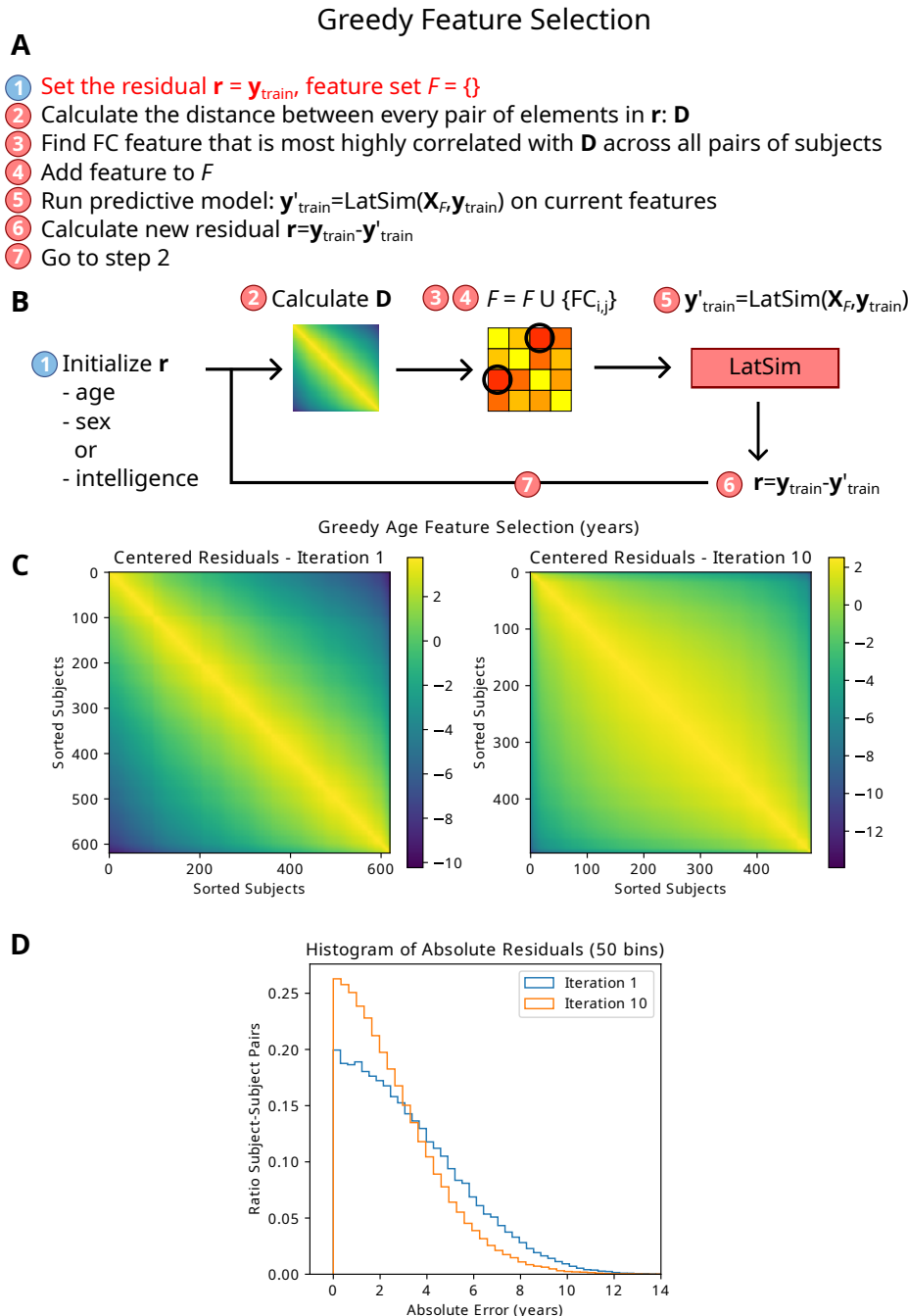


Figure 3.2: The greedy feature selection algorithm. **A.** A summary of the algorithm. **B.** A flowchart representation. **C.** Visualization of the residual distance matrices used to choose an FC feature at each iteration, at iterations 1 and 10. **D.** Histogram of absolute residual distance matrix values at iterations 1 and 10. Since LatSim works on subject pairs, our objective is to fit distances between residuals.

### 3.2.4 Spurious Correlation

We hypothesize that overfitting occurs due to feature noise or confounds, such as scanner motion, whose effects are more severe for smaller size cohorts. These confounds may create spurious correlations in a subset of the cohort.

We define a spuriously correlated feature  $X$  to be one that appears to be highly correlated with response variable  $Y$  for only a subset of subjects:

$$|\rho_S| \begin{cases} > 0 & s \in S \\ \approx 0 & s \in C \setminus S \end{cases} \quad (3.8)$$

where  $\rho_S$  is the value of the spurious correlation,  $C$  is the study cohort, and  $S \subseteq C$  is a subset of the cohort such that  $C \setminus S$  is maximized.

Note that spurious correlation may actually be true correlation identifying subgroups, but we hypothesize that a spurious correlation is more likely to be false as  $|S|$  decreases. We conduct simulation experiments in Section 3.3.1 that suggest LatSim is more robust against spurious correlation than traditional feature-based models. When  $|S|$  is close to  $|C|$ , and the effect is systematic, we cannot tell whether the correlation is true or false.

## 3.3 Results

We first demonstrate the superior performance of LatSim in a simulation study, then apply it to brain development fMRI data consisting of children and adolescents. We use both full-model and greedy feature selection to identify important functional connections for age, sex, and intelligence prediction.

### 3.3.1 Simulation Experiment

We performed a simulation experiment to test LatSim in the presence of a ground truth dataset. A set of  $N_{train} = 40$ ,  $N_{val} = 120$ , and  $N_{test} = 120$  subjects with 10,000 normally-distributed features  $x_{ni}$  was generated, where  $n$  and  $i$  refer to subject and feature, respectively. Each subject was also associated with a response variable  $y_n$ .

The data generation process for each subject was as follows:

$$y_n \sim \mathcal{N}(0, 1), \quad z_{ni} \sim \mathcal{N}(0, 4)$$

$$x_{ni} = \begin{cases} z_{ni} + y_n r, & \text{if } i \leq 1000 \\ z_{ni} + y_n r_S, & \text{if } 1000 < i \leq 2000 \text{ and } n \text{ even} \\ z_{ni}, & \text{otherwise} \end{cases} \quad (3.9)$$

where  $r$  and  $r_S$  are correlation-generating parameters for non-spurious and spurious correlations, respectively. In other words, the first 1,000 features were correlated with the response variable at level  $\rho$ , the next 1,000 features of half of the subjects were correlated at level  $\rho_S$  (and had 0 correlation for the other half of subjects), and the remaining 8,000 features were left uncorrelated. We varied  $r$  from 0.2 to 1 while keeping  $r_S = 1$ . It can be seen that final feature to response variable correlation is  $\rho = r/\sqrt{r^2 + 4}$  for correlated features for all subjects, and  $\rho_S \approx r_S/\sqrt{r_S^2 + 4}$  for spuriously correlated features for half of subjects.

The simulation showed that LatSim performs better than both a GCN [197] and Ridge Regression model in the presence of the spurious correlation  $\rho_S$  (see Figure 3.3). Additionally, LatSim was the only model identifying the three types of features: correlated, spuriously correlated, and uncorrelated. All results are on the test split. We believe insensitivity to spurious correlation is one of the reasons that LatSim performs well in the low-sample, high-dimensionality regime (see Section 3.4.3). A multi-

layer perceptron (MLP) with L1-regularization performed as well as Ridge Regression (not shown). The GCN model was not interpretable via either weight magnitude or gradient-based saliency. The MLP model identified only sparse features and selected features in the non-informative range. In contrast, LatSim was able to consistently identify the full range of informative features.

Notably, the weights are smaller for correlated features than for non-correlated features. This is an artifact of taking the absolute value of weights in order to average them across latent dimensions. Conversely, the spuriously-correlated weights are, on average, smaller than the constantly-correlated weights. To explain, suppose there are 2 sets of features,  $A$  and  $B$ , which are correlated and non-correlated, respectively. The similarity between two subjects will be:

$$\begin{aligned}
 & \mathbb{E}[(w_A A_1 + w_B B_1)(w_A A_2 + w_B B_2)] \\
 &= w_A^2 \mathbb{E}[A_1 A_2] + w_B^2 \mathbb{E}[B_1 B_2] \\
 &\quad + w_A w_B \mathbb{E}[A_1 B_2] + w_A w_B \mathbb{E}[A_2 B_1] \\
 &= w_A^2 \mathbb{E}[A_1 A_2] > 0,
 \end{aligned} \tag{3.10}$$

hence it doesn't matter what magnitude the weights  $B$  have, because the expectation of the non- $A_1 A_2$  terms is zero due to independence and the standard normal distribution of features. Conversely, if there is a subset of features  $A$  that are spuriously-correlated, it is beneficial to reduce the spurious weights compared to the non-spurious ones.

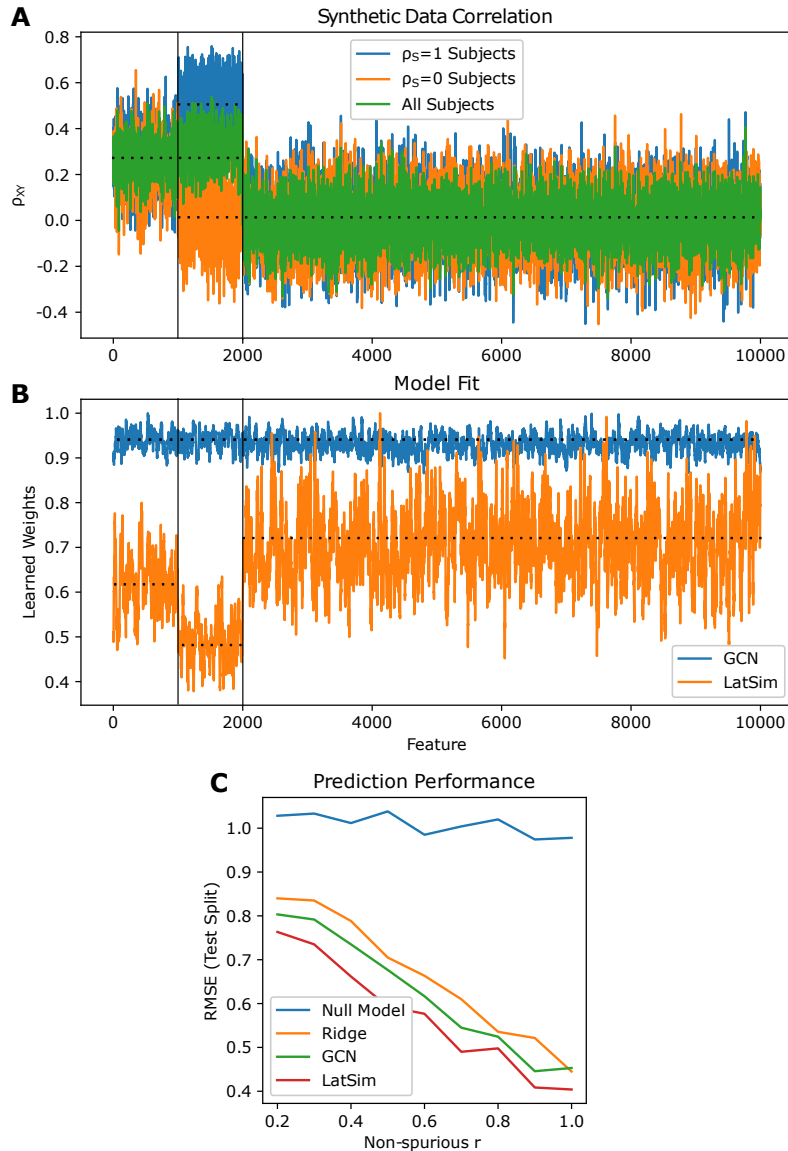


Figure 3.3: Results of simulations on synthetic data with spurious correlation. **A.** Data generated with non-spurious  $\rho = 1/(2\sqrt{4.25}) \approx 0.25$ , present in all subjects, and spurious  $\rho_s \approx 1/\sqrt{5} \approx 0.5$ , present in half of subjects. Correlation of response variable with feature for the training set is shown. Only the first two thousand features have any information relevant for prediction. **B.** Absolute value of learned model weights for the GCN and LatSim models, averaged over the first hidden layer (GCN) or latent dimension (LatSim). Weights are smoothed by a convolution kernel of size 20 to aid visualization. **C.** Average predictive performance (RMSE between ground truth  $y_i$  and predicted  $\hat{y}_i$ ) over 6 independent train/validation/test splits, evaluated on the test split.

	Number of Subjects
Males	286
Females	334
Total	620

	Min	Mean	Max
Age (months)	103	180±39	271
Age (years)	8.6	15±3.3	22.6
WRAT score	70	102±15.7	145

Table 3.2: Demographic information for the subset of the PNC dataset used in our experiments. WRAT score has been adjusted from its raw value by regressing out the effects of age.

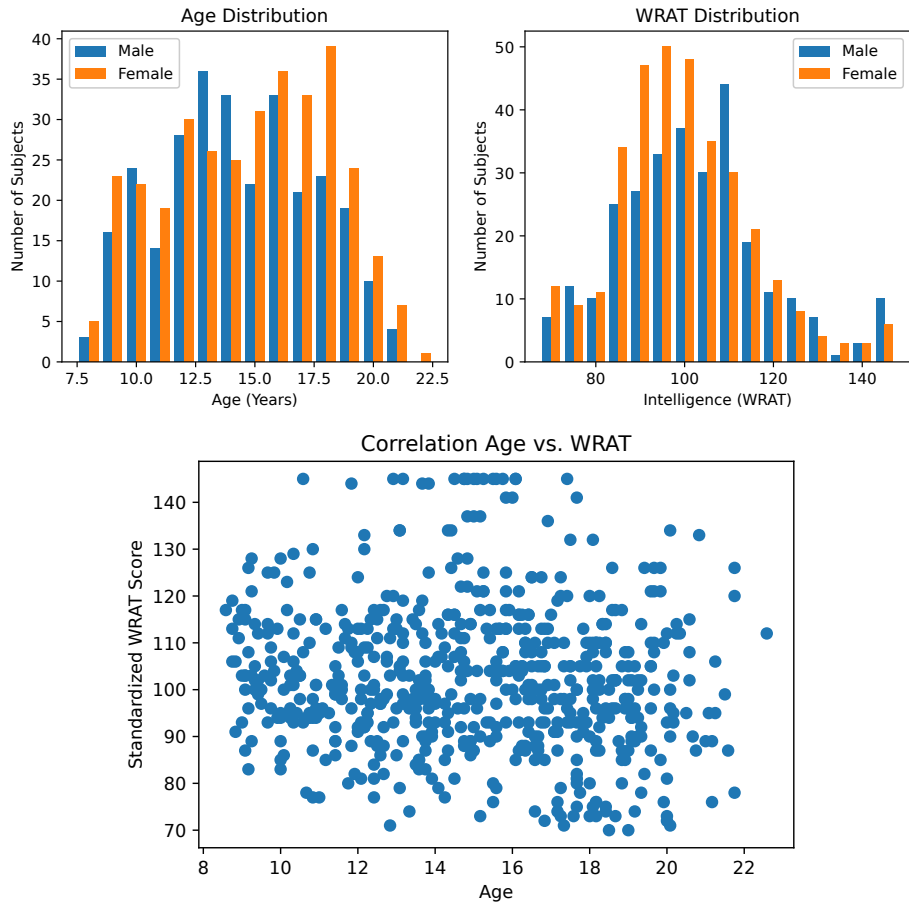


Figure 3.4: Demographics of the 620-subject subset of the PNC study used in our experiments. WRAT score has been adjusted from its raw value by regressing out the effects of age.

### 3.3.2 Brain Development Study

#### Dataset

We trained and validated our model on the publicly available PNC dataset. The PNC dataset contains multi-paradigm fMRI data, neurocognitive assessments, and psychiatric evaluations for 1,445 healthy adolescents ages 8-23. We chose 620 subjects from the cohort who had both working memory paradigm (nback) and emotion identification paradigm (emoid) fMRI scans, along with results from the 1-hour Wide Range Achievement Test (WRAT) [105] to measure general intelligence.

fMRI was performed using a 3T Siemens TIM Trio whole-body scanner with a single-shot, interleaved multi-slice, gradient-echo, echo-planar imaging sequence. The resolution was set to be 3x3x3 mm with 46 slices. The imaging parameters were TR = 3000 ms, TE = 32 ms, and flip angle = 90 degrees. Gradient magnitude was 45 mT/m, having a maximum slew rate of 200 T/m/s. The duration of the nback scan was 11.6 minutes (231 TR), during which time subjects were asked to conduct the n-back memory task, which is related to working memory and lexical processing [198]. The duration of the emoid scan was 10.5 minutes (210 TR), during which time subjects viewed faces displaying different emotions and gave an indication of what emotion was displayed. The demographics of our study cohort are given in Table 3.2 and the distribution is visualized in Figure 3.4.

Data was pre-processed with SPM12 (<http://www.fil.ion.ucl.ac.uk/spm/software/spm12/>). This included using multiple regression for motion correction, as well as spatial normalization and smoothing by a 3mm Gaussian kernel [199]. Pre-processing was similar to [200]. The Power template [5] was used to parcellate BOLD signal among 264 regions of interest, from which a  $264 \times 264$  symmetric connectivity matrix was constructed using Pearson correlation. The unique  $d = 34,716$  entries in the upper right triangle, excluding the main diagonal, were vectorized and taken as the

FC features for each subject.

The goal of the experiment was to predict subject age, sex, and intelligence as measured by WRAT score. Prediction performance was measured by root mean squared error (RMSE) for age and intelligence prediction, and accuracy for sex prediction, respectively. LatSim was compared against simple linear models (Least Squares and Logistic Regression), a Graph Convolutional Network (GCN), a Multi-Layer Perceptron (MLP), and a Multimodal Graph Convolutional Network (M-GCN). M-GCN is a recent deep learning model for functional connectome analysis [201] based on the CNN [202] architecture (<https://github.com/Niharika-SD/M-GCN>).

The inputs to all models were nback, emoid, and the arithmetic sum of nback and emoid task based vectorized FC matrices, from which separate predictions were made and averaged as part of an ensemble. The sum of nback and emoid FC was used to increase ensemble size. Standardization (Z-score normalization) was performed on the vectorized FC matrices using statistics from the training dataset applied to training, validation, and test datasets. Z-score normalization was performed only for the LatSim model, since the other models sometimes did not converge for Z-score normalized data. All predictive and feature selection experiments were carried out using 10-fold cross validation (CV), with an 80% training, 10% validation, and 10% test split. Hyperparameters were selected using random grid search (see Table 3.3 for LatSim hyperparameters and Table 3.4 for those of other models). The search grid was initialized to be a 5-decade window around prior assumptions of optimal hyperparameters, with search points occurring at decade intervals for all models. A total of 100 grid points were evaluated with three repetitions. The only exceptions were dropout, which was sampled at 0.1 intervals, latent/hidden dimension, which was set heuristically, and number of training epochs, which was set to just past the maximum best validation epoch for each model individually. Hyperparameters were estimated for the largest training set size ( $N = 496$ ) and subsequently used for all

Predictive Tasks fMRI Paradigms	Age, Sex, Intelligence nback, emoid, nback+emoid
Classification Multiplier	$\gamma = 1000$
Sparsity Parameter	$\lambda = 10$
Disentanglement Parameter	$\alpha = 100$
Feature Alignment Parameter	$\beta = 0.1$
Original Dimension	$d = 34,716$
Latent Dimension	$d' = 2$
Temperature	$\tau = 1$
Feature Dropout Rate	0.5
Edge Matrix Dropout Rate	0.1
Number of Training Epochs	200
Optimizer	Adam
Learning Rate	1e-4
L2 Regularization Parameter	1e-4
Weight Initialization	$1e-4 \cdot \mathcal{N}(0, 1)$

Table 3.3: Hyperparameters for PNC experiments (LatSim).

training set sizes, with the belief that over-optimization would give a distorted view of models and reduce reproducibility.

## Prediction

LatSim achieved superior predictive performance on the PNC dataset in all three predictive tasks, especially at low sample sizes. The result of the entire experiment is given in Figure 3.5, and the low and high sample size results are given in Table 3.5.

At  $N=30$ , close to the previously reported threshold of  $N=36$  for modestly reproducible fMRI results, we see that LatSim is the only model not to overfit. It surpassed the other models by a significant margin in two of three predictive tasks. Interestingly, LatSim performed much better at small sample sizes than the simple linear models, which we attribute to use of  $\mathcal{O}(n^2)$  inter-subject connections rather than the  $n$  subjects themselves. LatSim remains the best performing model until about  $N=100$ , at which point it is only slightly better than the other best predictive model, GCN. We note that the GCN model performs almost as well as LatSim, except at low sample sizes. We also note that with a categorical response variable such as sex, the

Predictive Tasks fMRI Paradigms	Age, Sex, Intelligence nback, emoid, nback+emoid
Model Implementation	<i>Least Squares Regression</i> PyTorch ( <a href="https://pytorch.org/">https://pytorch.org/</a> )
Model Implementation Regularization Parameter	<i>Logistic Regression</i> scikit-learn ( <a href="https://scikit-learn.org/stable/">https://scikit-learn.org/stable/</a> ) C=1
Model Optimizer Weight Initialization Learning Rate	<i>All Deep Models</i> Adam PyTorch Default 1e-4
Model Layers Number of Training Epochs L1 Regularization Parameter L2 Regularization Parameter	<i>MLP</i> 34,716 x 100 (hidden) 10,000 1e-2 1e-3
Model Implementation Number of Training Epochs L2 Regularization Parameter	<i>M-GCN</i> Github Repository 5,000 1e-4
Model Layers Number of Training Epochs Graph Type Neighbor Weight (Total) Node Self-loop Weight L2 Regularization Parameter	<i>GCN</i> 34,716 x 100 (hidden) 10,000 Complete 0.5 0.5 1e-4

Table 3.4: Hyperparameters for PNC experiments (comparison models).

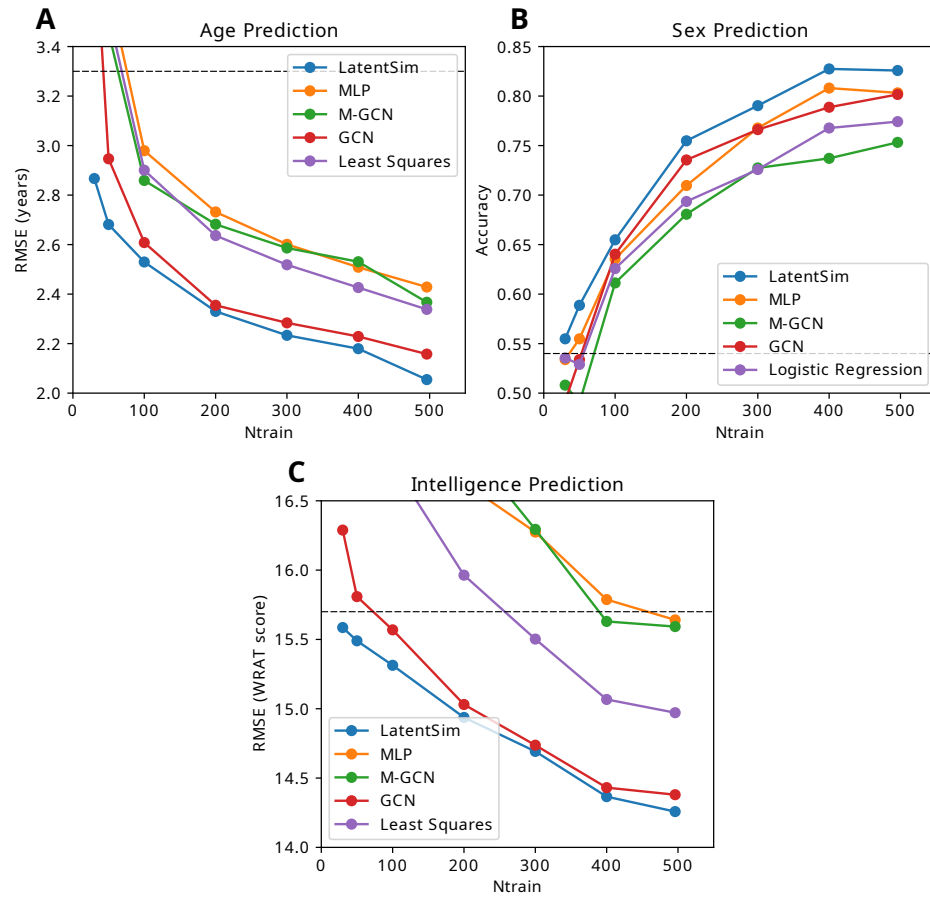


Figure 3.5: Results of age (A), sex (B), and intelligence (C) prediction experiments on our subset of the PNC dataset. Dashed black lines represent the null model. All models except LatSim performed worse than chance at the N=30 training set size for all tasks.

Model	Age (RMSE, years)		Sex (Accuracy)		Intelligence (RMSE, WRAT score)	
	N=30	N=496	N=30	N=496	N=30	N=496
Null	3.3		0.54		15.7	
M-GCN	4.47	2.37	0.51	0.75	23.27	15.59
MLP	4.52	2.43	0.53	0.8	21.17	15.64
GCN	3.89	2.16	0.49	0.8	16.29	14.38
Linear	4.36	2.34	0.54	0.77	19.8	14.97
LatSim	<b>2.86</b>	<b>2.05</b>	<b>0.55</b>	<b>0.82</b>	<b>15.59</b>	<b>14.26</b>
p-value	<b>2.2e-6</b>	<b>5e-3</b>	0.32	0.11	<b>0.02</b>	0.30

Table 3.5: Results of PNC experiments.

Model	LatSim	Lstsq	Logistic	GCN	MLP	M-GCN
Epochs	200	-	100	1e4	1e4	5e3
Training Time	<b>4.3s</b>	<b>&lt;1s</b>	63.4s	406s	364s	5912s

Table 3.6: Training time for all 10 folds of 10-fold cross validation.

performance of both LatSim and GCN is reduced. We believe the advantage of both LatSim and the GCN model lies in utilizing inter-subject similarities and differences. This is hindered by a lack of granularity in the response variable.

Based on the prediction results, LatSim can fit a dataset in orders of magnitude less time compared to other models (see Table 3.6). This makes it possible to perform large-scale bootstrapping, mixture of experts, and ensembling that is not possible with traditional ML models. It also allows for the use of greedy selection.

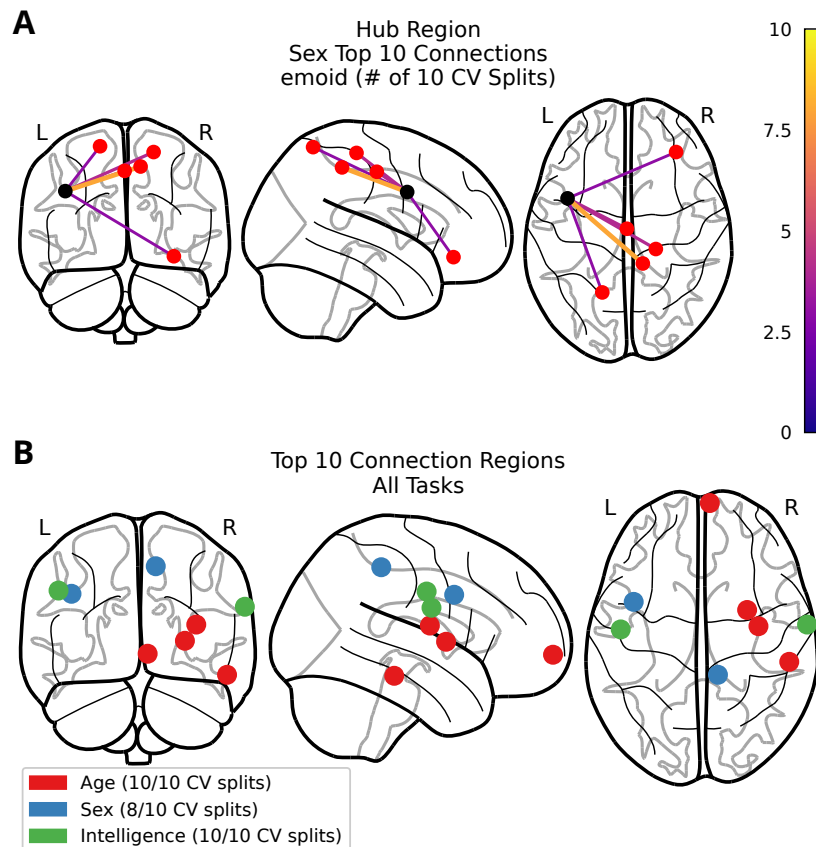


Figure 3.6: **A.** Identification of an interesting "hub" region found by emoid paradigm sex prediction that was included in 5 separate connections from among the top 10 connections across all CV splits. **B.** Visualization of regions found in the top 10 connections of more than 8 CV splits using the greedy selection algorithm.

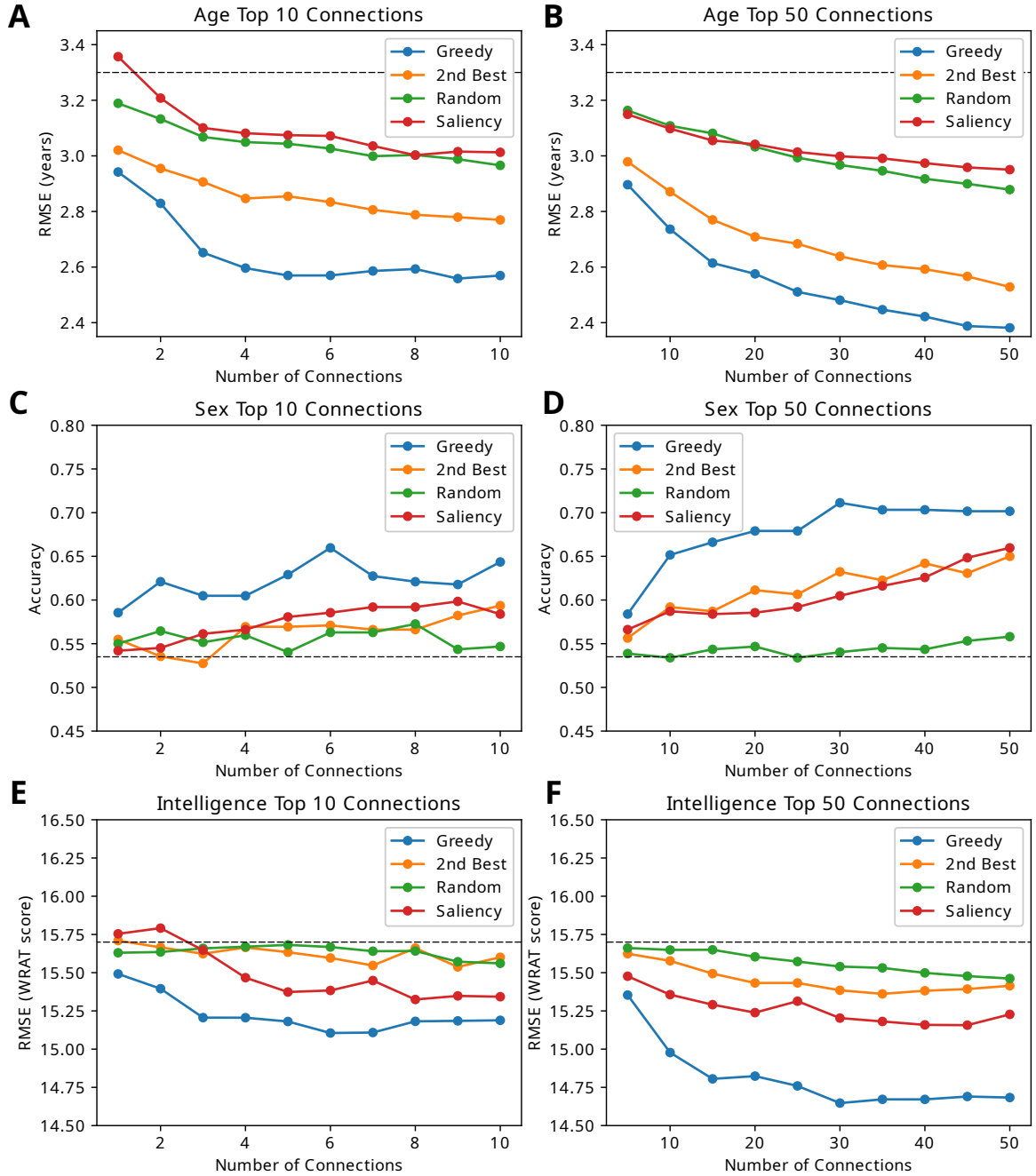


Figure 3.7: Comparison of four connection selection strategies. Dashed black lines represent the null model. Selection up to 10 connections (**A, C, E**) was done without dropout, whereas selection up to 50 connections (**B, D, F**) was done with 0.5 dropout.

	Region 1	MNI Coords	Network	Region 2	MNI Coords	Network	# CV Splits	Paradigm	Prediction Task
Insula_R	(36,-9,14)	SMT		Putamen_R	(29,1,4)	SUB	10/10	Both	Age
Temporal_Inf_R	(55,-31,-17)	UNK		Frontal_Med_Orb_R	(6,67,-4)	DMN	10/10	Both	Age
Frontal_Mid_L	(-34,55,4)	FRNT		Frontal_Mid_Orb_L	(-42,45,-2)	FRNT	9/10	nback	Age
Thalamus_R	(6,-24,0)	SUB		Left_Brainstem	(-5,-28,-4)	SUB	9/10	emoid	Age
Precentral_L	(-41,6,33)	FRNT		Temporal_Pole_Mid_R	(11,-39,50)	SAL	8/10		
Insula_R	(27,16,17)	UNK		Frontal_Inf_Orb_R	(49,35,-12)	DMN	3/10	emoid	Sex
Temporal_Pole_Mid_R	(46,16,-30)	DMN		Temporal_Pole_Mid_R	(52,7,-30)	DMN	3/10	nback	Sex
Frontal_Sup_Orb_R	(24,32,-18)	UNK		Fusiform_R	(27,-37,-13)	DMN	3/10	nback	Sex
Postcentral_L	(-49,-11,35)	SMT		Postcentral_R	(66,-8,25)	SMT	10/10	Both	Intelligence
Temporal_Mid_R	(52,-2,-16)	DMN		Precuneus_R	(10,-62,61)	DRSL	6/10	nback	Intelligence
Cerebellum_6_L	(-16,-65,-20)	CB		Postcentral_R	(66,-8,25)	SMT	5/10	emoid	Intelligence
Precentral_R	(44,-8,57)	SMT		Temporal_Inf_L	(-42,-60,-9)	DRSL	5/10	emoid	Intelligence

Table 3.7: Most important connections for discriminating age, sex, and intelligence among healthy adolescents. The # CV splits column shows the number of CV splits for which the connection appeared in the top 10 connections of the greedy selection algorithm. SMT=Sensory/Somatotomotor, CNG=Cingulo-opercular Task Control, AUD=Auditory, DMN=Default Mode, MEM=Memory Retrieval, VIS=Visual, FRNT=Fronto-parietal Task Control, SAL=Saliency, SUB=Subcortical, VTRSL=Ventral Attention, DRSL=Dorsal Attention, CB=Cerebellum, UNK=Uncertain

## Significant FCs in Prediction

The most important FCs for all prediction tasks are given in Table 3.7. All connections are given with Automated Anatomical Labeling (AAL) region names [94] and with Montreal Neurological Institute (MNI) region coordinates. For age prediction, the most important connections were Insula\_R to Putamen\_R and Temporal\_Inf\_R to Frontal\_Med\_Orb\_R, being present in the top 10 connections for both the nback and emoid paradigms. For sex prediction, the Precentral\_L to Temporal\_Pole\_Mid\_R FC was found in the top 10 connections for the emoid paradigm. For intelligence prediction, the Postcentral\_L to Postcentral\_R FC was found in the top 10 connections for both the nback and emoid paradigms. In addition, for sex prediction, we identified the Left Inferior Frontal Gyrus (Precentral\_L) as a region making multiple top 10 connections, as shown in Figure 3.6.

Using only the first few connections gives half of the predictive power of using the full set of  $d = 34,716$  connections. In particular, Figure 3.7 shows that the first 3 connections, if properly chosen, can contain more information than the next 50 connections, chosen in the same manner. Specifically, 10 FCs can explain 21% of variance for age, 50 FCs can explain 27%, whereas with the full set of FCs the GCN model can explain 35% and LatSim can explain 38%. The selected connections were chosen using the greedy feature selection algorithm. Figure 3.7 shows that the FCs chosen by greedy selection are superior to those chosen by gradient-based saliency, as well as to random FCs. Additionally, we compared the FCs chosen by greedy selection to the next-best FCs that would be chosen by it. We believe this helps validate the significance of our identified connections, since, for small numbers of connections, we could not find a minimal combination of FCs that performed as well as that found by greedy selection.

Selecting connections with the fully trained LatSim model corroborated the trend found by greedy selection. As seen in Figure 3.8, we identified a very few "core"

connections that were disproportionately important to the prediction task. The rest of the connections were interchangeable in terms of discriminative ability. Note, for instance, the rapid increase in accuracy for the 3 best FCs and the subsequent plateau in Figure 3.7. Likewise, almost all of the connections found in the top 50 connections by greedy selection were also found in the top 50 connections of the full model.

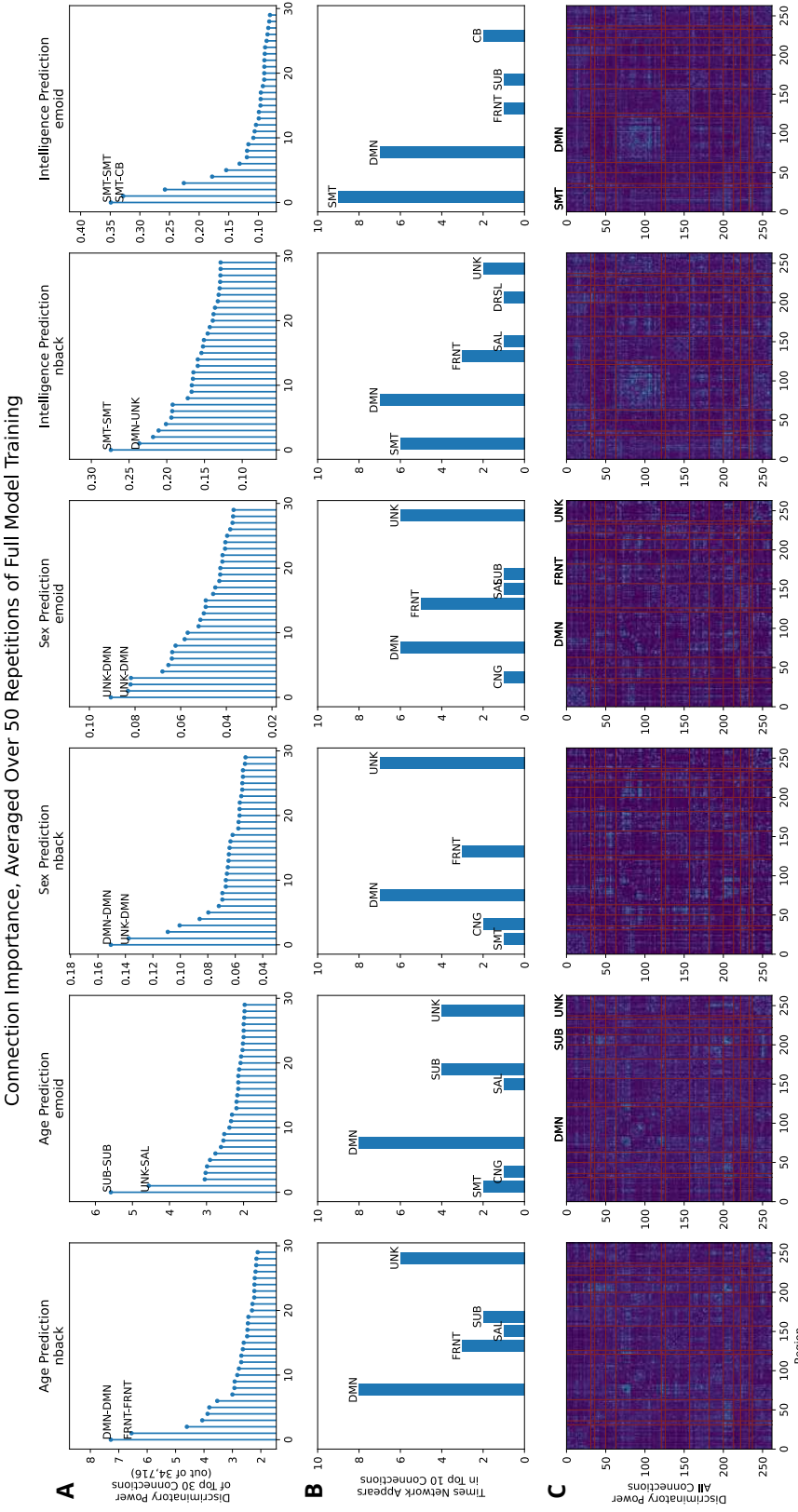


Figure 3.8: Important connections identified by running the full model with the entire  $d = 34,716$  set of connections as inputs. As with greedy selection, we show that the first several connections are far more important than the remaining ones (**A**). Notably, the DMN is highly represented in the top 10 connections for all predictive tasks and modalities (**B**). The DMN as a whole seems to be important for intelligence prediction (**C**). Importance was averaged over 50 repetitions of an 80-10-10 train/validation/test split. Discriminative power was calculated as in Equation 3.7. Correlation was greater than zero for all connections. See Table 3.7 for definitions of abbreviations.

### 3.3.3 Integration of Genomics and Functional Connectivity

Recent work has indicated better predictive performance from the integration of genomic, transcriptomic, or other omic data with imaging data compared with just imaging data by itself [70, 71, 81]. The Philadelphia Neurodevelopmental Cohort (PNC) dataset used in this study contains SNP data for more than 9,000 subjects as well as neuroimaging data for slightly more than 1,500 [59, 60]. SNPs were identified using one of 6 genotyping platforms, and a total of 1,901,972 SNPs were described in the entire cohort of 9,000 subjects. In this study, we tested whether SNP information combined with imaging data in the PNC dataset could yield superior prediction of WRAT score compared to imaging data alone.

Although many individual SNPs were identified, most could be described as rare alleles, or those with mean allele frequency less than 1% of the population [203]. To reduce the dimensionality of our dataset and enhance the predictive power of models integrating SNPs and FC, we excluded those SNPs whose minor allele was present in fewer than 50 subjects in the dataset resulting in a set of 35,621 SNPs used for further analysis. Integration of SNPs and FC was carried out via the LatSim model, with one half of the similarity kernel taking SNP input and the other half of the similarity kernel taking the upper right triangle of a subject's FC matrix (34,716 unique entries). These kernels reduced the dimensionality of these input features to two, and these latent features were combined in the typical way for LatSim using the cosine similarity and softmax function. The target feature used for this analysis was WRAT score, since age could not be predicted by SNPs, while sex could be predicted perfectly.

Figure 3.9 displays the results of using SNPs alone, SNPs integrated with FC, or FC alone to predict WRAT score in the PNC dataset. We see that SNPs or SNPs combined with FC have similar ability to predict WRAT score at a level better than chance, accounting for around 10% of variance in the data. FC derived from working

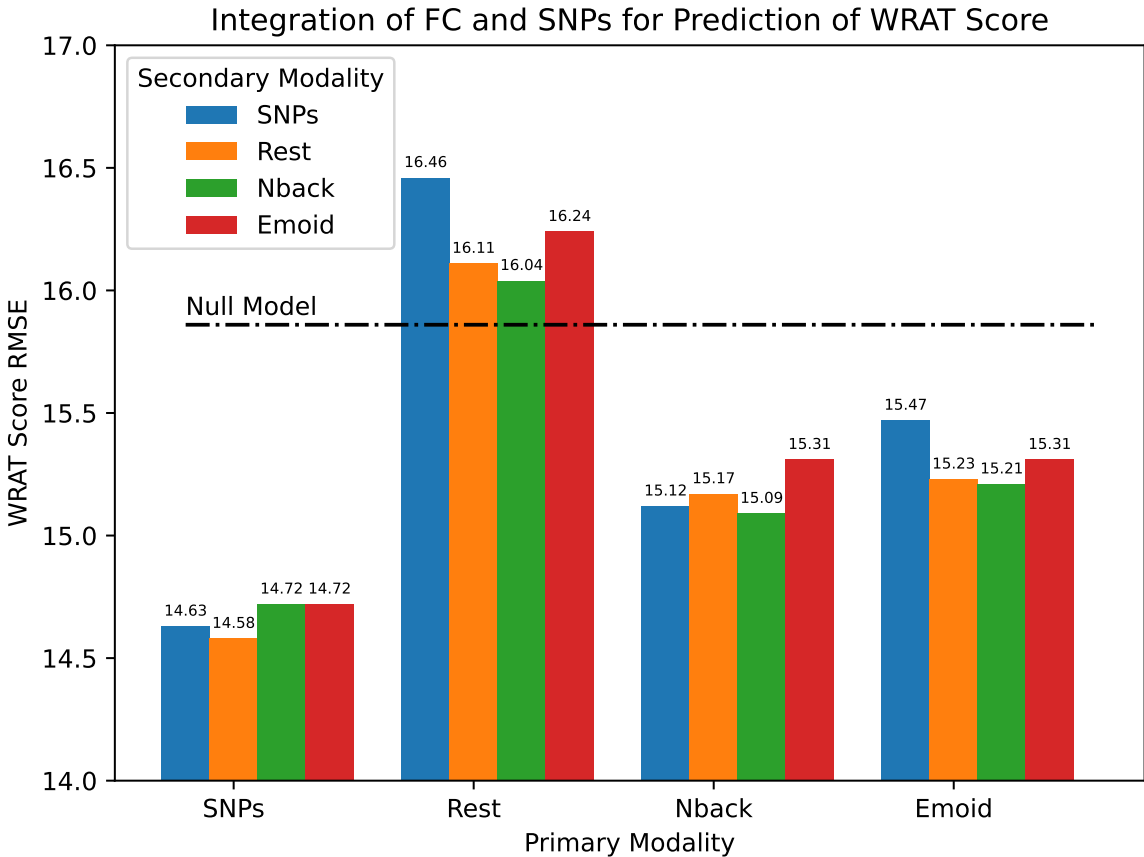


Figure 3.9: Prediction of WRAT score using integration of SNPs with resting or task fMRI FC. One part of the LatSim similarity kernel is used for SNP data while the other kernel is input FC data. Integration of SNPs with fMRI or SNPs by themselves provide for superior predictive power compared to fMRI alone. Resting state fMRI is unable to predict WRAT score better than chance, as represented by the null model line. Both working memory and emotion identification fMRI do a better job of predicting WRAT score than chance.

memory and emotion identification fMRI task could predict WRAT score almost as well as SNPs or SNPs integrated with FC, while resting state fMRI task was found to be unsuited for predicting WRAT score.

To identify the most important SNPs for WRAT prediction, we applied a LASSO L1 penalty to the weights of the kernel of the LatSim model. This resulted in a sparse set of SNPs that provided most of the predictive ability of using the full set of 35,621 SNPs. Since age and sex have been regressed out of raw WRAT score in the PNC dataset, while race has not, we then tested whether the distribution of SNPs was biased among the two main ethnic groups in the PNC dataset, African

Ancestry (AA) and European Ancestry (EA). We performed this analysis knowing that WRAT score distribution was different among the two subgroups, as seen in Figure 4.16. Indeed, we found that among the twenty mostly highly weighted SNPs in the predictive model, most were highly weighted toward one or the other ethnicity. Figure 3.10 shows the distribution of dominant allele among AA and EA groups as well as the difference between distributions for each SNP, compared with the difference in distribution among groups of the twenty most highly weighted SNPs for WRAT prediction. As discussed in Chapter 4, this hints that predictive tasks using both SNPs and FC are highly influenced by demographic confounds. In fact, as discussed in Section 4.5, removing demographic information from FC or SNP data makes most target features uncorrelated with said FC or SNP data.

Finally, Table 3.8 displays the details of the twenty most highly weighted SNPs for WRAT score prediction. Although most SNPs are highly biased toward one or the other ethnic group, we do find several SNPs that are associated with genes involved in neurodevelopment or associated with neurodevelopmental disorders. However, all of the twenty SNPs except one are found in intronic or non-coding DNA sequences, and although such SNPs can influence the expression of associated genes [204], they do not alter the sequence of the protein product itself.

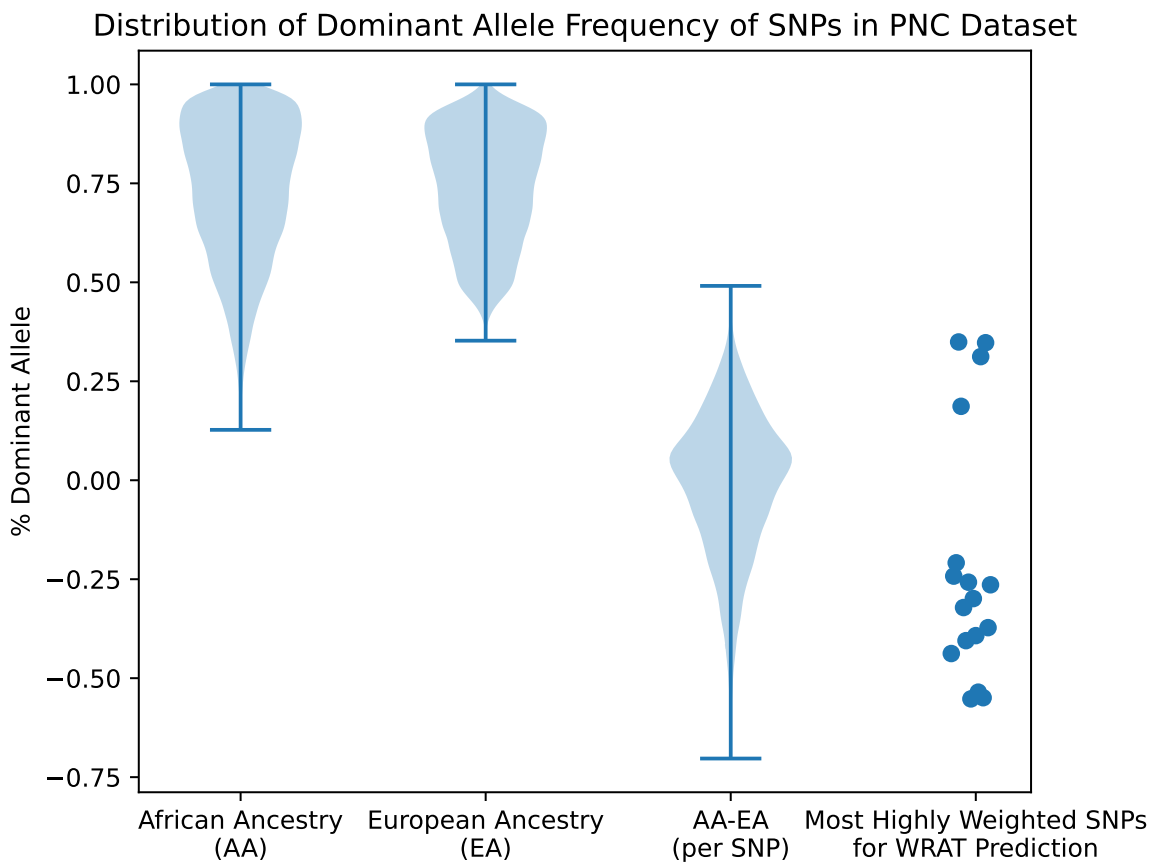


Figure 3.10: Plot of the distribution of dominant allele frequency among the two main ethnic groups in the PNC dataset, as well as difference between dominant allele frequency between the two groups and the 20 most highly weighted SNPs for WRAT prediction. WRAT-predicting SNPs are highly skewed toward those associated with one or the other ethnic group.

SNP	Weight	AA %	EA %	Allele	Location	Type	Gene	Role
rs919927	1.513	0.696	0.565	A>G	2:79862693	intron	CTNNNA2	Actin Binding in Brain
rs7854368	1.053	0.325	0.7628	A>G,T	9:112045361	intron	SUSD1	Calcium Binding Integral Membrane
rs7603462	1.015	0.634	0.877	A>C,G,T	2:99231427	non-coding		
rs2476773	0.899	0.507	0.716	C>A,G,T	13:107480826	intron	NALF1	Stretch activated calcium channel
rs7816586	0.866	0.891	0.541	A>C,G	8:27511817	intron	EPHX2	Epoxide hydrolase
rs898647	0.725	0.523	0.609	A>C,G,T	8:21162311	non-coding		
rs1956533	0.705	0.570	0.509	T>A,C	14:68444837	intron	RAD51B	DNA Repair by homologous replication
rs12457893	0.703	0.740	0.554	A>C,T	18:63258928	intron	BCL2	Cell death, blocks apoptosis
rs4692540	0.636	0.513	0.835	G>A,C,T	4:26529176	non-coding		
rs1036542	0.630	0.328	0.733	T>C,G	2:196993405	intron	ANKRD44	Recognition of phosphoproteins, Neurodevelopmental disorder-associated
rs2135354	0.531	0.384	0.642	G>A,C,T	4:113080731	intron	ANK2	Membrane-cytoskeleton linkage
rs9202449	0.529	0.323	0.875	A>C,G,T	2:200447606	intron	SPATS2L	RNA binding
rs7630982	0.501	0.590	0.889	G>A	3:184426858	nc-transcript	LINC02054	Glioma susceptibility
rs2855711	0.490	0.484	0.877	A>G,T	12:11877372	intron	ETV6	Vascular transcription factor
rs2252268	0.455	0.242	0.777	A>C,G,T	20:61411413	intron	CDH4	Cadherin cell-cell adhesion glycoprotein
rs223498	0.448	0.809	0.497	A>C,G	4:102730805	intron	MANBA	Lysosome enzyme
rs9285480	0.419	0.406	0.955	C>A,T	6:135298858	intron	AHI1	Cerebellar and cortical development
rs9518729	0.415	0.714	0.367	C>T	13:102451265	non-coding		
rs2211479	0.355	0.338	0.711	T>C,G	1:164997210	intron	KCNQ3	Neuronal potassium channel
rs7824311	0.345	0.457	0.721	G>A	8:132338873	intron		

Table 3.8: Description of the twenty most highly weighted SNPs for WRAT score prediction in the PNC dataset. Note that almost all highly weighted SNPs are non-coding: they are either intron variants or outside of genes. Some SNPs are associated with brain function, development, or neurodevelopmental disorders. AA=African Ancestry, EA=European Ancestry

## 3.4 Discussion

### 3.4.1 Significant Functional Networks

The top connections identified by this study contain regions that fall into the default mode (DMN), subcortical (SUB), fronto-parietal task control (FRNT), and sensory/somatotmotor (SMT) brain functional networks (FNs). Abbreviations are given as a footnote to Table 3.7. Regions that belong to the same FN (within-module) tend to be more synchronized than regions from different FNs (between-module) [205]. In Figure 3.8C, blocks on the main diagonal of the FC matrices represent connections within-module, while blocks off the main diagonal represent connections between-module. Recently, *Jiang et al.* (2022) found that, in an older population, connections between the DMN, SMT, and SUB networks were highly predictive for age [206]. They also found that a DMN-SUB connection was correlated with high cognitive performance.

The DMN was overrepresented in the top 10 connections for all predictive tasks; 36% of regions identified were part of the DMN, whereas DMN regions constitute 22% of the Power atlas. Robust developmental changes have been identified in the DMN, and DMN connectivity has been positively correlated with high cognitive performance [207]. *Fan et al.* (2021) found that DMN connectivity increases from childhood until young adulthood [208]. *Pan et al.* (2021) identified FCs which included DMN regions to be more important in predicting intelligence than FCs which didn't [209].

The SMT network was overrepresented in top 10 connection regions for intelligence prediction. In that task, 43% of top 10 connection regions belonged to the SMT network, whereas SMT regions constitute 13% of the Power atlas. It is known that dysfunction in the SMT network is correlated with depression [210]. However, FC represents synchronization between brain regions, and the cause of altered FC may not lie in the region itself. Table 3.7 shows that the top SMT connections involve the

CB network, leading to the idea that complex motor control is related to intelligence.

Many of the most important connections we identified for each predictive task are not recognized as part of an FN, and are classified as unknown-network (UNK). 24% of regions identified in top 10 connections are labeled UNK, whereas UNK regions constitute 10% of ROIs in the Power atlas. These connections include cerebellar regions; some cerebellar regions are not included in the CB network because they contribute to functions other than motor function [211], including social thinking and emotion [211]. *Zhang et al.* (2022) recently found disrupted effective connectivity in UNK cerebellar regions in individuals with schizophrenia, relative to controls [212].

### 3.4.2 Significant FCs

Greedy selection identified 4 FCs present in more than 8 out of 10 CV splits for one of the predictive tasks:

- **Insula\_R to Putamen\_R (Age).** The Insula\_R has many functions in humans dealing with low-level sensation, emotion, and high-level cognition [213]. *Mazzola et al.* (2016) hypothesized that the Insula\_R participates in the social brain and found increased activation when participants watched scenes of joyful or angry actors [214]. Increased Putamen\_R volume has been linked to autism spectrum disorder [215], and reduced amygdala-Putamen\_R FC has been linked to ADHD [216].
- **Temporal\_Inf\_R to Frontal\_Med\_Orb\_R (Age).** The Temporal\_Inf\_R region is associated with language processing [217]. Temporal\_Inf\_R FC was found to be decreased in adolescent schizophrenia patients [218]. The Frontal\_Med\_Orb\_R region is part of the prefrontal cortex and is associated with dysfunctional connectivity in major depressive disorder [219].
- **Precentral\_L to Temporal\_Pole\_Mid\_R (Gender).** The Precentral\_L re-

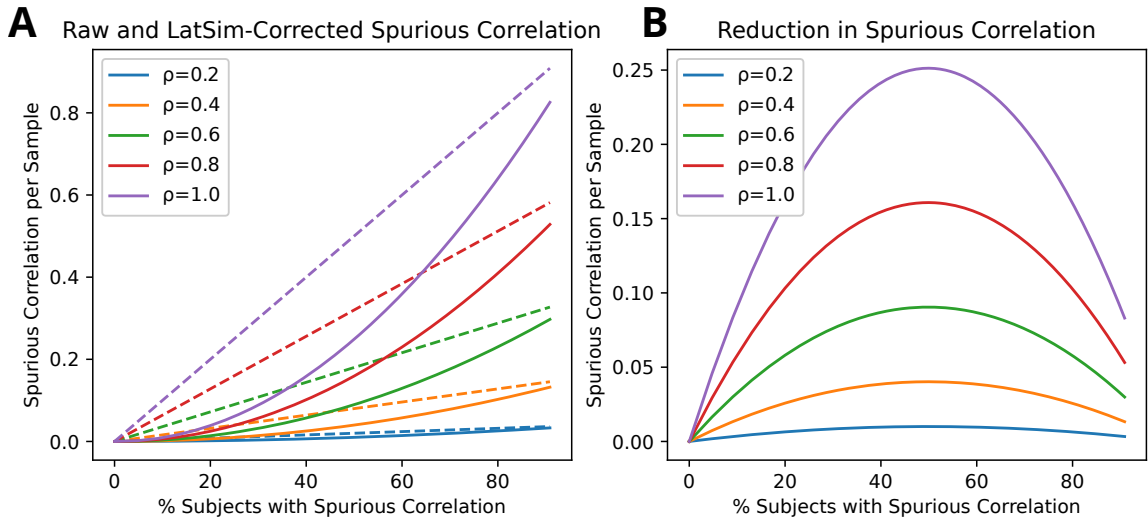


Figure 3.11: **A.** Spurious correlation per sample in a traditional ML model (dashed lines) versus LatSim (solid lines). **B.** The absolute reduction in spurious correlation as a function of frequency in the sample.

gion is associated with reading and language processing [220]. *Delvecchio et al.* (2021) found morphological differences in this region between sexes [221]. The Temporal\_Pole\_Mid\_R region is linked to social contracts, precautions, and strategies [222].

- **Postcentral\_L to Postcentral\_R (Intelligence).** This is a connection between regions symmetric about the body mid-line. The postcentral gyrus is involved in proprioception and contains the primary somatosensory cortex. Lesions in these regions may cause speech dysfunction [223, 224]. *Sander et al.* (2022) found inter-hemispheric connectivity to play a role in the ability to learn new languages [225].

Notably, AAL regions extend over a large area, and Power atlas ROIs do not correspond exactly to AAL regions.

### 3.4.3 Robustness to Spurious Correlations

In this section, we argue that LatSim is robust to spurious correlation because it identifies features based on  $\mathcal{O}(n^2)$  inter-subject connections, rather than the number of subjects in the cohort.

Assume feature  $X$  is spuriously correlated with response variable  $Y$  on a subset of the cohort  $S \subseteq C$ ,  $s = |S|$ ,  $n = |C|$ , and  $X, Y \sim \mathcal{N}(0, 1)$ . That is, for each subject  $u$ :

$$|\rho_S| \begin{cases} > 0 & u \in S \\ \approx 0 & u \in C \setminus S \end{cases} \quad (3.11)$$

LatSim uses weighted inner product similarity  $wX_1wX_2$  between the features of two subjects as input, where  $w$  is a learned weight. The correlation between  $wX_1wX_2$  and  $D = (Y_1 - Y_2)^2$  determines how well this feature pair predicts the response variable:

$$\begin{aligned} \rho_{XX,D} &= \frac{\sigma_{XX,D}^2}{\sqrt{\sigma_{XX}^2 \sigma_D^2}} \\ &= \frac{\text{Cov}[wX_1wX_2, (Y_1 - Y_2)^2]}{\sqrt{\text{Var}[wX_1wX_2] \text{Var}[(Y_1 - Y_2)^2]}} \\ &= \frac{\mathbb{E}[X_1X_2(Y_1 - Y_2)^2] - \mu_{XX}\mu_D}{\sqrt{\mathbb{E}[X_1^2X_2^2 - \mu_{XX}^2]\mathbb{E}[(Y_1 - Y_2)^4 - \mu_D^2]}} \\ &= \frac{\mathbb{E}[X_1X_2(Y_1 - Y_2)^2] - 0 \cdot 2}{\sqrt{\mathbb{E}[X_1^2X_2^2 - 0^2]\mathbb{E}[(Y_1 - Y_2)^4 - 2^2]}} \\ &= \frac{\mathbb{E}[X_1X_2Y_1^2 - 2X_1X_2Y_1Y_2 + X_1X_2Y_2^2]}{\sqrt{(1 \cdot 1)(12 - 4)}} \\ &= \frac{0 - 2\rho_{XY}^2 + 0}{\sqrt{8}} \\ &= \begin{cases} -\frac{\rho_S^2}{\sqrt{2}} & 1, 2 \in S \\ 0 & \text{otherwise} \end{cases} \end{aligned} \quad (3.12)$$

Since expectation is a linear operator, we can find the average value over the entire cohort:

$$\begin{aligned}\rho_{XX,D} &= -\frac{s(s-1)}{n(n-1)} \frac{\rho_S^2}{\sqrt{2}} \approx -\frac{s^2}{n^2} \frac{\rho_S^2}{\sqrt{2}} \\ &\approx k \frac{s^2}{n^2} \rho_S^2\end{aligned}\tag{3.13}$$

Conversely, in a traditional model, feature  $X$  is correlated with response variable  $Y$  as the size of the subset  $S$ :

$$\rho_{X,Y} = \frac{s}{n} \rho_S\tag{3.14}$$

A plot of the functions in Equations 3.13 and 3.14 is given in Figure 3.11. The maximum reduction in spurious correlation occurs at  $s/n = 0.5$  and is about 1/4 of the value of the spurious correlation. The relative reduction is linear and maximal when  $s = 0$ , i.e., there are no subjects with spurious correlation (not shown). As  $s/n$  increases, the reduction in spurious correlation is diminished. This suggests that large model capacity is not the only reason complicated models falter at low sample sizes. We see in our experiments, e.g., in Table 3.5, that the linear models perform worse than both LatSim and some other deep learning models.

Like LatSim, a k-layer GNN model also works on interactions between subjects, but as an adjunct to the prediction from the node self-loop. It also requires either additional degrees of freedom to estimate edge weights, or an arbitrary choice of a distance function and/or threshold. We believe the reason that a GCN model did so well in our experiments is that we made it incredibly simple: only 2 layers were used, and edge weights were uniform and equal in sum to the self-weights. It was found that expanding the GCN to 3 or 4 layers hurt performance. We believe the performance benefit comes from having a good prior and feature selection, not additional model

capacity. Due to the very weak relationships between features and response variables in our data, we believe the advantage of the GCN was in averaging. This strategy breaks down at low sample sizes, where spurious feature correlation still causes large errors to be present at the node self-loop.

### 3.5 Conclusion

This chapter proposes a novel model, LatSim, in the vein of metric learning, that is robust against overfitting at small sample sizes. It is interpretable, computationally efficient, multi-task and multi-view capable, and able to enforce feature disentanglement. First, we showed that LatSim is superior in the small sample size, high dimensionality regime, through both simulation and experiments on real datasets. Second, we identified specific connections within and between the sensory/somatomotor, default mode, fronto-parietal task control, and subcortical networks that are highly discriminative for age, sex, and intelligence in healthy adolescents. Third, we quantified the number of features required to attain a given prediction accuracy. Fourth, we showed that there are several core connections that are more discriminative for each predictive task than other connections. Finally, we found that connections identified by greedy selection were superior compared to those found by saliency methods. Our model may spur new research into algorithm development and, in turn, lead to new insights into the mechanisms underlying human cognition.

## Chapter 4

# Description of a Functional Connectivity Analysis Tool and Identification of Demographic Confounds

### 4.1 Introduction to ImageNomer

Existing software packages for analysis of fMRI, FC, and FC-like measures such as partial correlation connectivity are either mostly text-based (programmatic interface) or have incomplete feature sets for identifying correlations in phenotypes (see Figure 4.1). For example, numpy [226], PyTorch [227], scikit-learn [166], nilearn [228], and nipype [229] are all powerful and popular Python-based toolkits that can be used to conduct neuroimaging research. In fact, we use some of these packages as components in our ImageNomer software, but they all lack a graphical user interface that can speed up exploration of new datasets. Classic packages such as the Matlab-based BrainNet viewer [230] or GIFT toolbox [231], although they have a GUI frontend, do

	correlation analysis	GUI	no Matlab depend.	demographics	FC/PC/imaging	SNPs	custom groups	easy to use
numpy/PyTorch	+	-	+	+	-	-	+	-
sklearn/nilearn	+	-	+	+	+	-	+	-
GIFT	-	+	-	-	+	-	+	+
BrainNet viewer	-	+	-	-	+	-	-	+
COINSTAC	+	+	+	+	+	-	-	-
Infinitome	-	+	+	-	+	-	-	+
<b>ImageNomer</b>	+	+	+	+	+	+	+	+

Figure 4.1: Comparison of existing toolkits for analysis of fMRI-based FC data with our ImageNomer software. A more comprehensive list may be found at [https://en.wikipedia.org/wiki/List\\_of\\_functional\\_connectivity\\_software](https://en.wikipedia.org/wiki/List_of_functional_connectivity_software).

not allow for analysis of correlations between phenotypes as well as between phenotypes and imaging features/SNPs. Additionally, a Matlab-based toolchain ties one's product to a proprietary and non-free dependency. Even more modern tools like COINSTAC [232] fall short because of a complicated user interface, lack of support for extremely high dimensional features, and a focus on federated learning which most neuroscientists do not need in their research. In contrast, ImageNomer focuses on data exploration by allowing correlation analysis of imaging, demographic, and genomic features and the creation of demographic-based subgroups. An overview of the ImageNomer architecture is shown in Figure 4.2.

Two problems with creating good, easy-to-use tools for analysis of fMRI-derived FC data are the high dimensionality of imaging features and the small effect sizes being measured. For example, Bennet et al. found that many effects found as marginally significant by standard analysis techniques are simply due to noise [233, 234]. For many recent fMRI studies, high dimensionality of the data and small effect size is exacerbated by small cohort sizes [103], with the average reproducible cohort size for an fMRI result being 36 subjects [134]. Our ImageNomer software addresses these

points by treating visualized FC matrices (see Figure 4.3) and FC/phenotype correlation maps (see, e.g., Figure 4.8) as the primary outcome of the analysis, allowing quick visual inspection of what would take a long time through a programming interface. Cognizant of the high dimensionality of imaging features, we also perform Bonferroni-type multiple comparison correction in all FC-phenotype and SNP-phenotype correlation analysis. This does a lot to avoid the dead-salmon effect found by *Bennet et al.* (2010) [234].

To demonstrate the utility of our developed ImageNomer tool, we use its data visualization and correlation abilities to quickly and easily identify a race confound in FC data. Specifically, we find that the high correlation between FC and race and the unequal distribution of achievement scores among races makes it appear that FC can predict achievement score, when our work shows it is more likely due to a confound. Many studies have used FC features to predict scholastic achievement, as measured by, e.g., WRAT score [105], explaining 10% of the variance in a population [148] or achieving a small correlation with ground truth of  $\rho \approx 0.3$  [235]. We show, however, that the FC feature to WRAT score correlation is probably due to a confounding effect of race on FC. Indeed, previous studies have shown that AI models can sometimes trivially detect and be confounded by race [236], and recent work has suggested that race can confound FC-based prediction of behavior [237]. In this work, we use ImageNomer to identify a confound in FC, and find that this race confound is primarily responsible for any ability to predict WRAT score from FC. The utility of a tool like ImageNomer is validated by speed with which we find the race confound using a GUI toolkit, while numerous groups continue to search for achievement-based features, presumably using programmatic interfaces [148, 235].

In summary, correlation analysis can give a quick overview of the data, and subject-level or cohort-level views can be instrumental for quality control. This is the reason we have developed ImageNomer, a visualization and analysis tool for

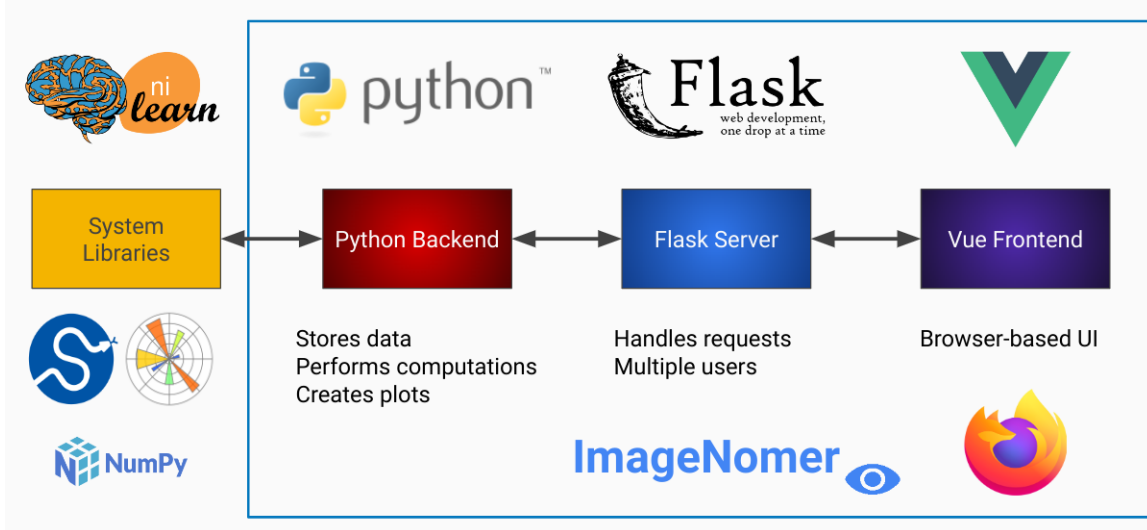


Figure 4.2: Overview of the ImageNomer architecture.

connectivity-based fMRI and omics studies. The tool enables rapid correlation analysis as well as the comparison of features from outside models in a convenient browser-based user interface. Additionally, we include the ability to analyze distribution of phenotypes. Indeed, we find that correlation analysis is sufficient to quickly and clearly identify the confounding effect of race on WRAT score found in our study. Our code, as well as a Docker image and a live on-line demo, has been released and are available via links on our GitHub page. The docker image and source code are available online at <https://github.com/TulaneMBB/ImageNomer>.

## 4.2 Methods

### 4.2.1 Architecture

ImageNomer is made up of three components (see Figure 4.2):

- a Python backend which integrates with available libraries such matplotlib, scikit-learn, and nilearn

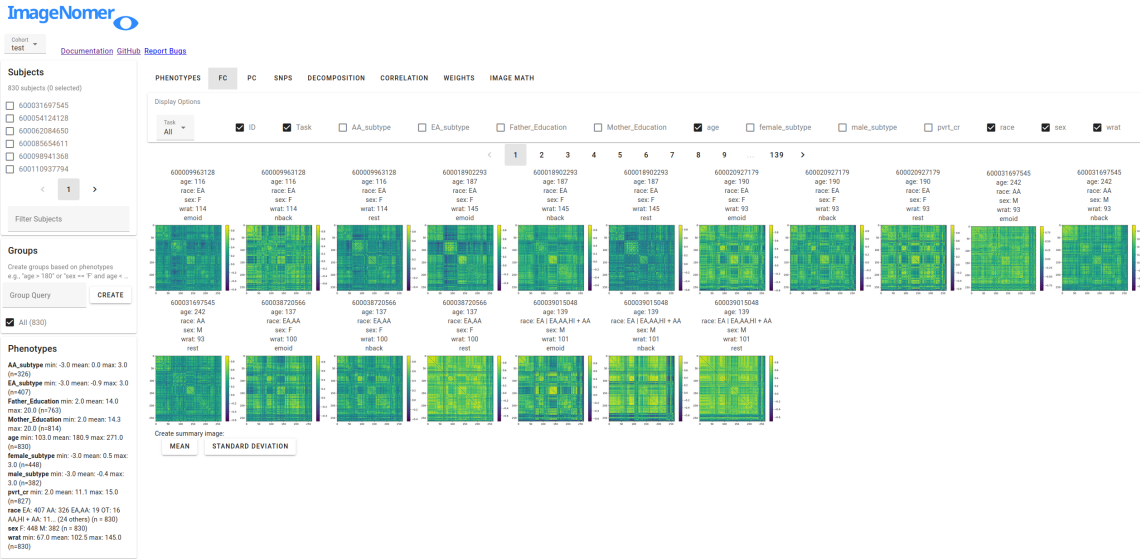


Figure 4.3: Main view of the ImageNomer program showing resting state FC for all subjects along with demographic data.

- a Flask server that handles requests from the browser-based UI to the backend
- a Vue frontend which provides an interactive user experience from within the browser

A web-based user interface allows quick navigation around a cohort as well as the creation of summary graphs and correlation analyses. The main FC view is shown in Figure 4.3. The data being explored is stored locally in the server component, while the Python backend allows integration with standard libraries such as nilearn, scipy, numpy, and matplotlib. The matplotlib backend is used to generate all graphs on the backend, which are sent to the frontend as images. The Vue frontend allows for modularity of UI components, provides a library of pre-built widgets via Vuetify, and enables easy-to-code interactivity.

#### 4.2.2 Software Features

ImageNomer has the following capabilities:

- Examine individual subject FC and partial correlation-based (PC) connectivity
- Display distributions of phenotypes
- Correlate phenotypes with phenotypes, FC/PC features with phenotypes, and SNPs with phenotypes
- Display p-value maps for correlations
- Perform math on images
- Display components for FC decompositions (such as PCA)
- Correlate decomposition components with phenotypes or SNPs
- Display weights from machine learning models
- Summarize and average weights from multiple models

Future work with fMRI will likely require summarizing connectivity patterns into discrete network contributions [238]. We are also working to expand ImageNomer’s capabilities for summary measures and dictionary learning.

#### 4.2.3 Live Web Demo, Docker Images, and Tutorial

We have created a live on-line demo (available at [https://aorliche.github.io/  
ImageNomer/live/](https://aorliche.github.io/ImageNomer/live/)) and a Docker image containing an example open-access dataset of Fibromyalgia patients. This dataset is available as accession number ds004144 from OpenNeuro [239, 240]. Instructions for using the Docker images, as well as a tutorial based around the Fibromyalgia dataset, can be found online. Documentation and tutorial are available at <https://imagenomer.readthedocs.io/en/latest/index.html>. The tutorial goes through step-by-step each of the major functions of ImageNomer, with instructions and screenshots of the expected output. Unfortunately,

NIH data access policy precludes us from making the PNC or BSNIP data available publicly. If you are an approved researcher, we would be happy to work with you regarding functions, e.g., SNPs, which are not found in the Fibromyalgia dataset.

The easiest way to use ImageNomer is by mapping a directory on your local machine containing a “demographics.pkl” file and an “fc” subdirectory into the Docker image when starting the container (download and use ImageNomer: <https://github.com/TulaneMBB/ImageNomer>). We provide a second preprocessed OpenNeuro dataset ds004775 [241] dealing with Vicarious Punishment in our GitHub along with a tutorial on how to map it to the Docker container, similar to what one would do for one’s own dataset. Our GitHub repository also contains a notebooks folder with Jupyter notebooks that shows step-by-step how the Fibromyalgia and Punishment data were preprocessed in manner suitable for ImageNomer, starting from a CSV/TSV file and BOLD timeseries.

Alternatively, ImageNomer can be used by cloning our GitHub project and installing the Python requirements via pip. However, the use of Docker images, via instructions found on our GitHub is the easiest method. Docker images have been built for the amd64 and arm64 architectures; check the documentation for how to use the right version for you. If one is interested in editing the code, it is split into the “backend” and “frontend” directories. The “backend” directory contains Python modules and does the heavy lifting with respect to data loading, image generation, and correlation analysis. The “frontend” directory contains a Vue javascript project that handles the browser-based interface and keeps track of most session state. Individual parts of the web-interface are built as Vue components.

#### 4.2.4 Case Study on Ethnicity Confound in FC and Its Impact on Achievement Score Prediction

As a demonstration of the power of ImageNomer’s GUI in quickly identifying trends, confounds, and correlations in data, we give a case study of using ImageNomer to identify an under-reported race confound present in FC. As discussed in the Introduction, many groups have tried to predict achievement score or similar metrics from FC. Using ImageNomer, we find that there is a large difference between achievement scores among races. This can potentially lead to a confounding effect if race can be predicted from FC. We also find a high correlation between race and certain FC regions, making us suspect that race-from-FC prediction is possible. We then verify the presence of this confound by performing regression on the whole cohort vs. within-ethnicity subsets. We learn that quick and dirty data exploration may save a lot of time trying to look for FC correlates of cognition that may or may not be there.

#### 4.2.5 PNC Dataset

We tested ImageNomer by using it to examine the large Philadelphia Neurodevelopmental Cohort (PNC) dataset [59, 60]. The PNC dataset contains fMRI scans, SNP information, cognitive batteries, questionnaires, and phenotype data from healthy adolescents between 8-23 years old. The dataset is enriched for European Ancestry (EA) and African Ancestry (AA) races. It contains fMRI scans for 1,445 healthy adolescents and SPN data for more than 9,267. We chose an 830-subject subset of the data which included subjects with SNP information as well as resting state (rest), working memory (nback), and emotion identification (emoid) scanner task fMRI scans. Scholastic achievement and problem-solving ability was measured by Wide Range Achievement Test (WRAT) score [105] with the effects of age regressed out. A total of three fMRI tasks were acquired: resting state, working memory,

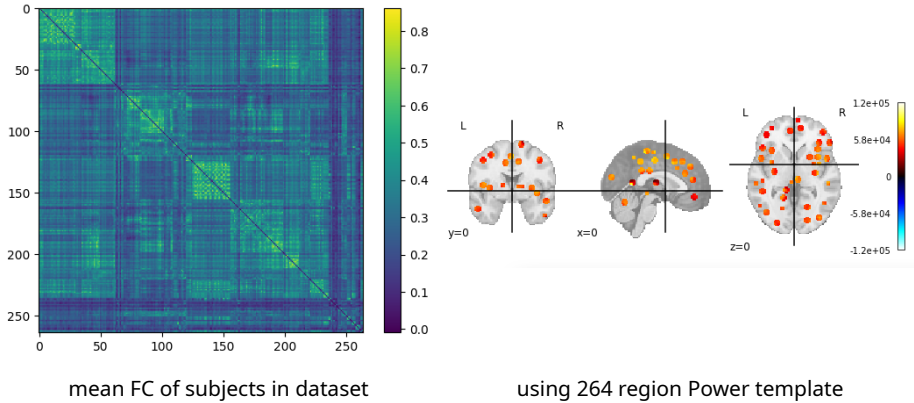


Figure 4.4: Mean FC in the PNC dataset along with the Power264 template[5] regions used to sample BOLD signal from brain regions.

and emotion identification. An example of parcellation along with mean FC in the PNC dataset is shown in Figure 4.4. The acquisition parameters for fMRI and FC preprocessing have been described elsewhere [148].

SNPs were collected using one of eight different platforms, with the largest set containing 1,185,051 SNPs [59]. We selected a subset of 10,433 SNPs that were found in at least 100 subjects in the cohort for our analysis. SNPs were categorized by haplotype as homozygous minor variant, heterozygous, and homozygous major variant. Missing values for subjects were set to zero for all haplotypes.

#### 4.2.6 BSNIP Dataset

Robustness of race prediction from FC was tested by using an independent dataset to validate models trained on PNC. The dataset used was the Bipolar and Schizophrenia Network for Intermediate Phenotypes (BSNIP) dataset of 933 patients, 1059 relatives, and 459 healthy controls [108]. fMRI scans were acquired over 6 different sites, and acquisition and preprocessing are described elsewhere [242]. For validation of race prediction we chose a subset of 387 African Americans (AA) and 778 Caucasians (CA), both patients and healthy controls, for whom we had fMRI scans.

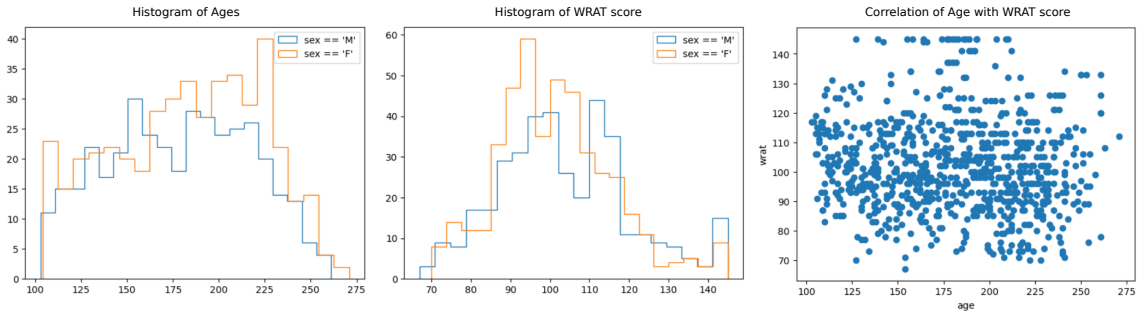


Figure 4.5: Demographics of our subset of the PNC dataset. Plots of age vs sex, WRAT vs sex, and WRAT vs age are shown. All plots created using the GUI of ImageNomer, without programming input.

## 4.3 Results and Discussion

We first present our exploration of the potential race confound in achievement score prediction from FC using ImageNomer. Based on analysis with ImageNomer, we hypothesize that due to the high correlation of FC with race and the obvious difference in achievement scores between races, prediction of achievement score from FC is solely due to a race confound. We then corroborate our hypothesis by using whole cohort and within-ethnic group regression models. Note that all Figures presented in this section are screenshots from the ImageNomer program.

### 4.3.1 Data Exploration of Confound with ImageNomer

We first confirm that age and sex are not possible confounding factors with respect to achievement score prediction. This is illustrated in Figures 4.5 and 4.6, where we see equal distributions of WRAT score among males and females and no correlation with age (raw WRAT score has been corrected for age).

Next, we use the group creation capabilities of ImageNomer to create two groups: European Ancestry (EA) and African Ancestry (AA) groups. We then compare the WRAT score distribution between the two groups, illustrated in Figure 4.7. We find that here there is a clear difference in achievement score distribution, leading to the

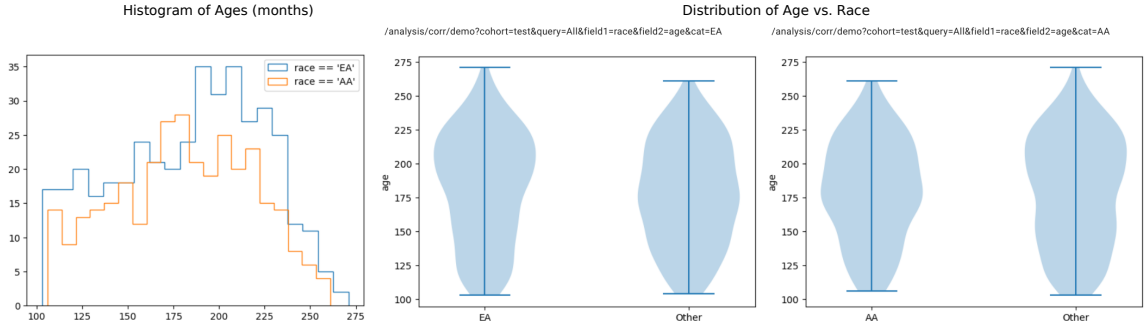


Figure 4.6: Distribution of race vs age. We see that there is no race bias on age distribution.

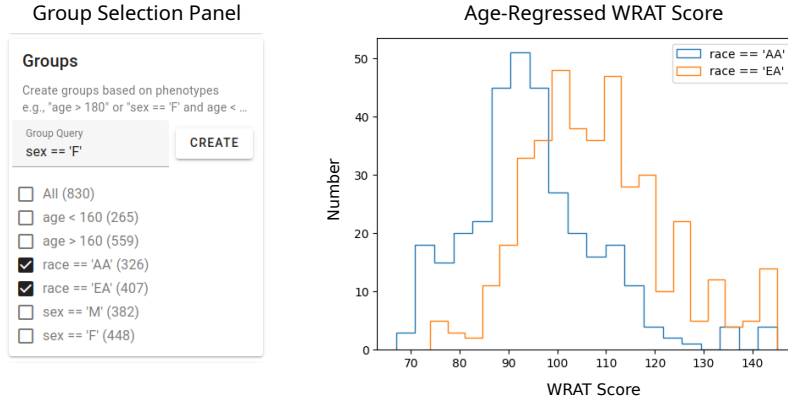


Figure 4.7: Examining race bias on WRAT score in the PNC dataset using ImageNomer. We find whereas age has been regressed from WRAT score, there is still a large racial bias.

possibility of a confounding effect if there is a race signal present in FC.

Using the FC-to-phenotype correlation feature of ImageNomer, we explore whether there is correlation between race and FC. In Figure 4.8, we find that there is a large and significant correlation between race and FC. Furthermore, in the same Figure, we show that the smaller correlation between WRAT score and FC is actually a subset of the race-FC correlation.

We perform the same analysis for SNPs, with the caveat that sex and race can be perfectly predicted using SNPs, and that SNP data does not contain any age-related signal. Nevertheless, we still attempted to find whether there was a suggestive overlap between SNPs correlated with race and SNPs correlated with high or low WRAT score. Our results are shown in Figure 4.9. From a total of 10,433 SNPs found in 100

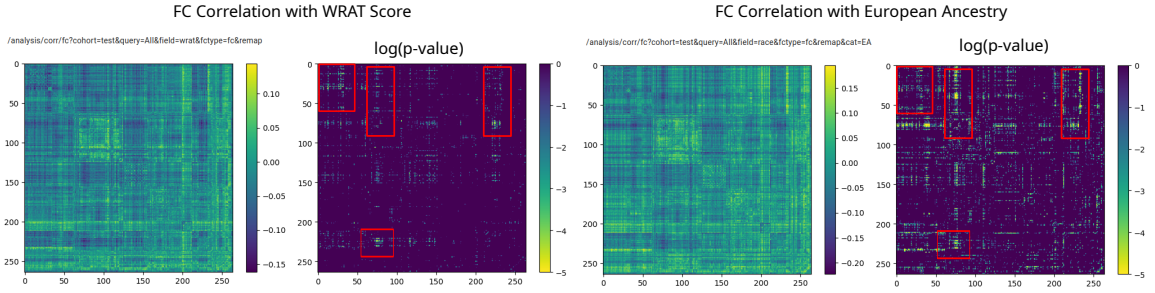


Figure 4.8: Correlation between race and FC is much higher than the correlation between race and WRAT score. Additionally, in almost all regions, achievement score-correlated FC is a subset of race-correlated FC.

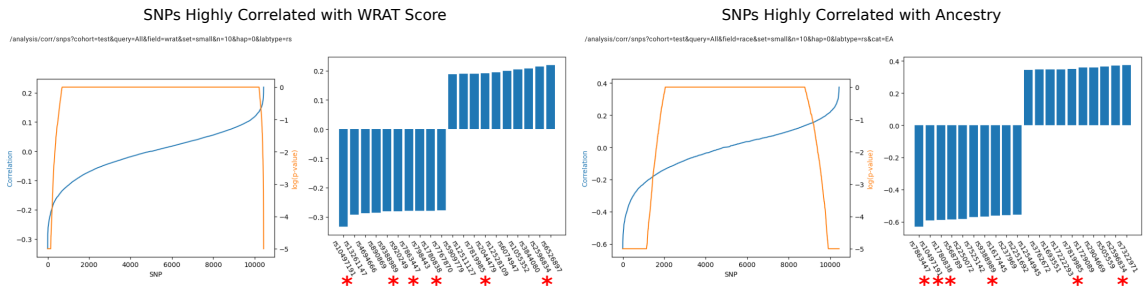


Figure 4.9: ImageNomer identifies a large overlap between SNPs correlated with race and SNPs correlated with WRAT score. Out of the top 20, 6 of the same SNP appear in both groups (marked with red asterisks).

or more subjects, we identified the top 20 SNPs correlated with race and achievement score. Of these top 20, six appeared in both the highly WRAT-correlated and highly race-correlated batches.

In summary, we use ImageNomer to form the hypothesis that race may bias FC-based prediction of achievement score if there is a race signal present in FC. We then find, using ImageNomer, that the race signal present in FC is in fact stronger than the signal for achievement score, and that WRAT score to FC correlation is a subset of race-FC correlation. Finally, we draw the same conclusion in SNP to race and SNP to achievement score correlation. In the next section, we describe the use of regression models to validate our hypothesis.

### 4.3.2 Validation with Regression Models

We validate the qualitative results from ImageNomer’s data visualization and exploration capabilities with train/test regression models. We use regularized Ridge and Logistic Regression models with an 80/20 train-test split and 20 bootstrapping repetitions to predict age, sex, race, and WRAT score. Additionally, we predict WRAT score in whole cohort as well as within intra-ethnicity groups. The results are shown in Table 4.1.

The results are as follows: age, sex, and race can all be modestly well predicted using FC. WRAT score can be predicted, although at a barely significant level, using the whole cohort, with both FC and/or SNPs as input. However, any ability to predict WRAT score disappears in race-controlled (within ethnicity) groups. This validates our hypothesis, formulated with ImageNomer via data exploration, that FC features used to predict achievement score are actually predicting ethnicity instead.

Next, we confirm the stability of race signal in FC by using both ImageNomer and transfer learning of regression models to find that race signal is at least somewhat conserved between the PNC and BSNIP datasets. Finally, we consider the effect of socioeconomic status (SES) as another potential confound besides race in predicting achievement score from FC.

### 4.3.3 Transfer of Race Prediction Models Between PNC and BSNIP

We show screenshots of ImageNomer-based data exploration for FC correlation with race in the PNC and BSNIP datasets in Figure 4.10. This figure highlights the fact that both datasets have similar correlations between specific FCs and race. We confirm the ImageNomer-based hypothesis with results for transfer of race prediction models between the PNC and BSNIP datasets, shown in Table 4.2. A Logistic Re-

Prediction	Modality	Metric	Null Model	Best Full Model	Best 10 Features
Age	FC	RMSE, months	38.4	<b>26</b>	<b>32.2</b>
WRAT Score	FC	RMSE	15.1	<b>13.6</b>	15.1
WRAT Score	SNPs	RMSE	15.1	<b>14</b>	-
WRAT Score (AA)	FC	RMSE	13.9	13.8	13.9
WRAT Score (AA)	SNPs	RMSE	13.9	13.4	-
WRAT Score (EA)	FC	RMSE	14	14.1	14
WRAT Score (EA)	SNPs	RMSE	14	13.6	-
Race	FC	Accuracy	55%	<b>85%</b>	<b>72%</b>
Sex	FC	Accuracy	51%	<b>78%</b>	<b>62%</b>

Table 4.1: Summary of prediction results for full models (34,716 features for FC, 10,433 features for SNPs) and top 10 feature models in the PNC dataset. Top 10 features selected on the training set. Statistically significant results are shown in bold.

Trained on PNC		Trained on BSNIP	
Evaluation Group	Accuracy	Evaluation Group	Accuracy
PNC (all, n=733)	85±3%	BSNIP (all, n=1165)	79±4%
BSNIP AA (n=387)	76±5%	PNC EA (n=407)	90±3%
BSNIP CA (n=778)	64±5%	PNC AA (n=326)	38±7%

Table 4.2: Accuracy of transfer learning between the PNC and BSNIP datasets. All predictions are better than the null model, except for identification of the AA group in the PNC dataset by a model trained on BSNIP.

gression model trained on the PNC dataset was able to predict race in the BSNIP dataset with an average accuracy of 68%. When trained on BSNIP and evaluated on PNC, the average prediction accuracy was 66%. We find that the prediction is less good than within-dataset prediction, although still better than chance. It should be taken into account that the PNC dataset is made up of healthy adolescents, while the BSNIP dataset contains schizophrenia and bipolar patients, relatives of patients, and healthy controls. Figure 4.10 shows a comparison between race correlation and FC in the PNC and BSNIP datasets, created using ImageNomer.

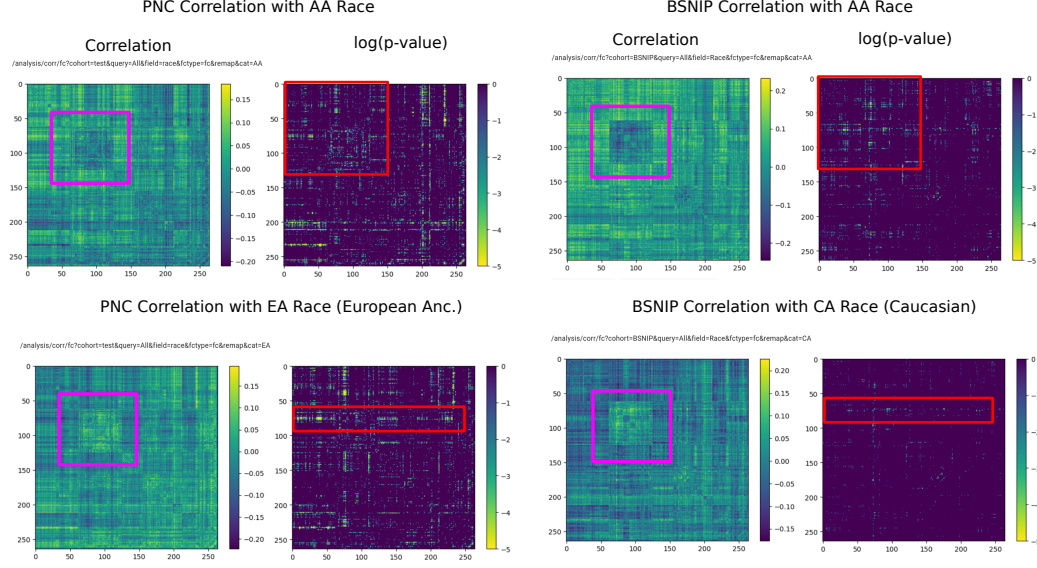


Figure 4.10: Correlation of FC with race in the PNC and BSNIP datasets. Although BSNIP p-values are lower, we see the same pattern of correlation. Additionally, the overall FC in the Default Mode Network (DMN), highlighted in pink, seems to be highly predictive of race.

#### 4.3.4 Effect of Socioeconomic Status Explored

We consider socioeconomic status (SES) as another confounding factor when predicting scholastic achievement based on a standardized test, with the majority of analysis again carried out using ImageNomer. Predictive models were only used to validate the conclusions made using data exploration in ImageNomer.

A problem is that SES was not directly measured in the PNC study, in that the income of family groups was not known. However, previous studies have used parental education levels as a proxy for SES [243], and this information was included in the PNC dataset. Indeed, as seen in Figure 4.11, we find that SES, race, and WRAT score are all inter-related. We see that non-EA ethnicity tend to have lower SES as measured by mother education level. The correlation of father education level with FC was similar to mother education, although less significant. It should be noted that many children had missing values for father education level.

We see in Figure 4.11 that SES, ethnicity, and WRAT score correlate to similar re-

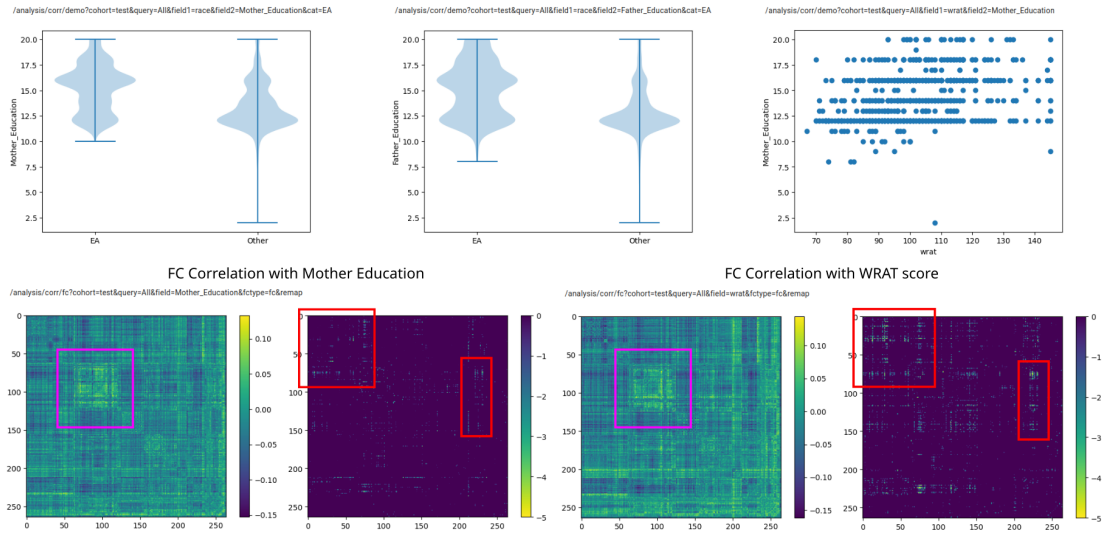


Figure 4.11: Top: distribution of mother and father education level by race category and distribution of WRAT score with mother education level. Bottom: correlation of FC with mother education level and WRAT score. Correlation consists of a correlation image and the negative log base 10 of the Bonferroni-corrected p-value, clipped at -5.

Group	WRAT score RMSE	Null model RMSE
Low SES (Mother Education $\leq$ 12 years)	14.1	15
High SES (Mother Education $\geq$ 14 years)	15	15.3

Table 4.3: Prediction of WRAT score in the low SES (mother with no college education) versus high SES (mother with some college education). Predictive ability was barely significant in the low SES group, and not significant in the high SES group.

gions on the FC map. The p-values associated with FC-SES correlation (as measured by mother education) are somewhat lower than those associated with FC-WRAT or FC-ethnicity correlation, but still significant. Additionally, performing regression analysis for WRAT score based on FC in low SES (mother education  $\leq 12$  years) and high SES (mother education  $\geq 14$  years) groups, we find a barely significant ability to predict achievement in the low SES group but not a significant ability in the high SES group. The results are shown in Table 4.3. The WRAT prediction accuracy in the low SES group is worse than in the cohort as a whole (compare 13.6 RMSE vs 14.1 RMSE). We conclude that SES is a confounding factor in WRAT score prediction, though not as severe as ethnicity in this dataset. Finally, we reject the idea that race is a causal factor in achievement or WRAT score, but only point out the potential confounding effects if race or SES is not taken into account in studies seeking to find markers of high or low achievement, and the ease with which such confounds were found using ImageNomer.

## 4.4 ImageNomer Conclusion

We present ImageNomer, a new fMRI and omics visualization and analysis tool. We note that most of the figures shown in this manuscript were created as screenshots of the working tool. We use this tool to examine the large PNC dataset and discover features important for phenotype prediction. As validation for ImageNomer-based correlation analysis, we find that age, sex, and race can be moderately well predicted by FC features, with 10 FC features giving up to 72% race prediction accuracy, compared with 85% for the full model.

We find both FC features and SNPs can somewhat predict scholastic knowledge and problem-solving ability, as measured by WRAT score, but that this is probably due to a race confound. When controlling for race, FC-based achievement score

prediction drops to the same accuracy as the null model and the SNP-based prediction becomes statistically insignificant. We conclude that, on average, the effect of either SNPs or FC features on scholastic achievement in normal children is very small, if one exists at all. Additionally, we find that race prediction from FC is at least somewhat robust between different datasets. Using ImageNomer, this work quickly and easily identifies race as an important confounding factor in FC and casts doubt on the ability to predict achievement-related features from both FC and SNP data.

Finally, we note that it is very easy to add additional datasets to explore into the ImageNomer program. To do so, follow the links given in the footnotes in Section 4.2.3 and read the corresponding instructions. Doing so requires following a Jupyter notebook, but once data is loaded into ImageNomer, it can be explored without writing any additional code. We find the ability to quickly visualize trends, correlations, and potential confounding effects provided by the ImageNomer software is invaluable to the ability to perform good and careful research. This is demonstrated by the rapid identification of a race confound on FC-based prediction of achievement using ImageNomer, despite the fact that many studies have attempted to predict achievement using FC with little or no mention of this effect [105, 148, 235].

## 4.5 Demographic Variational Autoencoder for Removal of Confounds

It is well known that fMRI can be used to predict demographics such as age, sex, and race [83, 148, 150]. It is also known that it is crucial to control for demographic confounds when performing statistical analysis [244, 245]. In fact, many simpler models have provisions for regressing out confounds [139]. There is a question, however, as to whether fMRI-based prediction using more complicated models is solely due to demographic signal present in fMRI [83]. To this end, we present a new generative model based on a VAE that decorrelates latent features from subject demographics (DemoVAE). It accomplishes this by forcing such correlations to be zero during training and injecting demographic information in the decoder after calculation of the latent features. We add classifier and regression-guided loss functions [246] to ensure that synthetic samples contain demographics-associated features that are compatible with models trained on real data. We believe our model serves two purposes: 1) generation of representative synthetic data based on datasets that are not accessible to the general public, and 2) creation of fMRI latent features which are free from the confounding effects of demographics. It is also possible that DemoVAE can aid in data harmonization by removing site-specific effects [139] through treating site location as a demographic. These capabilities are validated on two large datasets accessible to qualified researchers.

### 4.5.1 Formulation

First, we discuss the architecture and training of the DemoVAE model, shown in Figure 4.12. Next, we describe two datasets used for the validation of the model. Then, we outline experiments used to analyze DemoVAE’s ability to decorrelate latent features from demographic confounds as well as to generate high quality synthetic

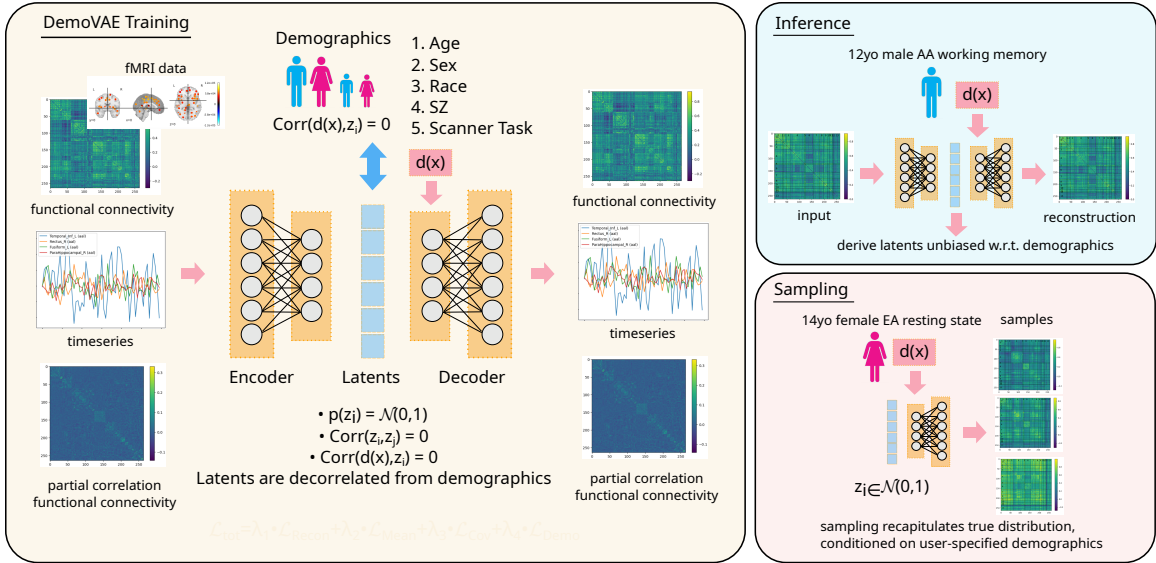


Figure 4.12: Overview of the demographics-conditioned and decorrelated variational autoencoder (DemoVAE) model. Instead of reconstruction based only on latent features  $\mathbf{z} = E_\phi(\mathbf{x})$ , the DemoVAE model uses demographics  $\mathbf{y}$  as input to the decoder  $\hat{\mathbf{x}} = D_\theta(\mathbf{z}, \mathbf{y})$ . The two main uses of the model are inference, which generates latent features  $\mathbf{z}$  decorrelated from demographics, and sampling, which generates synthetic fMRI data conditioned on user-provided demographics.

fMRI data. Finally, we describe experiments using DemoVAE for imputation of fMRI data.

## Variational Autoencoder

An autoencoder (AE) converts raw features into a lower-dimensional latent space via a learned encoder function  $\mathbf{z} = E_\phi(\mathbf{x})$ , along with a decoder function to convert the latent features back into a reconstructed version of the input  $\hat{\mathbf{x}} = D_\theta(\mathbf{z})$ . The AE is often trained to minimize the difference between the reconstruction  $\hat{\mathbf{x}}$  and original input  $\mathbf{x}$ . Thus, the AE may be seen as a nonlinear version of dimensionality reduction techniques such as PCA or Factor Analysis.

By contrast, a variational autoencoder (VAE) trains the encoder function  $E_\phi(\mathbf{x})$  to produce latent features that approximate a known probability distribution  $p_\theta(\mathbf{z})$ , most often taken to be a standard multivariate Gaussian distribution  $p_\theta(\mathbf{z}) = \mathcal{N}(\mathbf{0}, \mathbf{I})$  [247]. This allows for artificially constructing latent samples  $\mathbf{z}_{\text{samp}}$  from the approximated

distribution, followed by the conversion of those latents to samples of the original distribution  $p_\theta(\mathbf{x}|\mathbf{z})$  by passing through the decoder function  $\mathbf{x}_{\text{samp}} = D_\theta(\mathbf{z}_{\text{samp}})$ .

For the following, consider scalar features  $x$  and scalar latent features  $z$ . The exact calculation of  $p_\theta(z|x)$  is in most cases intractable, therefore an approximation  $q_\phi(z|x) \approx p_\theta(z|x)$  is made, and the Kullback-Leibler (KL) divergence between the two distributions is taken:

$$\begin{aligned} D_{KL}(q_\phi(z|x) \| p_\theta(z|x)) \\ = \mathbb{E}_{z \sim q_\phi(\cdot|x)} \left[ \ln \frac{q_\phi(z|x)}{p_\theta(z|x)} \right] \\ = \ln p_\theta(x) + \mathbb{E}_{z \sim q_\phi(\cdot|x)} \left[ \ln \frac{q_\phi(z|x)}{p_\theta(x, z)} \right] \end{aligned} \quad (4.1)$$

The evidence lower bound (ELBO) [247] is then defined as:

$$\begin{aligned} L_{\theta, \phi} &= \mathbb{E}_{z \sim q_\phi(\cdot|x)} \left[ \ln \frac{p_\theta(x, z)}{q_\phi(z|x)} \right] \\ &= \mathbb{E}_{z \sim q_\phi(\cdot|x)} [\ln p_\theta(x|z) - D_{KL}(q_\phi(z|x) \| p_\theta(z))] \end{aligned} \quad (4.2)$$

Maximizing the ELBO is equivalent to maximizing the reconstruction probability  $\ln p_\theta(x|z)$  while minimizing the KL divergence between our empirical and target distributions. Given a standard normal distribution for the latent features  $p_\theta(z) = \mathcal{N}(0, 1)$ , the ELBO objective to be minimized becomes:

$$\mathcal{L}_{\theta, \phi} = \|x - D_\theta(z)\|_2^2 + N\sigma_z^2 + \|\mu_z\|_2^2 - N\ln\sigma_z^2, \quad (4.3)$$

where  $\mu_z$  represents the mean of the the empirically calculated latent features,  $\sigma_z^2$  represents the variance of the same, and  $N$  represents the number of samples. This loss function can be seen to have three components: a reconstruction loss, two terms

that tend to make  $\sigma_z$  equal to one, and one term to make the expectation of the latent features equal to zero. Given this loss function, one is able to train a network to sample the distribution of FC data, but not to condition the samples on ancillary subject information such as demographics.

When considering a multivariate standard normal distribution  $p_\theta(\mathbf{z}) = \mathcal{N}(\mathbf{0}, \mathbf{I})$  for the latent features, the KL divergence part takes the more complicated form [248]:

$$\begin{aligned} D_{KL}(\mathcal{N}(\mu_z, \Sigma_z) \| \mathcal{N}(\mathbf{0}, \mathbf{I})) &= \\ \frac{1}{2} [\text{tr}(\Sigma_z) + \mu_z^\top \mu_z + \log(\det(\Sigma_z))] \end{aligned} \tag{4.4}$$

This presents a challenge due to the calculation of, and backpropagation through, the log determinant of the empirical latent covariance matrix  $\Sigma_z$ . We address this issue as part of our modifications to the VAE loss function presented in Section 4.5.1.

### **Demographics-Conditioned and Decorrelated Variational Autoencoder (De-moVAE)**

There is an existing body of academic literature [249, 250] as well as practical applications [251] exploring the conditioning of VAEs on user-specified inputs. VAEs have also been applied to the generation of synthetic fMRI data[252], but without considering patient demographics. In this work, we include the known patient demographic features as input to the decoder function  $\hat{\mathbf{x}} = D_\theta(\mathbf{z}, \mathbf{y})$ , where  $\mathbf{z}$  are the latent features and  $\mathbf{y}$  are the subject demographics. During training, we decorrelate the latent state  $\mathbf{z} = E_\phi(\mathbf{x})$  from demographic features  $\mathbf{y}$  so that all of the fMRI signal that can be attributed to demographics is based on user-provided input and not on the encoded latent features. To this end, we make several modifications to the traditional VAE loss function.

## Incorporate Demographic Information

First, the reconstruction error term of the loss function remains unchanged from the ELBO formulation, except for the injection of demographic information:

$$\mathcal{L}_{\text{Recon}} = \frac{1}{N} \sum_{i=1}^N \|\mathbf{x}_i - D_\theta(\mathbf{z}_i, \mathbf{y}_i)\|_2^2, \quad (4.5)$$

where  $N$  is the number of subjects,  $\mathbf{x}_i$  are the vectorized FC features,  $\mathbf{z}_i = E_\phi(\mathbf{x}_i)$  are the empirically calculated latent features, and  $\mathbf{y}_i$  are the subject demographics for subject  $i$ .

## Extension to Multidimensional Latent Space

Second, we note that the ELBO loss function of the standard VAE is applicable to scalar latent features  $z$  and not multi-dimensional latent features  $\mathbf{z} \in \mathbb{R}^{N_z}$ . This may allow for a non-diagonal covariance matrix in the empirical distribution of latents  $q_\phi(\mathbf{z}|\mathbf{x}) = \mathcal{N}(\mathbf{0}, \Sigma)$ . Thus, we modify a part of the ELBO loss function to specifically target a diagonal covariance matrix and zero expected value for the latents:

$$\begin{aligned} \mathcal{L}_{\text{Cov}} &= \frac{1}{N} \|\mathbf{Z}\mathbf{Z}^\top - N\mathbf{I}\|_{\text{F}}^2 \\ \mathcal{L}_{\text{Mean}} &= \frac{1}{NN_z} \sum_{i=1}^{N_z} \|\mu_{\mathbf{z}_i}\|_2^2, \end{aligned} \quad (4.6)$$

where  $\mathbf{Z} \in \mathbb{R}^{N_z \times N}$  is the matrix of all  $N_z$  latent features for all  $N$  subjects,  $\mathbf{z}_i$  is the vector of latent feature  $i$  for all  $N$  subjects, and  $\mu_{\mathbf{z}_i}$  is its mean. We find that this loss function performs as good or better than the KL divergence part of ELBO with fMRI data.

## Decorrelate Latent Features from Demographics

Third, we add a term penalizing correlations between the empirical latent features and four demographic features or clinical outcomes: age, sex, race, and disease status (schizophrenia diagnosis). Where we have multiple fMRI scans using different scanner tasks for each subject, we also decorrelate the latents with respect to scanner task.

We define

$$\mathcal{L}_{\text{Demo}} = \frac{1}{N_z N_y} \sum_{j=1}^{N_z} \sum_{k=1}^{N_y} \|\rho_{\mathbf{z}_j, \mathbf{y}_k}\|_2^2, \quad (4.7)$$

where  $\rho_{\mathbf{z}_j, \mathbf{y}_k}$  is the correlation between between latent feature  $\mathbf{z}_j$  and demographic feature  $\mathbf{y}_k$  across all  $N$  subjects.

## Classifier Guidance

Finally, while training the DemoVAE, we create synthetic samples based on random choices of demographic inputs, and penalize miss-predictions relative to pre-trained models. Given a single demographic prediction from a synthetic latent based on user-input demographics  $\hat{y}_i = f_i(D_\theta(\mathbf{z}_{\text{samp}}, \mathbf{y}))$ , we define

$$\mathcal{L}_{\text{Guide}} = \frac{1}{N_y} \sum_{i=1}^{N_y} \begin{cases} \|y_i - \hat{y}_i\|_2^2, & \mathbf{y}_i \text{ continuous} \\ -\sum_c y_{i,c} \log(p_{i,c}), & \mathbf{y}_i \text{ categorical} \end{cases} \quad (4.8)$$

where the models  $f_i(\cdot)$  are linear models trained on the ground truth fMRI subject data,  $y_{i,c}$  is the one hot encoded true class label for demographic  $i$ ,  $p_{i,c}$  is the predicted probability for class  $c$  and demographic  $i$ , and the loss is the Mean Square Error (MSE) for continuous demographics (age) and Cross Entropy (CE) error for categorical demographics (sex, race, disease status, scanner task).

The final loss function for training the DemoVAE can thus be formulated as:

$$\begin{aligned}\mathcal{L} = & \mathcal{L}_{\text{Recon}} + \lambda_1 \mathcal{L}_{\text{Cov}} + \lambda_2 \mathcal{L}_{\text{Mean}} + \\ & \lambda_3 \mathcal{L}_{\text{Demo}} + \lambda_4 \mathcal{L}_{\text{Guide}},\end{aligned}\tag{4.9}$$

where  $\lambda_{1-4}$  are the hyperparameters chosen alongside learning rate and latent dimension size via random grid search.

#### 4.5.2 Validation of fMRI Samples Generated by DemoVAE

Several tests were performed to validate that the samples created by DemoVAE accurately capture the distribution of fMRI data and recapitulate group differences between groups having different demographics. We first trained the DemoVAE model using the PNC dataset, including age, sex, and race as demographics, and with the scanner task being set to resting state. We also trained a traditional VAE using the traditional scalar ELBO objective in Equation 4.3 and no demographic information, as well as a Wasserstein generative adversarial network (W-GAN) model [253–255]. Synthetic FC samples were then generated for 1,000 subjects using all three models, and the distribution of FC features was visualized in two dimensions using the scikit-learn implementation of t-distributed stochastic neighbor embedding (t-SNE) [166, 256]. Subject demographics for the DemoVAE features were sampled randomly using an equally-weighted Bernoulli (sex, race) or normal (age) distribution. The distribution of synthetic data was compared with ground truth data.

Additionally, we measured the ability of DemoVAE synthetic data to recapitulate group differences in the PNC and BSNIP datasets. We calculated the mean difference in FC between young children and young adults, males and females, EA and AA race, and SZ patients and healthy controls using ground truth data. Then, we created synthetic FC data for those groups using DemoVAE, and compared group differences of real and synthetic data. The RMSE between FC differences of real

and synthetic data was calculated and compared with a null model.

Figure 4.13 displays a selection of ground truth subject FC data compared to synthetic data generated by DemoVAE, a traditional VAE, and a W-GAN. We note that it is visually hard to distinguish between true subject data and synthetic data. However, this is not the case when comparing the entire distribution of data using t-SNE, as evident in Figure 4.14. Figure 4.14 shows the distribution of synthetic DemoVAE data, VAE data, and W-GAN data transformed using t-SNE overlayed on ground truth resting state PNC subject data. DemoVAE data was created using randomly sampled age, sex, and race demographics but with scanner task set to resting state. We see that DemoVAE captures the distribution of fMRI data better than the traditional VAE and W-GAN. It is evident that a GAN makes no guarantees about matching or even approximating the true distribution of data [248] unless additional regularization is performed.

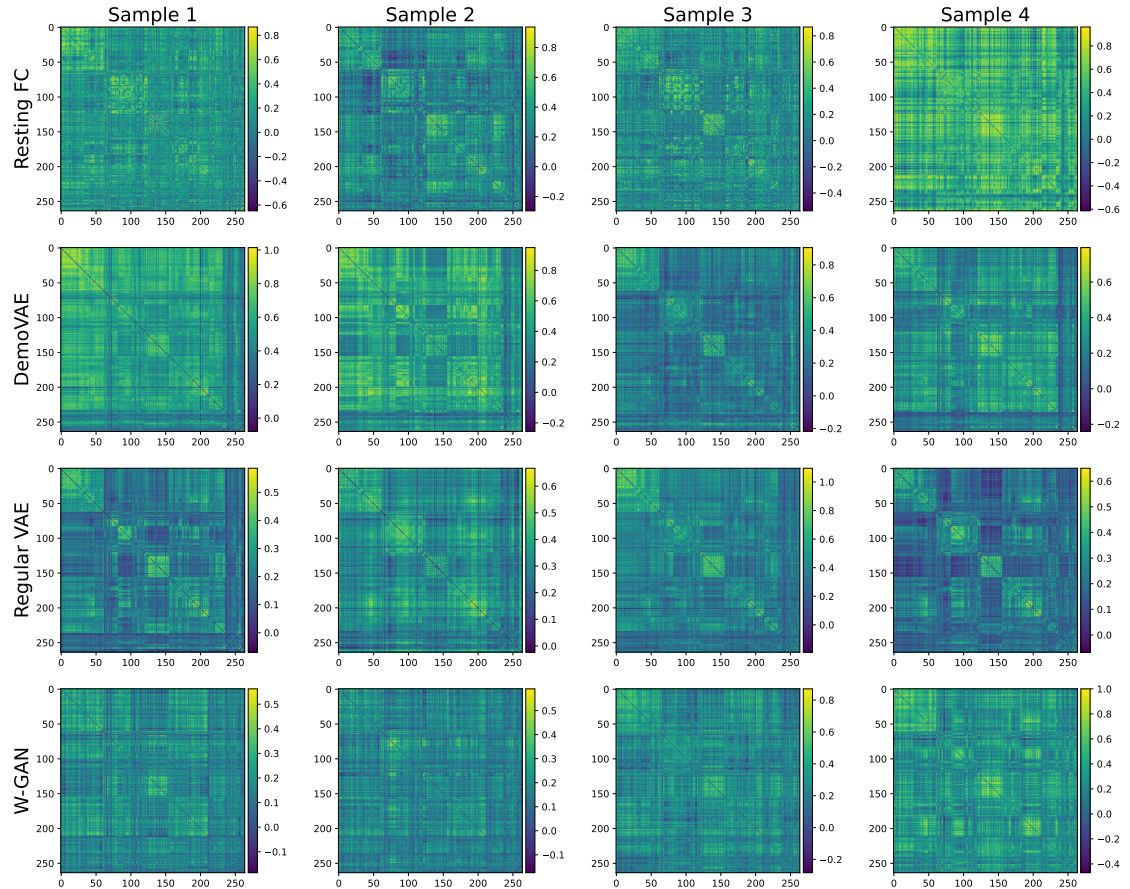


Figure 4.13: Sampled FC matrices for real PNC resting state scans (top) compared to synthetic DemoVAE, VAE, and W-GAN FC data. Visually, all synthetic models generate convincing data.

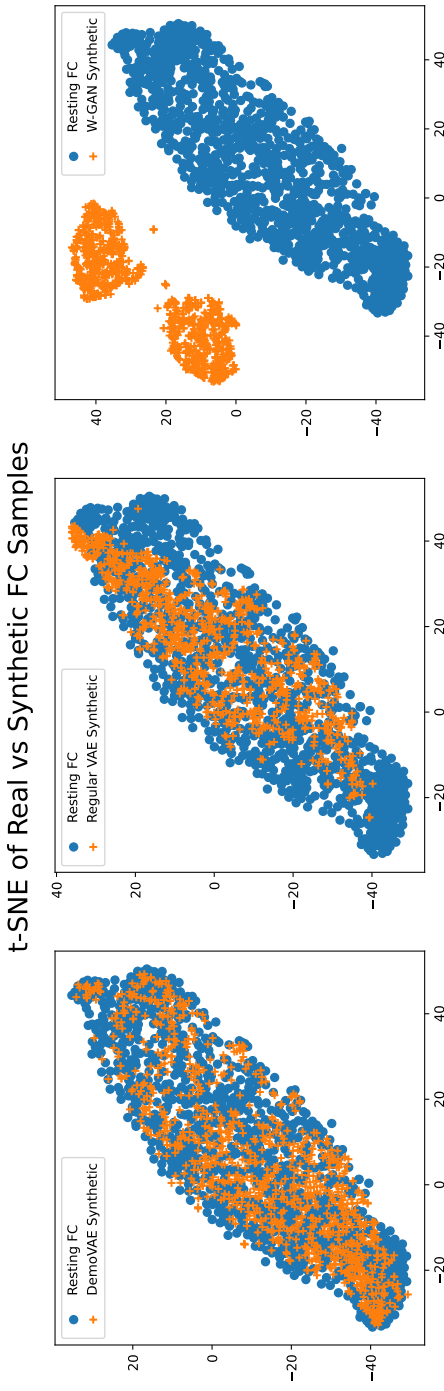


Figure 4.14: t-SNE embeddings of synthetic FC data from DemoVAE, traditional VAE, and W-GAN models overlayed on top of t-SNE embeddings of real resting state FC data from the PNC dataset. Blue circles represent embeddings of real subject FC data while orange crosses represent embeddings of synthetic data. We see that DemoVAE captures the distribution of fMRI FC data as well as or better than a traditional VAE and better than a GAN.

Figure 4.15 displays group differences between demographic subsets of real data compared to group differences from synthetic DemoVAE data. We see that by conditioning on demographic input, DemoVAE can produce samples that accurately recapitulate group differences in FC data.

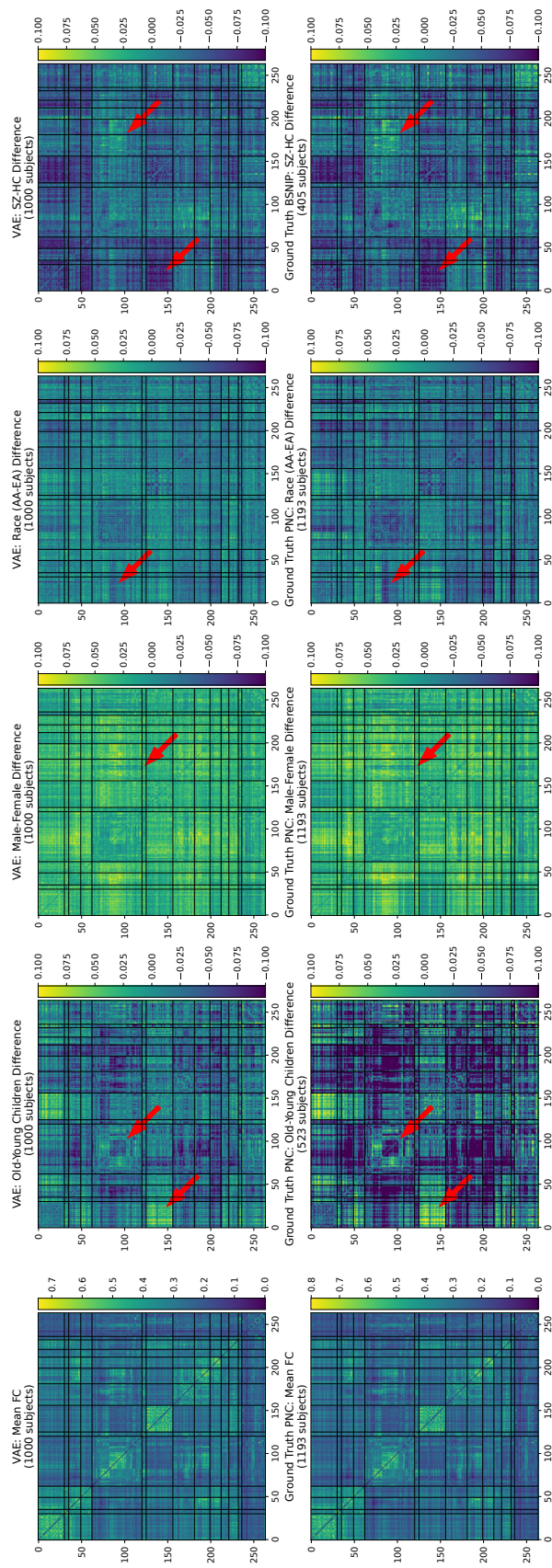


Figure 4.15: Group FC differences using real data and synthetic data generated by DemoVAE conditioned on appropriate demographic input. Top: synthetic DemoVAE data, bottom: real data. From left to right, we see that DemoVAE qualitatively recapitulates group differences in the PNC (mean, age, sex, race) and BSNIP (SZ diagnosis) datasets. Arrows point out FC features in real data that are reproduced in synthetic DemoVAE samples. Brain functional networks for the Power atlas, shown left to right and top to bottom in FC matrices, are given in Table 4.4.

Label	ROIs	Network Name
0	0-29	Somatomotor Hand (SMT)
1	30-34	Somatomotor Mouth (SMT)
2	35-48	Cinguloopercular (CNG)
3	49-61	Auditory (AUD)
4	62-119	Default Mode (DMN)
5	120-124	Memory (MEM)
6	125-155	Visual (VIS)
7	156-180	Frontoparietal (FRNT)
8	181-198	Salience (SAL)
9	199-211	Subcortical (SUB)
10	212-220	Ventral Attention (VTRL)
11	221-231	Dorsal Attention (DRSL)
12	232-235	Cerebellar (CB)
13	236-263	Uncertain (UNK)

Table 4.4: Brain functional networks in the Power264 atlas [5].

#### 4.5.3 Additional Insight on Demographic Confounds in FC

We describe two experiments to test how much demographic confounds influence prediction using functional fMRI data.

##### Prediction of WRAT Score Using DemoVAE Latents

We used the PNC dataset to predict age-adjusted WRAT score, which is heavily skewed according to ethnic group (Figure 4.16), using fMRI FC data, SNP data, scalar race indicator, and DemoVAE latents constructed from FC or SNPs. Ridge regression models were trained and evaluated on a set of 20 repetitions of an 80/20 train/test split with the above features, where the best value for the regularization parameter was chosen by random grid search. This experiment was performed to validate the ability of DemoVAE to decorrelate its latent features from demographics, and to demonstrate why demographic confounds in FC may be problematic for downstream analysis.

In Table 4.5, we give results for predicting age-adjusted WRAT score in the PNC

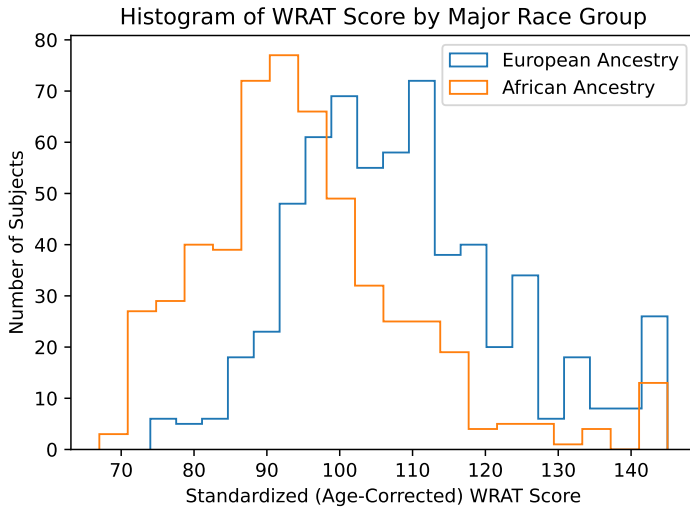


Figure 4.16: Histogram of standardized (age-correct) WRAT score from the PNC dataset, split among the two major race groups in the dataset. There is a clear demographic confound when predicting WRAT score from fMRI or genomic data. We show in Table 4.5 that DemoVAE is able to remove the effect of this confound, but at the same time, removes the ability to accurately predict WRAT score.

data from scalar race value, FC data, SNP data, DemoVAE latents derived from FC data, and DemoVAE latents derived from SNPs. We observe that using the scalar race variable yields the best prediction of standardized WRAT score. While FC and SNPs can predict WRAT score moderately well, that predictive ability disappears when latents are decorrelated from race, as in the DemoVAE latents. This demonstrates that DemoVAE is able to decorrelate the fMRI latent state from demographics. It also demonstrates that, while FC and SNPs have the ability to predict age-adjusted WRAT score, that prediction is based on ability to infer demographics, and not on any cognitive signal found in FC that is independent of demographics. We find, as have previous studies, that prediction of scholastic achievement may be highly confounded by race signal present in neuroimaging data [83, 237].

### Correlation of Clinical Measures with DemoVAE Latents

We tested the correlation of fMRI FC data with phenotype and clinical data fields before and after the removal of the confounding effects of demographics. Both the

Input	WRAT Prediction RMSE
Null Model	15.18
Race Scalar Only	<b><math>13.91 \pm 0.271</math></b>
Rest FC	$14.73 \pm 0.368$
Nback FC	$14.44 \pm 0.395$
Emoid FC	$14.46 \pm 0.414$
SNPs	$14.03 \pm 0.429$
Rest DemoVAE Latents	$15.20 \pm 0.015$
Nback DemoVAE Latents	$15.18 \pm 0.013$
Emoid DemoVAE Latents	$15.18 \pm 0.015$
SNP DemoVAE Latents	$15.14 \pm 0.131$

Table 4.5: RMSEs (mean and standard deviation) of predicting standardized WRAT scores using fMRI FC input, SNP input, DemoVAE fMRI latents, DemoVAE SNP latents, and scalar race variable. We find that race information alone provides the best predictor of WRAT score, followed by SNPs and then by task-based fMRI FC.

PNC and BSNIP dataset contain phenotype and clinical data which may be correlated with FC features. A subset of 169 phenotype, medication, and cognitive battery fields available in the PNC cohort was correlated with raw FC data, traditional VAE latents, and DemoVAE latents decorrelated from demographic features. Correlation was tested at a significance level of  $p < 0.05$  and  $p < 0.01$ , and the number of significant correlations was determined. Significance was determined using a t-test with the statistic:

$$t = \frac{\rho\sqrt{n-2}}{\sqrt{1-\rho^2}}, \quad (4.10)$$

where  $\rho$  was the correlation coefficient between FC or latent feature and clinical or computerized battery field and  $n$  was the number of samples, i.e., number of subjects having a value for that clinical or computerized battery field. Each FC, VAE, or DemoVAE feature was correlated independently and Bonferroni correction was applied to the p-value to correct for multiple comparisons.

In addition to the PNC clinical fields, the BSNIP dataset contained 32 demographic, clinical, and medication fields which were correlated with FC data and VAE latent features in a similar manner. Finally, the PNC dataset contained genomic data

for a 1,154-subject subset of subjects with fMRI scans. These genomic data were also correlated with phenotype and cognitive battery fields before and after removal of confounding effects with DemoVAE.

Figure 4.17 displays the correlation between clinical questionnaire and computerized battery fields of the PNC and BSNIP datasets and fMRI FC data, traditional VAE latents, and demographically-unconfounded DemoVAE latents. We see that removing the effects of demographic confounds from either fMRI data or SNP data greatly reduces the number of fields that are significantly correlated with the fMRI or genomic data. In fact, of 169 clinical or computerized battery fields, only four remained significantly correlated at the  $p < 0.01$  level after decorrelation from demographics. This result corroborates the result presented in Section 4.5.3, where it was found that scalar race value was the best predictor of scholastic achievement as measured by WRAT score. While FC and SNPs were found to be somewhat predictive of WRAT score, that predictive ability disappeared when FC features were decorrelated from the demographics age, sex, and race using DemoVAE.

Unlike the PNC dataset, from which we used 169 questionnaire and computerized battery fields, the BSNIP dataset included a more modest 32 clinical fields available for analysis. All fields including descriptions are available at the GitHub repository accompanying this manuscript. When processing BSNIP data with DemoVAE, we used age, sex, race, and schizophrenia diagnosis as demographic variables to decorrelate latent features. Interestingly, the five BSNIP fields that remained correlated to DemoVAE latent features at a significance of  $p < 0.05$  were related to medication (taking or not taking anti-psychotics,  $p < 0.0218$ ) or Positive and Negative Syndrome Scale (PANSS) assessment as to the severity of schizophrenia symptoms [257]. These included total positive symptom score ( $p < 0.0098$ ), total negative symptom score ( $p < 0.0296$ ), total general symptom score ( $p < 0.0011$ ), and total PANSS score ( $p < 0.00033$ ). This seems to imply that type or severity of schizophrenia symptoms

[258] may have effects in fMRI data which are not accounted for by a simple binary diagnosis of the condition or demographics.

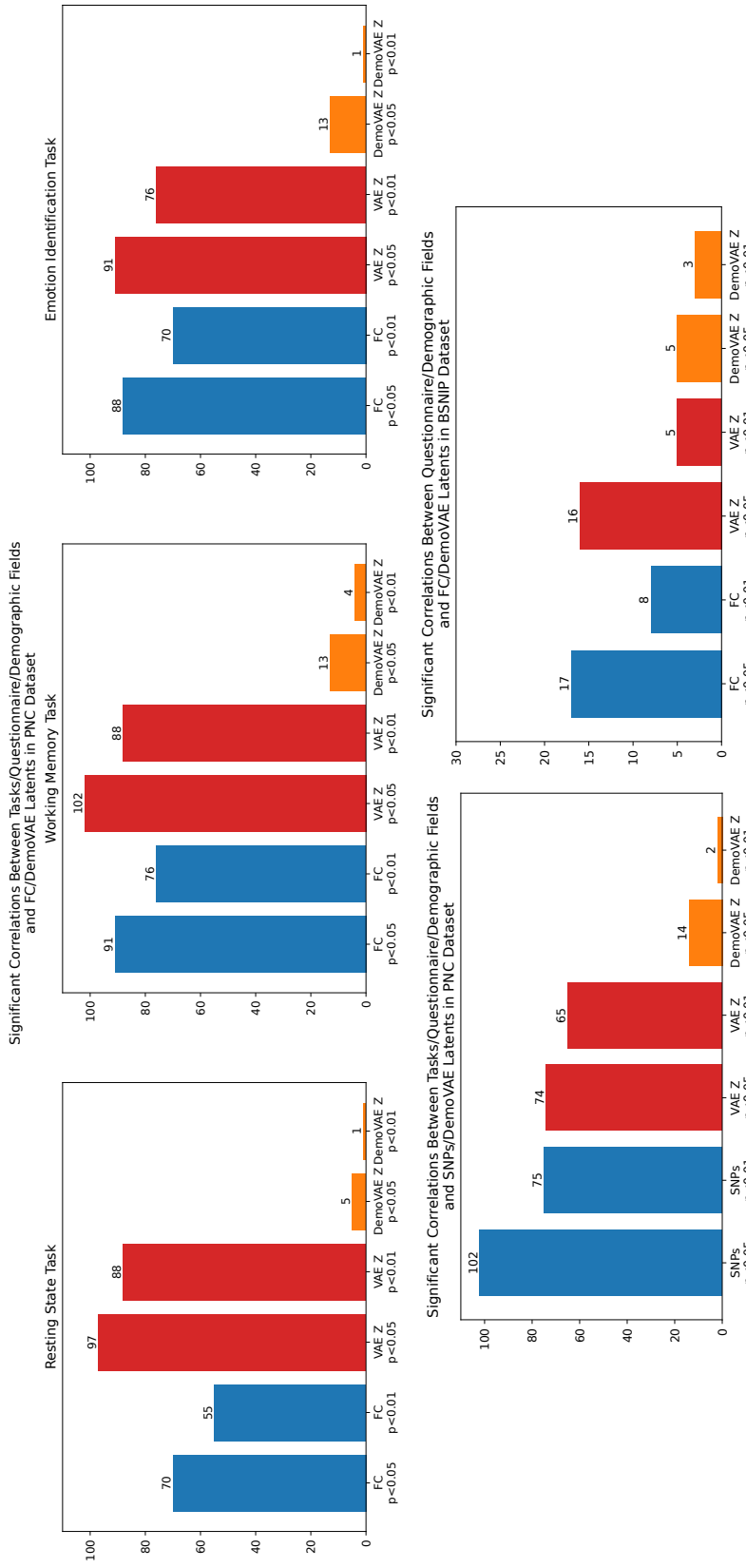


Figure 4.17: Correlation of questionnaire, computerized battery, and clinical fields with fMRI FC data versus traditional VAE or decorrelated DemoVAE latent features. Top: PNC dataset fMRI data, left bottom: PNC dataset SNP data, right bottom: BSNIP dataset fMRI data. There were a total of 169 fields in the PNC dataset and 32 in the BSNIP dataset. We see that both FC and traditional VAE latents, which are confounded by patient demographics, have significant correlations with more than half of all fields. Once demographic confounds are removed with DemoVAE, however, both FC and SNP data are significantly correlated with only a small percentage of fields. A list of the fields used is available in the GitHub repository. Blue color=correlation with FC features, Red color=correlation with regular VAE latents, Orange color=correlation with DemoVAE latents

# Chapter 5

## Conclusion

This thesis has explored the interplay of functional connectivity connectomes and phenotypic variables, using state of the art machine learning models to predict phenotypes based on FC features and/or SNPs. It has identified robust changes in a large longitudinal aging dataset (UK Biobank) and found that connectivity between the somatomotor and visual networks was the best predictor of relative age in older subjects. Specifically, we have found that somatomotor-visual connectivity increases from younger age to older age. Interestingly, as shown in Figure 4.15, the same connectivity difference is found between younger and older subjects in the developmental PNC dataset. Identifying such organic FC differences in non-pathological aging is important when FC features are brought in to identify pathological changes, such as changes in brain age associated with, e.g., Alzheimer's disease or mild cognitive impairment.

Additionally, this thesis has detailed the creation of ImageNomer, a software package for the quick and accurate analysis of correlations between and among FC, SNPs, and phenotypic variables. We have demonstrated the use of this software package to associate both FC and SNPs with test taking ability, as represented by WRAT score. We have also used this software package to identify FCs correlated with the demo-

graphic of race. Interestingly, we found that unequal distribution of WRAT score among different ethnic groups highly biases WRAT score prediction. This software package therefore has found use for both its own merit in quickly finding correlations in large datasets as well as well as finding an under-reported demographic confound.

This thesis has shown that FC can reliably predict the phenotypes age, sex, and WRAT score. However, as discussed in Section 4.5.3, FC data can and is influenced heavily by these demographic confounds, for example when predicting WRAT score. In fact, we have shown that once demographics of age, sex, race, and the non-demographic of scanner task are accounted for, the number of clinical variables significantly correlated with both FC and SNP data is reduced substantially. Fortunately for clinical application of FC, correlation with schizophrenia disease status as well as medication status and schizophrenia severity status remains even after accounting for demographics.

## 5.1 Future Work

Looking ahead, the future seems bright for the application of machine learning to ever-larger cognitive datasets. However, as shown in this thesis, care must be taken to remove demographic confounds from such data. In particular, it may be necessary to acquire data at a more granular level than that permitted by fMRI, where demographic confounds are responsible for the majority of FC-clinical variable correlations. Particularly, modalities such as EEG and MEG capture data at a much greater temporal resolution than fMRI, which may help tease apart differences in cognitive behaviors. Integration of fMRI data with other modalities of MRI, such as structural or diffusion MRI, may also be explored.

The FC used in this thesis has been so-called static FC, which uses the whole scanning session to construct the connectome. FC may also be dynamic, where several

different connectomes are created during a scanning session by using sliding window or other techniques. The changes in connectome may hold important information that is not accounted for in the static connectome. In addition, omics such as transcriptomics or genotyping, as well as spatial and single cell techniques may offer granularity that goes beyond demographically-correlated signal, and would be a powerful tool to integrate with imaging.

Finally, we want to expand our research from focusing on healthy populations and developmental studies to focus on populations at risk of developing mental or cognitive illness. With the power of multimodal brain imaging and machine learning, we may be able to better diagnose such patients and increase the effectiveness of treatment.

# Bibliography

- [1] N K Logothetis, J Pauls, M Augath, T Trinath, and A Oeltermann. Neurophysiological investigation of the basis of the fMRI signal. *Nature*, 412(6843):150–157, July 2001.
- [2] J W Belliveau, D N Kennedy, Jr, R C McKinstry, B R Buchbinder, R M Weisskoff, M S Cohen, J M Vevea, T J Brady, and B R Rosen. Functional mapping of the human visual cortex by magnetic resonance imaging. *Science*, 254(5032):716–719, November 1991.
- [3] S Ogawa, T M Lee, A R Kay, and D W Tank. Brain magnetic resonance imaging with contrast dependent on blood oxygenation. *Proc. Natl. Acad. Sci. U. S. A.*, 87(24):9868–9872, December 1990.
- [4] Bingxin Zhao, Tengfei Li, Stephen M Smith, Di Xiong, Xifeng Wang, Yue Yang, Tianyou Luo, Ziliang Zhu, Yue Shan, Nana Matoba, Quan Sun, Yuchen Yang, Mads E Hauberg, Jaroslav Bendl, John F Fullard, Panagiotis Roussos, Weili Lin, Yun Li, Jason L Stein, and Hongtu Zhu. Common variants contribute to intrinsic human brain functional networks. *Nat. Genet.*, 54(4):508–517, April 2022.
- [5] Jonathan D Power, Alexander L Cohen, Steven M Nelson, Gagan S Wig, Kelly Anne Barnes, Jessica A Church, Alecia C Vogel, Timothy O Laumann, Fran M Miezin, Bradley L Schlaggar, and Steven E Petersen. Functional network organization of the human brain. *Neuron*, 72(4):665–678, November 2011.
- [6] Randy L Buckner, Jessica R Andrews-Hanna, and Daniel L Schacter. The brain’s default network: anatomy, function, and relevance to disease. *Ann. N. Y. Acad. Sci.*, 1124(1):1–38, March 2008.
- [7] Amir Joudaki, Niloufar Salehi, Mahdi Jalili, and Maria G Knyazeva. EEG-based functional brain networks: does the network size matter? *PLoS One*, 7(4):e35673, April 2012.
- [8] Yujin Zhang and Chaozhe Zhu. Assessing brain networks by resting-state dynamic functional connectivity: An fNIRS-EEG study. *Front. Neurosci.*, 13:1430, 2019.

- [9] Matti Hämäläinen, Riitta Hari, Risto J Ilmoniemi, Jukka Knuutila, and Olli V Lounasmaa. Magnetoencephalography—theory, instrumentation, and applications to noninvasive studies of the working human brain. *Rev. Mod. Phys.*, 65(2):413–497, April 1993.
- [10] Benson Mwangi, Tian Siva Tian, and Jair C Soares. A review of feature reduction techniques in neuroimaging. *Neuroinformatics*, 12(2):229–244, April 2014.
- [11] Katrin Amunts, Markus Axer, Swati Banerjee, Lise Bitsch, Jan G Bjaalie, Philipp Brauner, Andrea Brovelli, Navona Calarco, Marcel Carrere, Svenja Caspers, Christine J Charvet, Sven Cichon, Roshan Cools, Irene Constantini, Egidio Ugo D’Angelo, Giulia De Bonis, Gustavo Deco, Javier DeFelipe, Alain Destexhe, Timo Dickscheid, Markus Diesmann, Emrah Düzel, Simon B Eickhoff, Gaute Einevoll, Damian Eke, Andreas K Engel, Alan C Evans, Kathinka Evers, Nataliia Fedorchenko, Stephanie J Forkel, Jan Fousek, Angela D Friederici, Karl Friston, Stephen Furber, Liesbet Geris, Rainer Goebel, Onur Güntürkün, Aini Ismafairus Abd Hamid, Christina Herold, Claus C Hilgetag, Sabine M Höller, Yannis Ioannidis, Viktor Jirsa, Sriranga Kashyap, Burkhard S Kasper, Alban de Kerchove d’Exaerde, Roxana Kooijmans, István Koren, Jeanette Hellgren Kotaleski, Gregory Kiar, Wouter Klijn, Lars Klüver, Alois C Knoll, Zeljka Krsnik, Julia Kämpfer, Matthew E Larkum, Marja-Leena Linne, Thomas Lippert, Jafri Malin Abdullah, Paola Di Maio, Neville Magielse, Pierre Maquet, Anna Letizia Allegra Mascaro, Daniele Marinazzo, Jorge Mejias, Andreas Meyer-Lindenberg, Michele Migliore, Judith Michael, Yannick Morel, Fabrice O Morin, Lars Muckli, Guy Nagels, Lena Oden, Nicola Palomero-Gallagher, Fanis Panagiotaropoulos, Pier Stanislao Paolucci, Cyriel Pennartz, Liesbet M Peeters, Spase Petkoski, Nicolai Petkov, Lucy S Petro, Mihai A Petrovici, Giovanni Pezzulo, Pieter Roelfsema, Laurence Ris, Petra Ritter, Kathleen Rockland, Stefan Rotter, Andreas Rowald, Sabine Ruland, Philippe Ryvlin, Arleen Salles, Maria V Sanchez-Vives, Johannes Schemmel, Walter Senn, Alexandra A de Sousa, Felix Ströckens, Bertrand Thirion, Kâmil Uludağ, Simo Vanni, Sacha Jennifer van Albada, Wim Vanduffel, Julien Vezoli, Lisa Vincenz-Donnelly, Florian Walter, and Laszlo Zaborszky. The coming decade of digital brain research: A vision for neuroscience at the intersection of technology and computing. *Imaging Neuroscience*, 2:1–35, April 2024.
- [12] Hanh Vu, Hyun-Chul Kim, Minyoung Jung, and Jong-Hwan Lee. fMRI volume classification using a 3D convolutional neural network robust to shifted and scaled neuronal activations. *Neuroimage*, 223(117328):117328, December 2020.
- [13] Xiaoxiao Li, Yuan Zhou, Nicha Dvornek, Muhan Zhang, Siyuan Gao, Juntang Zhuang, Dustin Scheinost, Lawrence H Staib, Pamela Ventola, and James S Duncan. BrainGNN: Interpretable brain graph neural network for fMRI analysis. *Med. Image Anal.*, 74(102233):102233, December 2021.

- [14] Hasan A Bedel, Irmak Sivgin, Onat Dalmaz, Salman U H Dar, and Tolga Çukur. Bolt: Fused window transformers for fMRI time series analysis. *Med. Image Anal.*, 88(102841):102841, August 2023.
- [15] Yi Hao Chan, Conghao Wang, Wei Kwek Soh, and Jagath C Rajapakse. Combining neuroimaging and omics datasets for disease classification using graph neural networks. *Front. Neurosci.*, 16:866666, May 2022.
- [16] Clare Bycroft, Colin Freeman, Desislava Petkova, Gavin Band, Lloyd T Elliott, Kevin Sharp, Allan Motyer, Damjan Vukcevic, Olivier Delaneau, Jared O'Connell, Adrian Cortes, Samantha Welsh, Alan Young, Mark Effingham, Gil McVean, Stephen Leslie, Naomi Allen, Peter Donnelly, and Jonathan Marchini. The UK biobank resource with deep phenotyping and genomic data. *Nature*, 562(7726):203–209, October 2018.
- [17] D C Van Essen, K Ugurbil, E Auerbach, D Barch, T E J Behrens, R Bucholz, A Chang, L Chen, M Corbetta, S W Curtiss, S Della Penna, D Feinberg, M F Glasser, N Harel, A C Heath, L Larson-Prior, D Marcus, G Michalareas, S Moeller, R Oostenveld, S E Petersen, F Prior, B L Schlaggar, S M Smith, A Z Snyder, J Xu, E Yacoub, and WU-Minn HCP Consortium. The human connectome project: a data acquisition perspective. *Neuroimage*, 62(4):2222–2231, October 2012.
- [18] R C Petersen, P S Aisen, L A Beckett, M C Donohue, A C Gamst, D J Harvey, C R Jack, Jr, W J Jagust, L M Shaw, A W Toga, J Q Trojanowski, and M W Weiner. Alzheimer's disease neuroimaging initiative (ADNI): clinical characterization. *Neurology*, 74(3):201–209, January 2010.
- [19] Yves Frégnac and Gilles Laurent. Neuroscience: Where is the brain in the human brain project? *Nature*, 513(7516):27–29, September 2014.
- [20] Boaz Abramson, Job Boerma, and Aleh Tsivinski. Macroeconomics of mental health. Technical report, Cambridge, MA, April 2024.
- [21] GBD 2016 Neurology Collaborators. Global, regional, and national burden of neurological disorders, 1990–2016: a systematic analysis for the global burden of disease study 2016. *Lancet Neurol.*, 18(5):459–480, May 2019.
- [22] J Olesen, A Gustavsson, M Svensson, H-U Wittchen, B Jönsson, CDBE2010 study group, and European Brain Council. The economic cost of brain disorders in europe. *Eur. J. Neurol.*, 19(1):155–162, January 2012.
- [23] Peter R Millar, Brian A Gordon, Patrick H Luckett, Tammie L S Benzinger, Carlos Cruchaga, Anne M Fagan, Jason J Hassenstab, Richard J Perrin, Suzanne E Schindler, Ricardo F Allegri, Gregory S Day, Martin R Farlow, Hiroshi Mori, Georg Nübling, Dominantly Inherited Alzheimer Network, Randall J Bateman, John C Morris, and Beau M Ances. Multimodal brain age

estimates relate to alzheimer disease biomarkers and cognition in early stages: a cross-sectional observational study. *Elife*, 12, January 2023.

- [24] Elena Doering, Georgios Antonopoulos, Merle Hoenig, Thilo van Eimeren, Marcel Daamen, Henning Boecker, Frank Jessen, Emrah Düzel, Simon Eickhoff, Kaustubh Patil, Alexander Drzezga, and Alzheimer's Disease Neuroimaging Initiative and the DELCODE Study Group. MRI or 18F-FDG PET for brain age gap estimation: Links to cognition, pathology, and alzheimer disease progression. *J. Nucl. Med.*, 65(1):147–155, January 2024.
- [25] Bruce N Cuthbert and Thomas R Insel. Toward the future of psychiatric diagnosis: the seven pillars of RDoC. *BMC Med.*, 11(1):126, May 2013.
- [26] Thomas Insel. Spring 2013 inside nimh.
- [27] Ronald C Eldridge, Karan Uppal, Mahsa Shokouhi, M Ryan Smith, Xin Hu, Zhaohui S Qin, Dean P Jones, and Ihab Hajjar. Multiomics analysis of structural magnetic resonance imaging of the brain and cerebrospinal fluid metabolomics in cognitively normal and impaired adults. *Front. Aging Neurosci.*, 13:796067, 2021.
- [28] Gyoergy Buzsaki. *The brain from inside out the brain from inside out*. Oxford University Press, Cary, NC, June 2019.
- [29] Murat Yücel, Erin Oldenhof, Serge H Ahmed, David Belin, Joel Billieux, Henrietta Bowden-Jones, Adrian Carter, Samuel R Chamberlain, Luke Clark, Jason Connor, Mark Daglish, Geert Dom, Pinhas Dannon, Theodora Duka, Maria Jose Fernandez-Serrano, Matt Field, Ingmar Franken, Rita Z Goldstein, Raul Gonzalez, Anna E Goudriaan, Jon E Grant, Matthew J Gullo, Robert Hester, David C Hodgins, Bernard Le Foll, Rico S C Lee, Anne Lingford-Hughes, Valentina Lorenzetti, Scott J Moeller, Marcus R Munafò, Brian Odlaug, Marc N Potenza, Rebecca Segrave, Zsuzsika Sjoerds, Nadia Solowij, Wim van den Brink, Ruth J van Holst, Valerie Voon, Reinout Wiers, Leonardo F Fontenelle, and Antonio Verdejo-Garcia. A transdiagnostic dimensional approach towards a neuropsychological assessment for addiction: an international delphi consensus study. *Addiction*, 114(6):1095–1109, June 2019.
- [30] Julian Nowogrodzki. The world's strongest MRI machines are pushing human imaging to new limits. *Nature*, 563(7729):24–26, November 2018.
- [31] Darren Hudson and Luis Abrantes. Heattech clothing technology and potential for thermal injury in MRI. *BJR Case Rep.*, 9(1):20220012, February 2023.
- [32] David A Feinberg, Alexander J S Beckett, An T Vu, Jason Stockmann, Laurentius Huber, Samantha Ma, Sinyeob Ahn, Kawin Setsompop, Xiaozhi Cao, Suhyung Park, Chunlei Liu, Lawrence L Wald, Jonathan R Polimeni, Azma Mareyam, Bernhard Gruber, Rüdiger Stirnberg, Congyu Liao, Essa Yacoub,

- Mathias Davids, Paul Bell, Elmar Rummert, Michael Koehler, Andreas Potthast, Ignacio Gonzalez-Insua, Stefan Stocker, Shajan Gunamony, and Peter Dietz. Next-generation MRI scanner designed for ultra-high-resolution human brain imaging at 7 tesla. *Nat. Methods*, 20(12):2048–2057, December 2023.
- [33] Gary H Glover. Overview of functional magnetic resonance imaging. *Neurosurg. Clin. N. Am.*, 22(2):133–9, vii, April 2011.
  - [34] Arjan D Hendriks, Federico D’Agata, Luisa Raimondo, Tim Schakel, Liesbeth Geerts, Peter R Luijten, Dennis W J Klomp, and Natalia Petridou. Pushing functional MRI spatial and temporal resolution further: High-density receive arrays combined with shot-selective 2D CAIPIRINHA for 3D echo-planar imaging at 7 T. *NMR Biomed.*, 33(5):e4281, May 2020.
  - [35] E Bustamante and P L Pedersen. High aerobic glycolysis of rat hepatoma cells in culture: role of mitochondrial hexokinase. *Proc. Natl. Acad. Sci. U. S. A.*, 74(9):3735–3739, September 1977.
  - [36] Keshav Anand and Marwan Sabbagh. Amyloid imaging: Poised for integration into medical practice. *Neurotherapeutics*, 14(1):54–61, January 2017.
  - [37] Guobao Wang. High temporal-resolution dynamic PET image reconstruction using a new spatiotemporal kernel method. *IEEE Trans. Med. Imaging*, 38(3):664–674, March 2019.
  - [38] William W Moses. Fundamental limits of spatial resolution in PET. *Nucl. Instrum. Methods Phys. Res. A*, 648 Supplement 1:S236–S240, August 2011.
  - [39] H J Wittsack, A M Wohlschläger, E K Ritzl, R Kleiser, M Cohnen, R J Seitz, and U Mödder. CT-perfusion imaging of the human brain: advanced deconvolution analysis using circulant singular value decomposition. *Comput. Med. Imaging Graph.*, 32(1):67–77, January 2008.
  - [40] Eugene Lin and Adam Alessio. What are the basic concepts of temporal, contrast, and spatial resolution in cardiac CT? *J. Cardiovasc. Comput. Tomogr.*, 3(6):403–408, November 2009.
  - [41] I Frank Ciernik, Elena Dizendorf, Brigitta G Baumert, Beatrice Reiner, Cyrill Burger, J Bernard Davis, Urs M Lütfolf, Hans C Steinert, and Gustav K Von Schulthess. Radiation treatment planning with an integrated positron emission and computer tomography (PET/CT): a feasibility study. *Int. J. Radiat. Oncol. Biol. Phys.*, 57(3):853–863, November 2003.
  - [42] Polad M Shikhaliev, Tong Xu, and Sabee Molloii. Photon counting computed tomography: concept and initial results. *Med. Phys.*, 32(2):427–436, February 2005.
  - [43] L F Haas. Hans berger (1873-1941), richard caton (1842-1926), and electroencephalography. *J. Neurol. Neurosurg. Psychiatry*, 74(1):9, January 2003.

- [44] Appaji Rayi. *Electroencephalogram*, Oct 2022.
- [45] Ray Cooper, A L Winter, H J Crow, and W Grey Walter. Comparison of subcortical, cortical and scalp activity using chronically indwelling electrodes in man. *Electroencephalogr. Clin. Neurophysiol.*, 18(3):217–228, February 1965.
- [46] Chetan S. Nayak. *Eeg normal waveforms*, Jul 2023.
- [47] Tracy Warbrick. Simultaneous EEG-fMRI: What have we learned and what does the future hold? *Sensors (Basel)*, 22(6):2262, March 2022.
- [48] Matti Hämäläinen, Riitta Hari, Risto J Ilmoniemi, Jukka Knuutila, and Olli V Lounasmaa. Magnetoencephalography—theory, instrumentation, and applications to noninvasive studies of the working human brain. *Rev. Mod. Phys.*, 65(2):413–497, April 1993.
- [49] Steven M Stufflebeam, Naoaki Tanaka, and Seppo P Ahlfors. Clinical applications of magnetoencephalography. *Hum. Brain Mapp.*, 30(6):1813–1823, June 2009.
- [50] T H Sander, J Preusser, R Mhaskar, J Kitching, L Trahms, and S Knappe. Magnetoencephalography with a chip-scale atomic magnetometer. *Biomed. Opt. Express*, 3(5):981–990, May 2012.
- [51] Elena Boto, Niall Holmes, James Leggett, Gillian Roberts, Vishal Shah, Sofie S Meyer, Leonardo Duque Muñoz, Karen J Mullinger, Tim M Tierney, Sven Bestmann, Gareth R Barnes, Richard Bowtell, and Matthew J Brookes. Moving magnetoencephalography towards real-world applications with a wearable system. *Nature*, 555(7698):657–661, March 2018.
- [52] Marco Ferrari and Valentina Quaresima. A brief review on the history of human functional near-infrared spectroscopy (fNIRS) development and fields of application. *Neuroimage*, 63(2):921–935, November 2012.
- [53] Xu Cui, Signe Bray, Daniel M Bryant, Gary H Glover, and Allan L Reiss. A quantitative comparison of NIRS and fMRI across multiple cognitive tasks. *Neuroimage*, 54(4):2808–2821, February 2011.
- [54] Ting Li, Hui Gong, and Qingming Luo. Visualization of light propagation in visible chinese human head for functional near-infrared spectroscopy. *J. Biomed. Opt.*, 16(4):045001, April 2011.
- [55] Satoru Kohno, Ichiro Miyai, Akitoshi Seiyama, Ichiro Oda, Akihiro Ishikawa, Shoichi Tsuneishi, Takashi Amita, and Koji Shimizu. Removal of the skin blood flow artifact in functional near-infrared spectroscopic imaging data through independent component analysis. *J. Biomed. Opt.*, 12(6):062111, November 2007.

- [56] G T Marth, I Korf, M D Yandell, R T Yeh, Z Gu, H Zakeri, N O Stitzel, L Hillier, P Y Kwok, and W R Gish. A general approach to single-nucleotide polymorphism discovery. *Nat. Genet.*, 23(4):452–456, December 1999.
- [57] Kevin J Gleason, Fan Yang, Brandon L Pierce, Xin He, and Lin S Chen. Primo: integration of multiple GWAS and omics QTL summary statistics for elucidation of molecular mechanisms of trait-associated SNPs and detection of pleiotropy in complex traits. *Genome Biol.*, 21(1):236, September 2020.
- [58] Katharina Schwarze, James Buchanan, Jilles M Fermont, Helene Dreau, Mark W Tilley, John M Taylor, Pavlos Antoniou, Samantha J L Knight, Carme Camps, Melissa M Pentony, Erika M Kvikstad, Steve Harris, Niko Popitsch, Alastair T Pagnamenta, Anna Schuh, Jenny C Taylor, and Sarah Wordsworth. The complete costs of genome sequencing: a microcosting study in cancer and rare diseases from a single center in the united kingdom. *Genet. Med.*, 22(1):85–94, January 2020.
- [59] Joseph T Glessner, Muredach P Reilly, Cecilia E Kim, Nagahide Takahashi, Anthony Albano, Cuiping Hou, Jonathan P Bradfield, Haitao Zhang, Patrick M A Sleiman, James H Flory, Marcin Imielinski, Edward C Frackelton, Rosetta Chiavacci, Kelly A Thomas, Maria Garris, Frederick G Otieno, Michael Davidson, Mark Weiser, Abraham Reichenberg, Kenneth L Davis, Joseph I Friedman, Thomas P Cappola, Kenneth B Margulies, Daniel J Rader, Struan F A Grant, Joseph D Buxbaum, Raquel E Gur, and Hakon Hakonarson. Strong synaptic transmission impact by copy number variations in schizophrenia. *Proc. Natl. Acad. Sci. U. S. A.*, 107(23):10584–10589, June 2010.
- [60] Theodore D Satterthwaite, Mark A Elliott, Kosha Ruparel, James Loughead, Karthik Prabhakaran, Monica E Calkins, Ryan Hopson, Chad Jackson, Jack Keefe, Marisa Riley, Frank D Mentch, Patrick Sleiman, Ragini Verma, Christos Davatzikos, Hakon Hakonarson, Ruben C Gur, and Raquel E Gur. Neuroimaging of the philadelphia neurodevelopmental cohort. *Neuroimage*, 86:544–553, February 2014.
- [61] Juan Fortea, Jordi Pegueroles, Daniel Alcolea, Olivia Belbin, Oriol Dols-Icardo, Lídia Vaqué-Alcázar, Laura Videla, Juan Domingo Gispert, Marc Suárez-Calvet, Sterling C Johnson, Reisa Sperling, Alexandre Bejanin, Alberto Lleó, and Víctor Montal. APOE4 homozygosity represents a distinct genetic form of alzheimer’s disease. *Nat. Med.*, 30(5):1284–1291, May 2024.
- [62] Khalid Iqbal and Inge Grundke-Iqbali. Alzheimer’s disease, a multifactorial disorder seeking multitherapies. *Alzheimers. Dement.*, 6(5):420–424, September 2010.
- [63] Simona Corina Trifu, Bianca Kohn, Andrei Vlasie, and Bogdan-Eduard Patrichi. Genetics of schizophrenia (review). *Exp. Ther. Med.*, 20(4):3462–3468, October 2020.

- [64] S Hong Lee, The Schizophrenia Psychiatric Genome-Wide Association Study Consortium (PGC-SCZ), Teresa R DeCandia, Stephan Ripke, Jian Yang, Patrick F Sullivan, Michael E Goddard, Matthew C Keller, Peter M Visscher, Naomi R Wray, The International Schizophrenia Consortium (ISC), and The Molecular Genetics of Schizophrenia Collaboration (MGS). Estimating the proportion of variation in susceptibility to schizophrenia captured by common SNPs. *Nat. Genet.*, 44(3):247–250, March 2012.
- [65] Patrick Friedrich, Stephanie J Forkel, Céline Amiez, Joshua H Balsters, Olivier Coulon, Lingzhong Fan, Alexandros Goulas, Fadila Hadj-Bouziane, Erin E Hecht, Katja Heuer, Tianzi Jiang, Robert D Latzman, Xiaojin Liu, Kep Kee Loh, Kaustubh R Patil, Alizée Lopez-Persem, Emmanuel Procyk, Jerome Sallet, Roberto Toro, Sam Vickery, Susanne Weis, Charles R E Wilson, Ting Xu, Valerio Zerbi, Simon B Eickhoff, Daniel S Margulies, Rogier B Mars, and Michel Thiebaut de Schotten. Imaging evolution of the primate brain: the next frontier? *Neuroimage*, 228(117685):117685, March 2021.
- [66] Honghui Yang, Jingyu Liu, Jing Sui, Godfrey Pearlson, and Vince D Calhoun. A hybrid machine learning method for fusing fMRI and genetic data: Combining both improves classification of schizophrenia. *Front. Hum. Neurosci.*, 4:192, October 2010.
- [67] Jinhua Sheng, Yu Xin, Qiao Zhang, Luyun Wang, Ze Yang, and Jie Yin. Predictive classification of alzheimer’s disease using brain imaging and genetic data. *Sci. Rep.*, 12(1):2405, February 2022.
- [68] Li Shen and Paul M Thompson. Brain imaging genomics: Integrated analysis and machine learning. *Proc. IEEE Inst. Electr. Electron. Eng.*, 108(1):125–162, January 2020.
- [69] Dongdong Lin, Vince D Calhoun, and Yu-Ping Wang. Correspondence between fMRI and SNP data by group sparse canonical correlation analysis. *Med. Image Anal.*, 18(6):891–902, August 2014.
- [70] Martin J McKeown, Lars Kai Hansen, and Terrence J Sejnowski. Independent component analysis of functional MRI: what is signal and what is noise? *Curr. Opin. Neurobiol.*, 13(5):620–629, October 2003.
- [71] Jingyu Liu, Godfrey Pearlson, Andreas Windemuth, Gualberto Ruano, Nora I Perrone-Bizzozero, and Vince Calhoun. Combining fMRI and SNP data to investigate connections between brain function and genetics using parallel ICA. *Hum. Brain Mapp.*, 30(1):241–255, January 2009.
- [72] Javad Ansarifar, Iliana I. Karipidis, Manish Saggar, and David S. Hong. BIG-graph: Brain imaging genetics by graph neural network, 2023.

- [73] Yi Hao Chan, Conghao Wang, Wei Kwek Soh, and Jagath C Rajapakse. Combining neuroimaging and omics datasets for disease classification using graph neural networks. *Front. Neurosci.*, 16:866666, May 2022.
- [74] Xiao-Meng Zhang, Li Liang, Lin Liu, and Ming-Jing Tang. Graph neural networks and their current applications in bioinformatics. *Front. Genet.*, 12:690049, July 2021.
- [75] Dana Mackenzie. How animals follow their nose. *Knowable Mag.*, March 2023.
- [76] P J Basser, S Pajevic, C Pierpaoli, J Duda, and A Aldroubi. In vivo fiber tractography using DT-MRI data. *Magn. Reson. Med.*, 44(4):625–632, October 2000.
- [77] Guglielmo Manenti, Marco Cariani, Stefano Mancino, Vittorio Colangelo, Mauro Di Roma, Ettore Squillaci, and Giovanni Simonetti. Diffusion tensor magnetic resonance imaging of prostate cancer. *Invest. Radiol.*, 42(6):412–419, June 2007.
- [78] Michal Bernstein-Eliav and Ido Tavor. The prediction of brain activity from connectivity: Advances and applications. *Neuroscientist*, 30(3):367–377, June 2024.
- [79] B B Biswal, J Van Kylen, and J S Hyde. Simultaneous assessment of flow and BOLD signals in resting-state functional connectivity maps. *NMR Biomed.*, 10(4-5):165–170, June 1997.
- [80] Stephen M Smith. The future of fMRI connectivity. *Neuroimage*, 62(2):1257–1266, August 2012.
- [81] Wenxing Hu, Biao Cai, Aiying Zhang, Vince D Calhoun, and Yu-Ping Wang. Deep collaborative learning with application to the study of multimodal brain development. *IEEE Trans. Biomed. Eng.*, 66(12):3346–3359, December 2019.
- [82] Chao Zhang, Chase C Dougherty, Stefi A Baum, Tonya White, and Andrew M Michael. Functional connectivity predicts gender: Evidence for gender differences in resting brain connectivity. *Hum. Brain Mapp.*, 39(4):1765–1776, April 2018.
- [83] Anton Orlichenko, Grant Daly, Ziyu Zhou, Anqi Liu, Hui Shen, Hong-Wen Deng, and Yu-Ping Wang. ImageNomer: Description of a functional connectivity and omics analysis tool and case study identifying a race confound. *Neuroimage Rep.*, 3(4):100191, December 2023.
- [84] Xiaotong Du, Xiaotong Wei, Hao Ding, Ying Yu, Yingying Xie, Yi Ji, Yu Zhang, Chao Chai, Meng Liang, Jie Li, Chuanjun Zhuo, Chunshui Yu, and Wen Qin. Unraveling schizophrenia replicable functional connectivity disruption patterns across sites. *Hum. Brain Mapp.*, 44(1):156–169, January 2023.

- [85] Wenjin Zou, Peilun Song, Weicong Lu, Robin Shao, Ruoxi Zhang, Suk-Yu Yau, Ti-Fei Yuan, Yaping Wang, and Kangguang Lin. Global hippocampus functional connectivity as a predictive neural marker for conversion to future mood disorder in unaffected offspring of bipolar disorder parents. *Asian J. Psychiatr.*, 78(103307):103307, December 2022.
- [86] Xueling Suo, Du Lei, Wenbin Li, Jing Yang, Lingjiang Li, John A Sweeney, and Qiyong Gong. Individualized prediction of PTSD symptom severity in trauma survivors from whole-brain resting-state functional connectivity. *Front. Behav. Neurosci.*, 14:563152, December 2020.
- [87] Madhura Ingalkar, Sumeet Shinde, Arnav Karmarkar, Archith Rajan, D Rangaprakash, and Gopikrishna Deshpande. Functional connectivity-based prediction of autism on site harmonized ABIDE dataset. *IEEE Trans. Biomed. Eng.*, 68(12):3628–3637, December 2021.
- [88] Lin Hua, Fei Gao, Xiaoluan Xia, Qiwei Guo, Yonghua Zhao, Shaohui Huang, and Zhen Yuan. Individual-specific functional connectivity improves prediction of alzheimer’s disease’s symptoms in elderly people regardless of APOE  $\epsilon 4$  genotype. *Commun. Biol.*, 6(1):581, May 2023.
- [89] Dafa Shi, Haoran Zhang, Guangsong Wang, Siyuan Wang, Xiang Yao, Yanfei Li, Qiu Guo, Shuang Zheng, and Ke Ren. Machine learning for detecting parkinson’s disease by resting-state functional magnetic resonance imaging: A multicenter radiomics analysis. *Front. Aging Neurosci.*, 14:806828, March 2022.
- [90] Bo-Yong Park, Kyoungseob Byeon, Mi Ji Lee, Chin-Sang Chung, Se-Hong Kim, Filip Morys, Boris Bernhardt, Alain Dagher, and Hyunjin Park. Whole-brain functional connectivity correlates of obesity phenotypes. *Hum. Brain Mapp.*, 41(17):4912–4924, December 2020.
- [91] J Mazziotta, A Toga, A Evans, P Fox, J Lancaster, K Zilles, R Woods, T Paus, G Simpson, B Pike, C Holmes, L Collins, P Thompson, D MacDonald, M Iacoboni, T Schormann, K Amunts, N Palomero-Gallagher, S Geyer, L Parsons, K Narr, N Kabani, G Le Goualher, D Boomsma, T Cannon, R Kawashima, and B Mazoyer. A probabilistic atlas and reference system for the human brain: International consortium for brain mapping (ICBM). *Philos. Trans. R. Soc. Lond. B Biol. Sci.*, 356(1412):1293–1322, August 2001.
- [92] Pravat K Mandal, Rashima Mahajan, and Ivo D Dinov. Structural brain atlases: design, rationale, and applications in normal and pathological cohorts. *J. Alzheimers. Dis.*, 31 Suppl 3(s3):S169–88, 2012.
- [93] Mark Jenkinson, Christian F Beckmann, Timothy E J Behrens, Mark W Woolrich, and Stephen M Smith. FSL. *Neuroimage*, 62(2):782–790, August 2012.

- [94] Edmund T Rolls, Chu-Chung Huang, Ching-Po Lin, Jianfeng Feng, and Marc Joliot. Automated anatomical labelling atlas 3. *Neuroimage*, 206(116189):116189, February 2020.
- [95] Matthew F Glasser, Timothy S Coalson, Emma C Robinson, Carl D Hacker, John Harwell, Essa Yacoub, Kamil Ugurbil, Jesper Andersson, Christian F Beckmann, Mark Jenkinson, Stephen M Smith, and David C Van Essen. A multi-modal parcellation of human cerebral cortex. *Nature*, 536(7615):171–178, August 2016.
- [96] X Shen, F Tokoglu, X Papademetris, and R T Constable. Groupwise whole-brain parcellation from resting-state fMRI data for network node identification. *Neuroimage*, 82:403–415, November 2013.
- [97] Lingzhong Fan, Hai Li, Junjie Zhuo, Yu Zhang, Jiaojian Wang, Liangfu Chen, Zhengyi Yang, Congying Chu, Sangma Xie, Angela R Laird, Peter T Fox, Simon B Eickhoff, Chunshui Yu, and Tianzi Jiang. The human brainnetome atlas: A new brain atlas based on connectional architecture. *Cereb. Cortex*, 26(8):3508–3526, August 2016.
- [98] Edgar A DeYoe and Ryan V Raut. Visual mapping using blood oxygen level dependent functional magnetic resonance imaging. *Neuroimaging Clin. N. Am.*, 24(4):573–584, November 2014.
- [99] Stefan Kemeny, Frank Q Ye, Rasmus Birn, and Allen R Braun. Comparison of continuous overt speech fMRI using BOLD and arterial spin labeling. *Hum. Brain Mapp.*, 24(3):173–183, March 2005.
- [100] Simone Grimm, Peter Boesiger, Johannes Beck, Daniel Schuepbach, Felix Bermpohl, Martin Walter, Jutta Ernst, Daniel Hell, Heinz Boeker, and Georg Northoff. Altered negative BOLD responses in the default-mode network during emotion processing in depressed subjects. *Neuropsychopharmacology*, 34(4):932–943, March 2009.
- [101] Klaas Enno Stephan and Karl J Friston. Analyzing effective connectivity with functional magnetic resonance imaging. *Wiley Interdiscip. Rev. Cogn. Sci.*, 1(3):446–459, May 2010.
- [102] K J Friston, Katrin H Preller, Chris Mathys, Hayriye Cagnan, Jakob Heinze, Adeel Razi, and Peter Zeidman. Dynamic causal modelling revisited. *Neuroimage*, 199:730–744, October 2019.
- [103] Denes Szucs and John Pa Ioannidis. Sample size evolution in neuroimaging research: An evaluation of highly-cited studies (1990-2012) and of latest practices (2017-2018) in high-impact journals. *Neuroimage*, 221(117164):117164, November 2020.

- [104] Visar Berisha, Chelsea Krantsevich, P Richard Hahn, Shira Hahn, Gautam Dasarathy, Pavan Turaga, and Julie Liss. Digital medicine and the curse of dimensionality. *NPJ Digit. Med.*, 4(1):153, October 2021.
- [105] Philip Sayegh, Alyssa Arentoft, Nicholas S Thaler, Andy C Dean, and April D Thames. Quality of education predicts performance on the wide range achievement test-4th edition word reading subtest. *Arch. Clin. Neuropsychol.*, 29(8):731–736, December 2014.
- [106] D C Van Essen, K Ugurbil, E Auerbach, D Barch, T E J Behrens, R Bucholz, A Chang, L Chen, M Corbetta, S W Curtiss, S Della Penna, D Feinberg, M F Glasser, N Harel, A C Heath, L Larson-Prior, D Marcus, G Michalareas, S Moeller, R Oostenveld, S E Petersen, F Prior, B L Schlaggar, S M Smith, A Z Snyder, J Xu, E Yacoub, and WU-Minn HCP Consortium. The human connectome project: a data acquisition perspective. *Neuroimage*, 62(4):2222–2231, October 2012.
- [107] Mikhail Milchenko and Daniel Marcus. Obscuring surface anatomy in volumetric imaging data. *Neuroinformatics*, 11(1):65–75, January 2013.
- [108] Carol A Tamminga, Godfrey Pearlson, Matcheri Keshavan, John Sweeney, Brett Clementz, and Gunvant Thaker. Bipolar and schizophrenia network for intermediate phenotypes: outcomes across the psychosis continuum. *Schizophr. Bull.*, 40 Suppl 2(Suppl 2):S131–7, March 2014.
- [109] Sebastian Urchs, Christian Dansereau, Yassine Benhajali, and Pierre Bellec. Group multiscale functional template generated with BASC on the cambridge sample, January 2015.
- [110] C J Aine, H J Bockholt, J R Bustillo, J M Cañive, A Caprihan, C Gasparovic, F M Hanlon, J M Houck, R E Jung, J Lauriello, J Liu, A R Mayer, N I Perrone-Bizzozero, S Posse, J M Stephen, J A Turner, V P Clark, and Vince D Calhoun. Multimodal neuroimaging in schizophrenia: Description and dissemination. *Neuroinformatics*, 15(4):343–364, October 2017.
- [111] J M Stephen, I Solis, J Janowich, M Stern, M R Frenzel, J A Eastman, M S Mills, C M Embury, N M Coolidge, E Heinrichs-Graham, A Mayer, J Liu, Y P Wang, T W Wilson, and V D Calhoun. The developmental Chronnecto-Genomics (Dev-CoG) study: A multimodal study on the developing brain. *Neuroimage*, 225(117438):117438, January 2021.
- [112] I S Kiselev, O G Kulakova, A N Boyko, and O O Favorova. DNA methylation as an epigenetic mechanism in the development of multiple sclerosis. *Acta Naturae*, 13(2):45–57, April 2021.
- [113] A Di Martino, C-G Yan, Q Li, E Denio, F X Castellanos, K Alaerts, J S Anderson, M Assaf, S Y Bookheimer, M Dapretto, B Deen, S Delmonte, I Dinstein, B Ertl-Wagner, D A Fair, L Gallagher, D P Kennedy, C L Keown, C Keysers,

- J E Lainhart, C Lord, B Luna, V Menon, N J Minshew, C S Monk, S Mueller, R-A Müller, M B Nebel, J T Nigg, K O’Hearn, K A Pelphrey, S J Peltier, J D Rudie, S Sunaert, M Thioux, J M Tyszka, L Q Uddin, J S Verhoeven, N Wenderoth, J L Wiggins, S H Mostofsky, and M P Milham. The autism brain imaging data exchange: towards a large-scale evaluation of the intrinsic brain architecture in autism. *Mol. Psychiatry*, 19(6):659–667, June 2014.
- [114] Adriana Di Martino, David O’Connor, Bosi Chen, Kaat Alaerts, Jeffrey S Anderson, Michal Assaf, Joshua H Balsters, Leslie Baxter, Anita Beggiato, Sylvie Bernaerts, Laura M E Blanken, Susan Y Bookheimer, B Blair Braden, Lisa Byrge, F Xavier Castellanos, Mirella Dapretto, Richard Delorme, Damien A Fair, Inna Fishman, Jacqueline Fitzgerald, Louise Gallagher, R Joanne Jao Keehn, Daniel P Kennedy, Janet E Lainhart, Beatriz Luna, Stewart H Mostofsky, Ralph-Axel Müller, Mary Beth Nebel, Joel T Nigg, Kirsten O’Hearn, Marjorie Solomon, Roberto Toro, Chandan J Vaidya, Nicole Wenderoth, Tonya White, R Cameron Craddock, Catherine Lord, Bennett Leventhal, and Michael P Milham. Enhancing studies of the connectome in autism using the autism brain imaging data exchange II. *Sci. Data*, 4(1):170010, March 2017.
  - [115] R C Petersen, P S Aisen, L A Beckett, M C Donohue, A C Gamst, D J Harvey, C R Jack, Jr, W J Jagust, L M Shaw, A W Toga, J Q Trojanowski, and M W Weiner. Alzheimer’s disease neuroimaging initiative (ADNI): clinical characterization. *Neurology*, 74(3):201–209, January 2010.
  - [116] Elaheh Moradi, Antonietta Pepe, Christian Gaser, Heikki Huttunen, Jussi Tohka, and Alzheimer’s Disease Neuroimaging Initiative. Machine learning framework for early MRI-based alzheimer’s conversion prediction in MCI subjects. *Neuroimage*, 104:398–412, January 2015.
  - [117] Zhi Chen, Yongguo Liu, Yun Zhang, Qiaoqin Li, and Alzheimer’s Disease Neuroimaging Initiative. Orthogonal latent space learning with feature weighting and graph learning for multimodal alzheimer’s disease diagnosis. *Med. Image Anal.*, 84(102698):102698, February 2023.
  - [118] Natalie M Saragosa-Harris, Natasha Chaku, Niamh MacSweeney, Victoria Guazzelli Williamson, Maximilian Scheuplein, Brandee Feola, Carlos Cardenas-Iniguez, Ece Demir-Lira, Elizabeth A McNeilly, Landry Goodgame Huffman, Lucy Whitmore, Kalina J Michalska, Katherine Sf Damme, Divyangana Rakesh, and Kathryn L Mills. A practical guide for researchers and reviewers using the ABCD study and other large longitudinal datasets. *Dev. Cogn. Neurosci.*, 55(101115):101115, June 2022.
  - [119] H Garavan, H Bartsch, K Conway, A Decastro, R Z Goldstein, S Heeringa, T Jernigan, A Potter, W Thompson, and D Zahs. Recruiting the ABCD sample: Design considerations and procedures. *Dev. Cogn. Neurosci.*, 32:16–22, August 2018.

- [120] Cathie Sudlow, John Gallacher, Naomi Allen, Valerie Beral, Paul Burton, John Danesh, Paul Downey, Paul Elliott, Jane Green, Martin Landray, Bette Liu, Paul Matthews, Giok Ong, Jill Pell, Alan Silman, Alan Young, Tim Sprosen, Tim Peakman, and Rory Collins. UK biobank: an open access resource for identifying the causes of a wide range of complex diseases of middle and old age. *PLoS Med.*, 12(3):e1001779, March 2015.
- [121] Anton Orlichenko, Kuan-Jui Su, Hui Shen, Hong-Wen Deng, and Yu-Ping Wang. Somatomotor-visual resting state functional connectivity increases after 2 years in the UK biobank longitudinal cohort. *J. Med. Imaging (Bellingham)*, 11(2):024010, March 2024.
- [122] Michael Allwright, Hamish D Mundell, Andrew N McCorkindale, Richard I Lindley, Paul J Austin, Boris Guennewig, and Greg T Sutherland. Ranking the risk factors for alzheimer's disease; findings from the UK biobank study. *Aging Brain*, 3(100081):100081, June 2023.
- [123] Koene R A Van Dijk, Mert R Sabuncu, and Randy L Buckner. The influence of head motion on intrinsic functional connectivity MRI. *Neuroimage*, 59(1):431–438, January 2012.
- [124] Theodore D Satterthwaite, Daniel H Wolf, James Loughead, Kosha Ruparel, Mark A Elliott, Hakon Hakonarson, Ruben C Gur, and Raquel E Gur. Impact of in-scanner head motion on multiple measures of functional connectivity: relevance for studies of neurodevelopment in youth. *Neuroimage*, 60(1):623–632, March 2012.
- [125] R K Niazy, C F Beckmann, G D Iannetti, J M Brady, and S M Smith. Removal of fMRI environment artifacts from EEG data using optimal basis sets. *Neuroimage*, 28(3):720–737, November 2005.
- [126] Carolina Makowski, Martin Lepage, and Alan C Evans. Head motion: the dirty little secret of neuroimaging in psychiatry. *J. Psychiatry Neurosci.*, 43(5):180022, August 2018.
- [127] S Thesen, O Heid, E Mueller, and L R Schad. Prospective acquisition correction for head motion with image-based tracking for real-time fMRI. *Magn. Reson. Med.*, 44(3):457–465, September 2000.
- [128] Hans-Peter Müller, Anna Behler, G Bernhard Landwehrmeyer, Hans-Jürgen Huppertz, and Jan Kassubek. How to arrange follow-up time-intervals for longitudinal brain MRI studies in neurodegenerative diseases. *Front. Neurosci.*, 15:682812, July 2021.
- [129] Edward Joseph Caruana, Marius Roman, Jules Hernández-Sánchez, and Piergiorgio Solli. Longitudinal studies. *J. Thorac. Dis.*, 7(11):E537–40, November 2015.

- [130] Richard McClatchey, Andrew Branson, Ashiq Anjum, Peter Bloodsworth, Irfan Habib, Kamran Munir, Jetendr Shamsdasani, Kamran Soomro, and neuGRID Consortium. Providing traceability for neuroimaging analyses. *Int. J. Med. Inform.*, 82(9):882–894, September 2013.
- [131] Jean-Baptiste Poline, Janis L Breeze, Satrajit Ghosh, Krzysztof Gorgolewski, Yaroslav O Halchenko, Michael Hanke, Christian Haselgrove, Karl G Helmer, David B Keator, Daniel S Marcus, Russell A Poldrack, Yannick Schwartz, John Ashburner, and David N Kennedy. Data sharing in neuroimaging research. *Front. Neuroinform.*, 6, 2012.
- [132] Tarek Sherif, Pierre Rioux, Marc-Etienne Rousseau, Nicolas Kassis, Natacha Beck, Reza Adalat, Samir Das, Tristan Glatard, and Alan C Evans. CBRAIN: a web-based, distributed computing platform for collaborative neuroimaging research. *Front. Neuroinform.*, 8:54, May 2014.
- [133] Jessica A Turner, Vince D Calhoun, Paul M Thompson, Neda Jahanshad, Christopher R K Ching, Sophia I Thomopoulos, Eric Verner, Gregory P Strauss, Anthony O Ahmed, Matthew D Turner, Sunitha Basodi, Judith M Ford, Daniel H Mathalon, Adrian Preda, Aysenil Belger, Bryon A Mueller, Kelvin O Lim, and Theo G M van Erp. ENIGMA + COINSTAC: Improving findability, accessibility, interoperability, and re-usability. *Neuroinformatics*, 20(1):261–275, January 2022.
- [134] Benjamin O Turner, Erick J Paul, Michael B Miller, and Aron K Barbey. Small sample sizes reduce the replicability of task-based fMRI studies. *Commun. Biol.*, 1(1):62, June 2018.
- [135] Eva Breznik, Filip Malmberg, Joel Kullberg, Håkan Ahlström, and Robin Strand. Multiple comparison correction methods for whole-body magnetic resonance imaging. *J. Med. Imaging (Bellingham)*, 7(1):014005, January 2020.
- [136] Shruti Atul Mali, Abdalla Ibrahim, Henry C Woodruff, Vincent Andreadczyk, Henning Müller, Sergey Primakov, Zohaib Salahuddin, Avishek Chatterjee, and Philippe Lambin. Making radiomics more reproducible across scanner and imaging protocol variations: A review of harmonization methods. *J. Pers. Med.*, 11(9):842, August 2021.
- [137] Jean-Philippe Fortin, Drew Parker, Birkan Tunç, Takanori Watanabe, Mark A Elliott, Kosha Ruparel, David R Roalf, Theodore D Satterthwaite, Ruben C Gur, Raquel E Gur, Robert T Schultz, Ragini Verma, and Russell T Shino-hara. Harmonization of multi-site diffusion tensor imaging data. *Neuroimage*, 161:149–170, November 2017.
- [138] Lukas Snoek, Steven Milić, and H Steven Scholte. How to control for confounds in decoding analyses of neuroimaging data. *Neuroimage*, 184:741–760, January 2019.

- [139] Meichen Yu, Kristin A Linn, Philip A Cook, Mary L Phillips, Melvin McInnis, Maurizio Fava, Madhukar H Trivedi, Myrna M Weissman, Russell T Shinohara, and Yvette I Sheline. Statistical harmonization corrects site effects in functional connectivity measurements from multi-site fMRI data. *Hum. Brain Mapp.*, 39(11):4213–4227, November 2018.
- [140] David D Cox and Robert L Savoy. Functional magnetic resonance imaging (fMRI) “brain reading”: detecting and classifying distributed patterns of fMRI activity in human visual cortex. *Neuroimage*, 19(2):261–270, June 2003.
- [141] J T Coull and A C Nobre. Where and when to pay attention: the neural systems for directing attention to spatial locations and to time intervals as revealed by both PET and fMRI. *J. Neurosci.*, 18(18):7426–7435, September 1998.
- [142] Kenneth R Pugh, Bennett A Shaywitz, Sally E Shaywitz, Robert K Fulbright, Dani Byrd, Paweł Skudlarski, Donald P Shankweiler, Leonard Katz, R Todd Constable, Jack Fletcher, Cheryl Lacadie, Karen Marchione, and John C Gore. Auditory selective attention: An fMRI investigation. *Neuroimage*, 4(3):159–173, December 1996.
- [143] K Luan Phan, Tor Wager, Stephan F Taylor, and Israel Liberzon. Functional neuroanatomy of emotion: a meta-analysis of emotion activation studies in PET and fMRI. *Neuroimage*, 16(2):331–348, June 2002.
- [144] Kevin N. Ochsner, Silvia A. Bunge, James J. Gross, and John D. E. Gabrieli. Rethinking feelings: An fmri study of the cognitive regulation of emotion. *Journal of Cognitive Neuroscience*, 14(8):1215–1229, 2002.
- [145] Stefan Koelsch, Thomas Fritz, D Yves Cramon, V, Karsten Müller, and Angela D Friederici. Investigating emotion with music: an fMRI study. *Hum. Brain Mapp.*, 27(3):239–250, March 2006.
- [146] A E Hernandez, M Dapretto, J Mazziotta, and S Bookheimer. Language switching and language representation in Spanish-English bilinguals: an fMRI study. *Neuroimage*, 14(2):510–520, August 2001.
- [147] Martijn P van den Heuvel and Hilleke E Hulshoff Pol. Exploring the brain network: a review on resting-state fMRI functional connectivity. *Eur. Neuropsychopharmacol.*, 20(8):519–534, August 2010.
- [148] Anton Orlichenko, Gang Qu, Gemeng Zhang, Binish Patel, Tony W. Wilson, Julia M. Stephen, Vince D. Calhoun, and Yu-Ping Wang. Latent similarity identifies important functional connections for phenotype prediction. *IEEE Transactions on Biomedical Engineering*, 70(6):1979–1989, 2023.
- [149] Wenxing Hu, Biao Cai, Aiying Zhang, Vince D. Calhoun, and Yu-Ping Wang. Deep collaborative learning with application to the study of multimodal brain development. *IEEE Transactions on Biomedical Engineering*, 66(12):3346–3359, 2019.

- [150] Semra İcer, İrem Acer, and Abdullah Baş. Gender-based functional connectivity differences in brain networks in childhood. *Computer Methods and Programs in Biomedicine*, 192:105444, 2020.
- [151] Bhaskar Sen and Keshab K. Parhi. Predicting biological gender and intelligence from fmri via dynamic functional connectivity. *IEEE Transactions on Biomedical Engineering*, 68(3):815–825, 2021.
- [152] Shuai Wang, Yajing Zhan, Yan Zhang, Luxian Lyu, Hailong Lyu, Guodong Wang, Renrong Wu, Jingping Zhao, and Wenbin Guo. Abnormal long- and short-range functional connectivity in adolescent-onset schizophrenia patients: A resting-state fMRI study. *Progress in Neuro-Psychopharmacology and Biological Psychiatry*, 81:445–451, February 2018.
- [153] Barnaly Rashid, Mohammad R Arbabshirani, Eswar Damaraju, Mustafa S Cetin, Robyn Miller, Godfrey D Pearson, and Vince D Calhoun. Classification of schizophrenia and bipolar patients using static and dynamic resting-state fMRI brain connectivity. *Neuroimage*, 134:645–657, July 2016.
- [154] Emily S Finn, Xilin Shen, Dustin Scheinost, Monica D Rosenberg, Jessica Huang, Marvin M Chun, Xenophon Papademetris, and R Todd Constable. Functional connectome fingerprinting: identifying individuals using patterns of brain connectivity. *Nat. Neurosci.*, 18(11):1664–1671, November 2015.
- [155] Biao Cai, Gemeng Zhang, Wenxing Hu, Aiying Zhang, Pascal Zille, Yipu Zhang, Julia M Stephen, Tony W Wilson, Vince D Calhoun, and Yu-Ping Wang. Re-fined measure of functional connectomes for improved identifiability and prediction. *Hum. Brain Mapp.*, 40(16):4843–4858, November 2019.
- [156] Nico U F Dosenbach, Binyam Nardos, Alexander L Cohen, Damien A Fair, Jonathan D Power, Jessica A Church, Steven M Nelson, Gagan S Wig, Alecia C Vogel, Christina N Lessov-Schlaggar, Kelly Anne Barnes, Joseph W Dubis, Eric Feczkó, Rebecca S Coalson, John R Pruett, Jr, Deanna M Barch, Steven E Petersen, and Bradley L Schlaggar. Prediction of individual brain maturity using fMRI. *Science*, 329(5997):1358–1361, September 2010.
- [157] Lauren E Mak, Luciano Minuzzi, Glenda MacQueen, Geoffrey Hall, Sidney H Kennedy, and Roumen Milev. The default mode network in healthy individuals: A systematic review and meta-analysis. *Brain Connect.*, 7(1):25–33, February 2017.
- [158] Bronte Ficek-Tani, Corey Horien, Suyeon Ju, Wanwan Xu, Nancy Li, Cheryl Lacadie, Xilin Shen, Dustin Scheinost, Todd Constable, and Carolyn Fredericks. Sex differences in default mode network connectivity in healthy aging adults. *Cereb. Cortex*, December 2022.
- [159] Anders M Fjell, Markus H Sneve, Håkon Grydeland, Andreas B Storsve, Inge K Amlie, Anastasia Yendiki, and Kristine B Walhovd. Relationship between

- structural and functional connectivity change across the adult lifespan: A longitudinal investigation. *Hum. Brain Mapp.*, 38(1):561–573, January 2017.
- [160] Adam M Staffaroni, Jesse A Brown, Kaitlin B Casaletto, Fanny M Elahi, Jersey Deng, John Neuhaus, Yann Cobigo, Paige S Mumford, Samantha Walters, Rowan Saloner, Anna Karydas, Giovanni Coppola, Howie J Rosen, Bruce L Miller, William W Seeley, and Joel H Kramer. The longitudinal trajectory of default mode network connectivity in healthy older adults varies as a function of age and is associated with changes in episodic memory and processing speed. *J. Neurosci.*, 38(11):2809–2817, March 2018.
  - [161] Sarah Hirsiger, Vincent Koppelmans, Susan Mérillat, Franziskus Liem, Burak Erdeniz, Rachael D Seidler, and Lutz Jäncke. Structural and functional connectivity in healthy aging: Associations for cognition and motor behavior. *Hum. Brain Mapp.*, 37(3):855–867, March 2016.
  - [162] Alireza Salami, Anders Wåhlin, Neda Kaboodvand, Anders Lundquist, and Lars Nyberg. Longitudinal evidence for dissociation of anterior and posterior MTL resting-state connectivity in aging: Links to perfusion and memory. *Cereb. Cortex*, 26(10):3953–3963, October 2016.
  - [163] Stephen M. Smith, Fidel Alfaro-Almagro, and Karla L. Miller. Uk biobank brain imaging documentation. Technical report, UK Biobank, September 2022.
  - [164] Ahmad R. Hariri, Alessandro Tessitore, Venkata S. Mattay, Francesco Fera, and Daniel R. Weinberger. The amygdala response to emotional stimuli: A comparison of faces and scenes. *NeuroImage*, 17(1):317–323, September 2002.
  - [165] Fidel Alfaro-Almagro, Mark Jenkinson, Neal K Bangerter, Jesper L R Andersson, Ludovica Griffanti, Gwenaëlle Douaud, Stamatios N Sotiroopoulos, Saad Jbabdi, Moises Hernandez-Fernandez, Emmanuel Vallee, Diego Vidaurre, Matthew Webster, Paul McCarthy, Christopher Rorden, Alessandro Daducci, Daniel C Alexander, Hui Zhang, Iulius Dragonu, Paul M Matthews, Karla L Miller, and Stephen M Smith. Image processing and quality control for the first 10,000 brain imaging datasets from UK biobank. *Neuroimage*, 166:400–424, February 2018.
  - [166] F. Pedregosa, G. Varoquaux, A. Gramfort, V. Michel, B. Thirion, O. Grisel, M. Blondel, P. Prettenhofer, R. Weiss, V. Dubourg, J. Vanderplas, A. Passos, D. Cournapeau, M. Brucher, M. Perrot, and E. Duchesnay. Scikit-learn: Machine learning in Python. *Journal of Machine Learning Research*, 12:2825–2830, 2011.
  - [167] Laia Farras-Permanyer, Núria Mancho-Fora, Marc Montalà-Flaquer, David Bartrés-Faz, Lídia Vaqué-Alcázar, Maribel Peró-Cebollero, and Joan Guàrdia-Olmos. Age-related changes in resting-state functional connectivity in older adults. *Neural Regen. Res.*, 14(9):1544, 2019.

- [168] Anne Hafkemeijer, Irmhild Altmann-Schneider, Anna M. Oleksik, Lotte van de Wiel, Huub A.M. Middelkoop, Mark A. van Buchem, Jeroen van der Grond, and Serge A.R.B. Rombouts. Increased functional connectivity and brain atrophy in elderly with subjective memory complaints. *Brain Connectivity*, 3(4):353–362, August 2013.
- [169] Roser Sala-Llonch, David Bartrés-Faz, and Carme Junqué. Reorganization of brain networks in aging: a review of functional connectivity studies. *Front. Psychol.*, 6:663, May 2015.
- [170] Brigitta Malagurski, Pascal Frédéric Deschwanden, Lutz Jäncke, and Susan Mérillat. Longitudinal functional connectivity patterns of the default mode network in healthy older adults. *NeuroImage*, 259:119414, October 2022.
- [171] Hazel I Zonneveld, Raimon H R Pruim, Daniel Bos, Henri A Vrooman, Ryan L Muetzel, Albert Hofman, Serge Arb Rombouts, Aad van der Lugt, Wiro J Niessen, M Arfan Ikram, and Meike W Vernooij. Patterns of functional connectivity in an aging population: The rotterdam study. *Neuroimage*, 189:432–444, April 2019.
- [172] Dietsje D Jolles, Mark A van Buchem, Eveline A Crone, and Serge A R B Rombouts. A comprehensive study of whole-brain functional connectivity in children and young adults. *Cereb. Cortex*, 21(2):385–391, February 2011.
- [173] Anton Orlichenko, Gang Qu, and Yu-Ping Wang. Phenotype guided interpretable graph convolutional network analysis of fMRI data reveals changing brain connectivity during adolescence. In Barjor S. Gimi and Andrzej Krol, editors, *Medical Imaging 2022: Biomedical Applications in Molecular, Structural, and Functional Imaging*, volume 12036, pages 294 – 303. International Society for Optics and Photonics, SPIE, 2022.
- [174] Gang Qu, Li Xiao, Wenxing Hu, Junqi Wang, Kun Zhang, Vince D. Calhoun, and Yu-Ping Wang. Ensemble manifold regularized multi-modal graph convolutional network for cognitive ability prediction. *IEEE Transactions on Biomedical Engineering*, 68(12):3564–3573, 2021.
- [175] Yuhui Du, Zening Fu, and Vince D. Calhoun. Classification and prediction of brain disorders using functional connectivity: Promising but challenging. *Frontiers in Neuroscience*, 12, 2018.
- [176] Hojjat Salehinejad, Jumpei Kitamura, Noah G. Ditkofsky, Amy Wei Lin, Aditya Bharatha, Suradech Suthiphoswan, Hui-Ming Lin, Jefferson R. Wilson, Muhammad Mamdani, and Errol Colak. A real-world demonstration of machine learning generalizability in the detection of intracranial hemorrhage on head computerized tomography. *Scientific Reports*, 11, 2021.

- [177] Alexander Selvikvåg Lundervold and Arvid Lundervold. An overview of deep learning in medical imaging focusing on mri. *Zeitschrift für Medizinische Physik*, 29(2):102–127, 2019. Special Issue: Deep Learning in Medical Physics.
- [178] Zohaib Salahuddin, Henry C. Woodruff, Avishek Chatterjee, and Philippe Lambin. Transparency of deep neural networks for medical image analysis: A review of interpretability methods. *Computers in Biology and Medicine*, 140:105111, 2022.
- [179] Gaël Varoquaux and Veronika Cheplygina. Machine learning for medical imaging: methodological failures and recommendations for the future. *NPJ Digit. Med.*, 5(1):48, April 2022.
- [180] Xi Zhang, Meng Liang, Wen Qin, Baikun Wan, Chunshui Yu, and Dong Ming. Gender differences are encoded differently in the structure and function of the human brain revealed by multimodal mri. *Frontiers in Human Neuroscience*, 14, 2020.
- [181] Natalia Z Bielczyk, Sebo Uithol, Tim van Mourik, Paul Anderson, Jeffrey C Glennon, and Jan K Buitelaar. Disentangling causal webs in the brain using functional magnetic resonance imaging: A review of current approaches. *Netw. Neurosci.*, 3(2):237–273, February 2019.
- [182] Indhupriya Subramanian, Srikant Verma, Shiva Kumar, Abhay Jere, and Krishanpal Anamika. Multi-omics data integration, interpretation, and its application. *Bioinform. Biol. Insights*, 14:1177932219899051, January 2020.
- [183] Wenxing Hu, Xianghe Meng, Yuntong Bai, Aiying Zhang, Gang Qu, Biao Cai, Gemeng Zhang, Tony W. Wilson, Julia M. Stephen, Vince D. Calhoun, and Yu ping Wang. Interpretable multimodal fusion networks reveal mechanisms of brain cognition. *IEEE Transactions on Medical Imaging*, 40:1474–1483, 2021.
- [184] Samuel M Gross and Robert Tibshirani. Collaborative regression. *Biostatistics*, 16(2):326–338, April 2015.
- [185] Xueli Song, Rongpeng Li, Kaiming Wang, Yuntong Bai, Yuzhu Xiao, and Yu-Ping Wang. Joint sparse collaborative regression on imaging genetics study of schizophrenia. *IEEE/ACM Transactions on Computational Biology and Bioinformatics*, pages 1–1, 2022.
- [186] Mahmut Kaya and Hasan S. Bilge. Deep metric learning: A survey. *Symmetry*, 11:1066, 2019.
- [187] Sanae Kato, Epifanio Bagarinao, Haruo Isoda, Shuji Koyama, Hirohisa Watanabe, Satoshi Maesawa, Daisuke Mori, Kazuhiro Hara, Masahisa Katsuno, Minoru Hoshiyama, Shinji Naganawa, Norio Ozaki, and Gen Sobue. Effects of head motion on the evaluation of age-related brain network changes using resting state functional MRI. *Magn Reson Med Sci*, 20(4):338–346, October 2020.

- [188] Jie Zhou, Ganqu Cui, Zhengyan Zhang, Cheng Yang, Zhiyuan Liu, and Maosong Sun. Graph neural networks: A review of methods and applications. *ArXiv*, abs/1812.08434, 2020.
- [189] Petar Velickovic, Guillem Cucurull, Arantxa Casanova, Adriana Romero, Pietro Lio', and Yoshua Bengio. Graph attention networks. *ArXiv*, abs/1710.10903, 2018.
- [190] Muhan Zhang and Yixin Chen. Link prediction based on graph neural networks. In S. Bengio, H. Wallach, H. Larochelle, K. Grauman, N. Cesa-Bianchi, and R. Garnett, editors, *Advances in Neural Information Processing Systems*, volume 31. Curran Associates, Inc., 2018.
- [191] H Hotelling. Relations between two sets of variates. *Biometrika*, 28(3-4):321–377, December 1936.
- [192] Gang Li, Depeng Han, Chao Wang, Wenxing Hu, Vince D. Calhoun, and Yu-Ping Wang. Application of deep canonically correlated sparse autoencoder for the classification of schizophrenia. *Computer Methods and Programs in Biomedicine*, 183:105073, 2020.
- [193] Shotaro Akaho. A kernel method for canonical correlation analysis. *CoRR*, abs/cs/0609071, 2006.
- [194] Owen Richfield, Md Ashad Alam, Vince Calhoun, and Yu-Ping Wang. Learning schizophrenia imaging genetics data via multiple kernel canonical correlation analysis. In *2016 IEEE International Conference on Bioinformatics and Biomedicine (BIBM)*. IEEE, December 2016.
- [195] Mingkai Zheng, Shan You, Lang Huang, Fei Wang, Chen Qian, and Chang Xu. Simmatch: Semi-supervised learning with similarity matching. In *Proceedings of the IEEE/CVF Conference on Computer Vision and Pattern Recognition (CVPR)*, pages 14471–14481, June 2022.
- [196] Yuval Atzmon, Uri Shalit, and Gal Chechik. Learning sparse metrics, one feature at a time. In Dmitry Storcheus, Afshin Rostamizadeh, and Sanjiv Kumar, editors, *Proceedings of the 1st International Workshop on Feature Extraction: Modern Questions and Challenges at NIPS 2015*, volume 44 of *Proceedings of Machine Learning Research*, pages 30–48, Montreal, Canada, 11 Dec 2015. PMLR.
- [197] Thomas Kipf and Max Welling. Semi-supervised classification with graph convolutional networks. *ArXiv*, abs/1609.02907, 2017.
- [198] J. Daniel Ragland, Bruce I. Turetsky, Ruben C. Gur, Faith M. Gunning-Dixon, Travis H Turner, Lee Schroeder, Robin M. Chan, and Raquel E. Gur. Working memory for complex figures: an fmri comparison of letter and fractal n-back tasks. *Neuropsychology*, 16 3:370–9, 2002.

- [199] Karl J. Friston, C. D. Frith, R. S. J. Frackowiak, and Robert Turner. Characterizing dynamic brain responses with fmri: A multivariate approach. *NeuroImage*, 2:166–172, 1995.
- [200] Jian Fang, Chao Xu, Pascal Zille, Dongdong Lin, Hong-Wen Deng, Vince D Calhoun, and Yu-Ping Wang. Fast and accurate detection of complex imaging genetics associations based on greedy projected distance correlation. *IEEE Trans. Med. Imaging*, 37(4):860–870, April 2018.
- [201] Niharika Shimona Dsouza et al. M-GCN: A multimodal graph convolutional network to integrate functional and structural connectomics data to predict multidimensional phenotypic characterizations. In Mattias Heinrich, Qi Dou, Marleen de Bruijne, Jan Lellmann, Alexander Schläfer, and Floris Ernst, editors, *Proceedings of the Fourth Conference on Medical Imaging with Deep Learning*, volume 143 of *Proceedings of Machine Learning Research*, pages 119–130. PMLR, 07–09 Jul 2021.
- [202] Yann LeCun, Léon Bottou, Yoshua Bengio, and Patrick Haffner. Gradient-based learning applied to document recognition. In *Proceedings of the IEEE*, volume 86, pages 2278–2324, 1998.
- [203] Chayanika Goswami, Amrita Chattopadhyay, and Eric Y Chuang. Rare variants: data types and analysis strategies. *Ann. Transl. Med.*, 9(12):961, June 2021.
- [204] Maria Rigau, David Juan, Alfonso Valencia, and Daniel Rico. Intronic CNVs and gene expression variation in human populations. *PLoS Genet.*, 15(1):e1007902, January 2019.
- [205] Theodore D Satterthwaite, Daniel H Wolf, David R Roalf, Kosha Ruparel, Guray Erus, Simon Vandekar, Efstathios D Gennatas, Mark A Elliott, Alex Smith, Hakon Hakonarson, Ragini Verma, Christos Davatzikos, Raquel E Gur, and Ruben C Gur. Linked sex differences in cognition and functional connectivity in youth. *Cereb. Cortex*, 25(9):2383–2394, September 2015.
- [206] Rongtao Jiang, Dustin Scheinost, Nianming Zuo, Jing Wu, Shile Qi, Qinghao Liang, Dongmei Zhi, Na Luo, Young-Chul Chung, Sha Liu, Yong Xu, Jing Sui, and Vince Calhoun. A neuroimaging signature of cognitive aging from whole-brain functional connectivity. *Adv. Sci. (Weinh.)*, 9(24):e2201621, August 2022.
- [207] Jonas Persson, Sara Pudas, Lars-Göran Nilsson, and Lars Nyberg. Longitudinal assessment of default-mode brain function in aging. *Neurobiology of Aging*, 35(9):2107–2117, 2014.
- [208] Fengmei Fan, Xuhong Liao, Tianyuan Lei, Tengda Zhao, Mingrui Xia, Weiwei Men, Yanpei Wang, Mingming Hu, Jie Liu, Shaozheng Qin, Shuping Tan, Jia-Hong Gao, Qi Dong, Sha Tao, and Yong He. Development of the default-mode

- network during childhood and adolescence: A longitudinal resting-state fmri study. *NeuroImage*, 226:117581, 2021.
- [209] Guixia Pan, Li Xiao, Yuntong Bai, Tony W. Wilson, Julia M. Stephen, Vince D. Calhoun, and Yu-Ping Wang. Multiview diffusion map improves prediction of fluid intelligence with two paradigms of fmri analysis. *IEEE Transactions on Biomedical Engineering*, 68(8):2529–2539, 2021.
  - [210] Lu Zhang, Jiajia Zhao, Qunjie Zhou, Zhaowen Liu, Yi Zhang, Wei Cheng, Weikang Gong, Xiaoping Hu, Wenlian Lu, Edward T Bullmore, Chun-Yi Zac Lo, and Jianfeng Feng. Sensory, somatomotor and internal mentation networks emerge dynamically in the resting brain with internal mentation predominating in older age. *Neuroimage*, 237(118188):118188, August 2021.
  - [211] F. Van Overwalle, Q. Ma, and E. Heleven. The posterior crus II cerebellum is specialized for social mentalizing and emotional self-experiences: a meta-analysis. *Soc Cogn Affect Neurosci*, 15(9):905–928, 11 2020.
  - [212] G. Zhang, B. Cai, A. Zhang, Z. Tu, L. Xiao, J. M. Stephen, T. W. Wilson, V. D. Calhoun, and Y. P. Wang. Detecting abnormal connectivity in schizophrenia via a joint directed acyclic graph estimation model. *Neuroimage*, 260:119451, Jul 2022.
  - [213] L. Q. Uddin, J. S. Nomi, B. Hébert-Seropian, J. Ghaziri, and O. Boucher. Structure and Function of the Human Insula. *J Clin Neurophysiol*, 34(4):300–306, Jul 2017.
  - [214] V. Mazzola, G. Arciero, L. Fazio, T. Lanciano, B. Gelao, T. Popolizio, P. Vuilleumier, G. Bondolfi, and A. Bertolino. What Impact does An Angry Context have Upon Us? The Effect of Anger on Functional Connectivity of the Right Insula and Superior Temporal Gyri. *Front Behav Neurosci*, 10:109, 2016.
  - [215] Wataru Sato, Yasutaka Kubota, Takanori Kochiyama, Shota Uono, Sayaka Yoshimura, Reiko Sawada, Morimitsu Sakihama, and Motomi Toichi. Increased putamen volume in adults with autism spectrum disorder. *Frontiers in Human Neuroscience*, 8, 2014.
  - [216] Kevin R. McLeod, Lisa Marie Langevin, Bradley G. Goodyear, and Deborah Dewey. Functional connectivity of neural motor networks is disrupted in children with developmental coordination disorder and attention-deficit/hyperactivity disorder. *NeuroImage: Clinical*, 4:566–575, 2014.
  - [217] J. Xu, S. Kemeny, G. Park, C. Frattali, and A. Braun. Language in context: emergent features of word, sentence, and narrative comprehension. *Neuroimage*, 25(3):1002–1015, Apr 2005.

- [218] J. Zhao, Y. Zhang, F. Liu, J. Chen, J. Zhao, and W. Guo. Abnormal global-brain functional connectivity and its relationship with cognitive deficits in drug-naive first-episode adolescent-onset schizophrenia. *Brain Imaging Behav*, 16(3):1303–1313, Jun 2022.
- [219] Z. He, F. Lu, W. Sheng, S. Han, Z. Long, Y. Chen, W. Luo, Y. Yu, X. Nan, A. Ouyang, Q. Cui, and H. Chen. Functional dysconnectivity within the emotion-regulating system is associated with affective symptoms in major depressive disorder: A resting-state fMRI study. *Aust N Z J Psychiatry*, 53(6):528–539, 06 2019.
- [220] J. Liu, J. Li, C. A. Rieth, D. E. Huber, J. Tian, and K. Lee. A dynamic causal modeling analysis of the effective connectivities underlying top-down letter processing. *Neuropsychologia*, 49(5):1177–1186, Apr 2011.
- [221] G. Delvecchio, E. Maggioni, A. Pignoni, B. Crespo-Facorro, I. Nenadić, F. Benedetti, C. Gaser, H. Sauer, R. Roiz-Santiañez, S. Poletti, M. G. Rossetti, M. Bellani, C. Perlini, M. Ruggeri, V. A. Diwadkar, and P. Brambilla. Sexual Regional Dimorphism of Post-Adolescent and Middle Age Brain Maturation. A Multi-center 3T MRI Study. *Front Aging Neurosci*, 13:622054, 2021.
- [222] T. Bereczkei, A. Deak, P. Papp, G. Perlaki, and G. Orsi. Neural correlates of Machiavellian strategies in a social dilemma task. *Brain Cogn*, 82(1):108–116, Jun 2013.
- [223] B. Tomasino, D. Marin, M. Maieron, T. Ius, R. Budai, F. Fabbro, and M. Skrap. Foreign accent syndrome: a multimodal mapping study. *Cortex*, 49(1):18–39, Jan 2013.
- [224] J DiGuiseppi and P Tadi. *Neuroanatomy, Postcentral Gyrus*. StatPearls Publishing, Treasure Island, FL, Jul 2021.
- [225] Kaija Sander, Xiaoqian Chai, Elise B Barbeau, Shanna Kousaie, Michael Petrides, Shari Baum, and Denise Klein. Interhemispheric functional brain connectivity predicts new language learning success in adults. *Cerebral Cortex*, 03 2022. bhac131.
- [226] Charles R. Harris, K. Jarrod Millman, Stéfan J. van der Walt, Ralf Gommers, Pauli Virtanen, David Cournapeau, Eric Wieser, Julian Taylor, Sebastian Berg, Nathaniel J. Smith, Robert Kern, Matti Picus, Stephan Hoyer, Marten H. van Kerkwijk, Matthew Brett, Allan Haldane, Jaime Fernández del Río, Mark Wiebe, Pearu Peterson, Pierre Gérard-Marchant, Kevin Sheppard, Tyler Reddy, Warren Weckesser, Hameer Abbasi, Christoph Gohlke, and Travis E. Oliphant. Array programming with NumPy. *Nature*, 585(7825):357–362, September 2020.
- [227] Adam Paszke, Sam Gross, Francisco Massa, Adam Lerer, James Bradbury, Gregory Chanan, Trevor Killeen, Zeming Lin, Natalia Gimelshein, Luca Antiga,

- Alban Desmaison, Andreas Kopf, Edward Yang, Zachary DeVito, Martin Raison, Alykhan Tejani, Sasank Chilamkurthy, Benoit Steiner, Lu Fang, Junjie Bai, and Soumith Chintala. Pytorch: An imperative style, high-performance deep learning library. In *Advances in Neural Information Processing Systems 32*, pages 8024–8035. Curran Associates, Inc., 2019.
- [228] Alexandre Abraham, Fabian Pedregosa, Michael Eickenberg, Philippe Gervais, Andreas Mueller, Jean Kossaifi, Alexandre Gramfort, Bertrand Thirion, and Gaël Varoquaux. Machine learning for neuroimaging with scikit-learn. *Frontiers in Neuroinformatics*, 8, 2014.
- [229] Krzysztof J. Gorgolewski, Oscar Esteban, Christopher Burns, Erik Ziegler, Basile Pinsard, Cindee Madison, Michael Waskom, David Gage Ellis, Dav Clark, Michael Dayan, Alexandre Manhães-Savio, Michael Philipp Notter, Hans Johnson, Blake E Dewey, Yaroslav O. Halchenko, Carlo Hamalainen, Anisha Kesavan, Daniel Clark, Julia M. Huntenburg, Michael Hanke, B. Nolan Nichols, Demian Wassermann, Arman Eshaghi, Christopher Markiewicz, Gael Varoquaux, Benjamin Acland, Jessica Forbes, Ariel Rokem, Xiang-Zhen Kong, Alexandre Gramfort, Jens Kleesiek, Alexander Schaefer, Sharad Sikka, Martin Felipe Perez-Guevara, Tristan Glatard, Shariq Iqbal, Siqi Liu, David Welch, Paul Sharp, Joshua Warner, Erik Kastman, Leonie Lampe, L. Nathan Perkins, R. Cameron Craddock, René Küttner, Dmytro Bielievtsov, Daniel Geisler, Stephan Gerhard, Franziskus Liem, Janosch Linkersdörfer, Daniel S. Margulies, Sami Kristian Andberg, Jörg Stadler, Christopher John Steele, William Broderick, Gavin Cooper, Andrew Floren, Lijie Huang, Ivan Gonzalez, Daniel McNamee, Dimitri Papadopoulos Orfanos, John Pellman, William Triplett, and Satrajit Ghosh. Nipype: a flexible, lightweight and extensible neuroimaging data processing framework in Python. 0.12.0-rc1, April 2016.
- [230] Mingrui Xia, Jinhui Wang, and Yong He. BrainNet viewer: A network visualization tool for human brain connectomics. *PLoS ONE*, 8(7):e68910, July 2013.
- [231] V.D. Calhoun, T. Adali, G.D. Pearson, and J.J. Pekar. A method for making group inferences from functional MRI data using independent component analysis. *Human Brain Mapping*, 14(3):140–151, 2001.
- [232] Sergey M. Plis, Anand D. Sarwate, Dylan Wood, Christopher Dieringer, Drew Landis, Cory Reed, Sandeep R. Panta, Jessica A. Turner, Jody M. Shoemaker, Kim W. Carter, Paul Thompson, Kent Hutchison, and Vince D. Calhoun. COINSTAC: A privacy enabled model and prototype for leveraging and processing decentralized brain imaging data. *Frontiers in Neuroscience*, 10, August 2016.
- [233] Louisa Lyon. Dead salmon and voodoo correlations: should we be sceptical about functional MRI? *Brain*, 140(8):e53, August 2017.

- [234] Craig M Bennett and Michael B Miller. How reliable are the results from functional magnetic resonance imaging? *Ann. N. Y. Acad. Sci.*, 1191(1):133–155, March 2010.
- [235] Usama Pervaiz, Diego Vidaurre, Mark W Woolrich, and Stephen M Smith. Optimising network modelling methods for fMRI. *Neuroimage*, 211(116604):116604, May 2020.
- [236] Judy Wawira Gichoya, Imon Banerjee, Ananth Reddy Bhimireddy, John L Burns, Leo Anthony Celi, Li-Ching Chen, Ramon Correa, Natalie Dullerud, Marzyeh Ghassemi, Shih-Cheng Huang, Po-Chih Kuo, Matthew P Lungren, Lyle J Palmer, Brandon J Price, Saptarshi Purkayastha, Ayis T Pyrros, Lauren Oakden-Rayner, Chima Okechukwu, Laleh Seyyed-Kalantari, Hari Trivedi, Ryan Wang, Zachary Zaiman, and Haoran Zhang. AI recognition of patient race in medical imaging: a modelling study. *Lancet Digit. Health*, 4(6):e406–e414, June 2022.
- [237] Jingwei Li, Danilo Bzdok, Jianzhong Chen, Angela Tam, Leon Qi Rong Ooi, Avram J Holmes, Tian Ge, Kaustubh R Patil, Mbemba Jabbi, Simon B Eickhoff, B T Thomas Yeo, and Sarah Genon. Cross-ethnicity/race generalization failure of behavioral prediction from resting-state functional connectivity. *Sci. Adv.*, 8(11):eabj1812, March 2022.
- [238] Zhongyang Wang, Junchang Xin, Zhiqiong Wang, Yudong Yao, Yue Zhao, and Wei Qian. Brain functional network modeling and analysis based on fMRI: a systematic review. *Cogn. Neurodyn.*, 15(3):389–403, June 2021.
- [239] Thania Balducci, Jalil Rasgado-Toledo, Alely Valencia, Maria-Jose van Tol, Andre Aleman, and Eduardo A. Garza-Villarreal. ”a behavioral, clinical and brain imaging dataset with focus on emotion regulation of females with fibromyalgia”, 2022.
- [240] Christopher J Markiewicz, Krzysztof J Gorgolewski, Franklin Feingold, Ross Blair, Yaroslav O Halchenko, Eric Miller, Nell Hardcastle, Joe Wexler, Oscar Esteban, Mathias Goncavles, Anita Jwa, and Russell Poldrack. The OpenNeuro resource for sharing of neuroscience data. *Elife*, 10, October 2021.
- [241] Rene Weber, Frederic R. Hopp, Allison Eden, and Kate Lee. ”vicarious punishment of moral violations in naturalistic drama narratives predicts cortical synchronization”, 2023.
- [242] Anees Abrol, Hooman Rokham, and Vince D. Calhoun. Diagnostic and prognostic classification of brain disorders using residual learning on structural mri data. In *2019 41st Annual International Conference of the IEEE Engineering in Medicine and Biology Society (EMBC)*, pages 4084–4088, 2019.

- [243] Qishan Chen, Yurou Kong, Wenyang Gao, and Lei Mo. Effects of socioeconomic status, parent-child relationship, and learning motivation on reading ability. *Front. Psychol.*, 9, July 2018.
- [244] Mohamad Amin Pourhoseingholi, Ahmad Reza Baghestani, and Mohsen Vahedi. How to control confounding effects by statistical analysis. *Gastroenterol. Hepatol. Bed Bench*, 5(2):79–83, 2012.
- [245] Andrea C Skelly, Joseph R Dettori, and Erika D Brodt. Assessing bias: the importance of considering confounding. *Evid. Based Spine Care J.*, 3(1):9–12, February 2012.
- [246] Prafulla Dhariwal and Alexander Quinn Nichol. Diffusion models beat GANs on image synthesis. In A. Beygelzimer, Y. Dauphin, P. Liang, and J. Wortman Vaughan, editors, *Advances in Neural Information Processing Systems*, 2021.
- [247] Diederik P. Kingma and Max Welling. Auto-Encoding Variational Bayes. In *2nd International Conference on Learning Representations, ICLR 2014, Banff, AB, Canada, April 14-16, 2014, Conference Track Proceedings*, 2014.
- [248] Kevin P. Murphy. *Probabilistic Machine Learning: Advanced Topics*. MIT Press, 2023.
- [249] Kihyuk Sohn, Honglak Lee, and Xinchen Yan. Learning structured output representation using deep conditional generative models. In C. Cortes, N. Lawrence, D. Lee, M. Sugiyama, and R. Garnett, editors, *Advances in Neural Information Processing Systems*, volume 28. Curran Associates, Inc., 2015.
- [250] Ali Razavi, Aäron van den Oord, and Oriol Vinyals. Generating diverse high-fidelity images with VQ-VAE-2. In Hanna M. Wallach, Hugo Larochelle, Alina Beygelzimer, Florence d’Alché-Buc, Emily B. Fox, and Roman Garnett, editors, *Advances in Neural Information Processing Systems 32: Annual Conference on Neural Information Processing Systems 2019, NeurIPS 2019, December 8-14, 2019, Vancouver, BC, Canada*, pages 14837–14847, 2019.
- [251] Aditya Ramesh, Mikhail Pavlov, Gabriel Goh, Scott Gray, Chelsea Voss, Alec Radford, Mark Chen, and Ilya Sutskever. Zero-shot text-to-image generation, 2021. cite arxiv:2102.12092.
- [252] Jung-Hoon Kim, Yizhen Zhang, Kuan Han, Zheyu Wen, Minkyu Choi, and Zhongming Liu. Representation learning of resting state fMRI with variational autoencoder. *Neuroimage*, 241(118423):118423, November 2021.
- [253] Ian Goodfellow, Jean Pouget-Abadie, Mehdi Mirza, Bing Xu, David Warde-Farley, Sherjil Ozair, Aaron Courville, and Yoshua Bengio. Generative adversarial nets. In *Advances in neural information processing systems*, pages 2672–2680, 2014.

- [254] Martin Arjovsky, Soumith Chintala, and Léon Bottou. Wasserstein generative adversarial networks. In Doina Precup and Yee Whye Teh, editors, *Proceedings of the 34th International Conference on Machine Learning*, volume 70 of *Proceedings of Machine Learning Research*, pages 214–223. PMLR, 06–11 Aug 2017.
- [255] Maria Elena Laino, Pierandrea Cancian, Letterio Salvatore Politi, Matteo Giovanni Della Porta, Luca Saba, and Victor Savevski. Generative adversarial networks in brain imaging: A narrative review. *J. Imaging*, 8(4), March 2022.
- [256] Laurens van der Maaten and Geoffrey Hinton. Visualizing data using t-sne. *Journal of Machine Learning Research*, 9(86):2579–2605, 2008.
- [257] Stacy Liechti, Gianna Capodilupo, Douglas J Opler, Mark Opler, and Lawrence H Yang. A developmental history of the positive and negative syndrome scale (PANSS). *Innov. Clin. Neurosci.*, 14(11-12):12–17, December 2017.
- [258] Mona Dabiri, Fatemeh Dehghani Firouzabadi, Kun Yang, Peter B Barker, Roland R Lee, and David M Yousem. Neuroimaging in schizophrenia: A review article. *Front. Neurosci.*, 16:1042814, November 2022.

## Biography

Anton Orlichenko was born in Serpukhov, Russia (formerly the USSR) in 1988. He received a Bachelor of Science degree in Computer and Electrical Engineering from the Illinois Institute of Technology, Chicago, IL, USA in 2010. He started his Ph.D. studies in the Biomedical Engineering program at Tulane University in August 2020 and is completing the program in November 2024.